UNIVERSITY OF THESSALY
SCHOOL OF ENGINEERING
DEPARTMENT OF MECHANICAL ENGINEERING

Finite element simulation of the structural behavior of elastic cylindrical shells under external pressure for biomedical applications

Diploma Thesis

Karetsa Ioanna

Submitted in partial fulfillment of the requirements for the degree of Diploma in Mechanical Engineering at the University of Thessaly

June 2023

© 2023 Ioanna Karetsa

The approval of the present Diploma Thesis by the Department of Mechanical Engineering, School of Engineering, University of Thessaly, does not constitute acceptance of the writer's views (Greek Law No.5343/32, article 202, paragraph 2).

Approved by the Examination Committee:

Supervisor **Prof. Spyros Karamanos**
Professor, Department of Mechanical Engineering, University of Thessaly

Member **Prof. Michalis Agoras**
Assistant professor, Department of Mechanical Engineering, University of Thessaly

Member **Prof. Georgios Charalampous**
Assistant Professor, Department of Mechanical Engineering, University of Thessaly

DISCLAIMER ON ACADEMIC ETHICS AND INTELLECTUAL PROPERTY RIGHTS

«Being fully aware of the implications of copyright laws, I expressly state that this diploma thesis, as well as the electronic files and source codes developed or modified in the course of this thesis, are solely the product of my personal work and do not infringe any rights of intellectual property, personality and personal data of third parties, do not contain work / contributions of third parties for which the permission of the authors / beneficiaries is required and are not a product of partial or complete plagiarism, while the sources used are limited to the bibliographic references only and meet the rules of scientific citing. The points where I have used ideas, text, files and / or sources of other authors are clearly mentioned in the text with the appropriate citation and the relevant complete reference is included in the bibliographic references section. I also declare that the results of the work have not been used to obtain another degree. I fully, individually and personally undertake all legal and administrative consequences that may arise in the event that it is proven, in the course of time, that this thesis or part of it does not belong to me because it is a product of plagiarism».

The declarant

Karetsa Ioanna

Acknowledgements

I would like to express my sincere gratitude and appreciation to my supervisor, Proff. Spyros A. Karamanos, for his invaluable guidance throughout not only during the conduction of this thesis, but also during my undergraduate studies in general. His knowledge and support have been instrumental in shaping this research. I would also like to extend my heartfelt thanks to the other members of the examination committee for their valuable input and feedback. Also, I am especially grateful to Aristeidis-Georgios Stamou for his continuous assistance and collaboration, strarting from the assignment of the thesis theme till the last moment of writting process. His contributions have been immensely helpful in the development of this work. Furthermore, I would like to express my deepest appreciation to my family members and friends for their unwavering support and encouragement during the entire process of studying and writing this diploma thesis. Their presence and encouragement have been a constant source of motivation. Once again, I extend my heartfelt thanks to everyone who has played a part in making this thesis possible.

Diploma Thesis

Finite element simulation of the structural behavior of elastic cylindrical shells under external pressure for biomedical applications

Karetsa Ioanna

Abstract

Collapsible tubes from their nature are vulnerable to collapse. Veins, arteries, airways, and other tubular structures found in living organisms can be described as collapsible tubes. In specific circumstances, the investigation of which isn't the objective of this thesis, these tubular structures are susceptible to imperfections that may result in collapse and propagation under uniform external pressure. In this thesis, the aim was to simulate the behavior of collapsible tubes when initial ovality and uniform external pressure applied. Thin and thick walled tubes, with five different diameter-to-thickness ratios, are studied numerically utilizing finite element simulations in ABAQUS. Three-dimensional slice models and long tube models have been conducted as base cases, in order to investigate propagation pressure extracted from their pressure-volume responses, and contact conditions of propagation obtained from the corresponding configurations. Deformation theory was employed as non-linear elastic material model. A parametric investigation has been performed to examine the effects of material exponents, element type, and mesh density applied on the base case models. Furthermore, the influence of ring geometry was investigated through analyses of 3D models. Parametric analyses was also carried out into the relationship between the type of element and its impact on the propagation pressure. Also, effect of initial ovality has been scrutinized by the construction of two-dimensional models. The collapse responses of the 2D models were examined for elastic material and the results were compared with analytical solutions. Overall, the main conclusions drawn from the 3D analysis are that propagation pressure is dependent of the material exponent of Deformation Theory, of tubes geometry and of element type of modeling part. However,the value of propagation pressure is independent of the mesh density. As the material exponent increases, the propagation pressure diminishes. Additionally, as the tube's cross-section becomes thinner, the extension of propagation plateau decreases. Also, element type of the modeling part doesn't affect the contact propagation conditions when the material exponent remains constant. Lastly, the conclusions from the

2D models highlight that as the initial imperfection value increases, the deviation of the collapse pressure from curve of the ideal case also increases leading to the softening of the ring and collapsing at lower pressures.

Διπλωματική Εργασία

Προσομοίωση πεπερασμένων στοιχείων της δομικής συμπεριφοράς ελαστικών κυλινδρικών κελυφών υπό εξωτερική πίεση για βιοϊατρικές εφαρμογές

Καρέτσα Ιωάννα

Περίληψη

Οι πτυσσόμενοι σωλήνες λόγω της φύσης τους είναι ευάλωτοι σε κατάρρευση. Οι φλέβες, οι αρτηρίες, οι αεραγωγοί και άλλες σωληνοειδείς δομές που βρίσκονται σε ζωντανούς οργανισμούς μπορούν να περιγραφούν ως πτυσσόμενοι σωλήνες. Σε συγκεκριμένες περιπτώσεις, η διερεύνηση των οποίων δεν είναι ο στόχος αυτής της διατριβής, αυτές οι σωληνοειδείς κατασκευές είναι επιρρεπείς σε ατέλειες που μπορεί να οδηγήσουν σε κατάρρευση και διάδοση ύβωσης υπό ομοιόμορφη εξωτερική πίεση. Σε αυτή τη διατριβή, στόχος ήταν η προσομοίωση της συμπεριφοράς των πτυσσόμενων σωλήνων όταν εφαρμόζεται οβαλότητα και ομοιόμορφη εξωτερική πίεση. Σωλήνες με λεπτό και παχύ τοίχωμα, με πέντε διαφορετικές αναλογίες διαμέτρου προς πάχος, μελετώνται αριθμητικά χρησιμοποιώντας προσομοιώσεις πεπερασμένων στοιχείων στο ABAQUS. Τρισδιάστατα μοντέλα φέτας και μοντέλα μακριών σωλήνων έχουν θεωρήθηκαν οι βασικές περιπτώσεις αυτής της διπλωματικής, προκειμένου να διερευνηθεί η πίεση διάδοσης ύβωσης που εξάγεται από τις αποκρίσεις πίεσης-όγκου τους αλλά και οι συνθήκες επαφής κατά την διάδοση ύβωσης. Το υλικό Deformation Theory χρησιμοποιήθηκε ως μοντέλο μη γραμμικού ελαστικού υλικού. Μια παραμετρική διερεύνηση διεξάχθηκε με σκοπό να εξεταστούν οι επιδράσεις των εκθετών υλικού, του τύπου στοιχείου και της πυκνότητας πλέγματος που εφαρμόζονται στα βασικά μοντέλα. Επιπλέον, διερευνήθηκε η επίδραση της γεωμετρίας του δακτυλίου μέσω αναλύσεων τρισδιάστατων μοντέλων. Πραγματοποιήθηκαν επίσης παραμετρικές αναλύσεις για τη σχέση μεταξύ του τύπου του στοιχείου και της επίδρασής του στην πίεση διάδοσης ύβωσης. Επίσης, η επίδραση της αρχικής οβαλότητας διερευνήθηκε με την κατασκευή δισδιάστατων μοντέλων. Οι αποκρίσεις κατάρρευσης των μοντέλων 2D εξετάζονται για ελαστικό υλικό και τα αποτελέσματα συγκρίνονται με αναλυτικές λύσεις. Συνολικά, τα κύρια συμπεράσματα που εξάγονται από την τρισδιάστατη ανάλυση είναι ότι η πίεση διάδοσης ύβωσης εξαρτάται από τον εκθέτη υλικού του Deformation Theory, από τη γεωμετρία των σωλήνων αλλά και από τον τύπο

στοιχείου της μοντελοποίησης. Ωστόσο είναι ανεξάρτητη από την πυκνότητα του πλέγματος που χρησιμοποιείται στη μοντελοποίηση. Καθώς ο εκθέτης υλικού αυξάνεται, η πίεση διάδοσης ύβωσης μειώνεται. Επιπλέον, καθώς η διατομή του σωλήνα γίνεται πιο λεπτή, η έκταση του πλατώ, από το οποίο εξάγεται η τιμή της διάδοσης ύβωσης, μειώνεται. Επίσης, ο τύπος στοιχείου που χρησιμοποιείται στην μοντελοποίηση δεν επηρεάζει τις συνθήκες επαφής της διάδοσης της ύβωσης, όταν ο εκθέτης υλικού παραμένει σταθερός. Τέλος, τα συμπεράσματα από τα δισδιάστατα μοντέλα υπογραμμίζουν ότι καθώς αυξάνεται η αρχική τιμή ατέλειας, αυξάνεται επίσης η απόκλιση της πίεσης κατάρρευσης από την καμπύλη της ιδανικής περίπτωσης, οδηγώντας σε κατάρρευση υπό χαμηλότερες πιέσεις.

Table of contents

Acknowledgements **v**

Abstract **vi**

Περίληψη **viii**

Table of contents **xi**

List of figures **xiv**

List of tables **xix**

1 Introduction **1**

1.1 Problem motivation 1

1.2 Literature Review 2

1.2.1 Airway collapse cases 2

1.2.2 Collapse Cases of Elastic Tubes 3

1.2.3 Collapse in Veins and Arteries 4

1.2.4 Collapsible tube models 5

1.2.5 Buckle propagation 6

1.3 Collapse in metal tubes 7

1.4 Problem Statement 7

2 Theory of collapse under external pressure **9**

2.1 Buckling of a ring 9

2.1.1 Theoretical post-buckling 10

2.2 Buckling Propagation 10

2.2.1 Maxwell line 11
2.3 Material Theory 12
2.3.1 Deformation Theory 12
2.3.2 Hyperelastic Materials 12
2.4 Initial Imperfections 13

3 Modeling 15
3.1 Two-dimensional models 16
3.1.1 Numerical modeling for 2D models 16
3.1.2 ABAQUS modeling for 2D models 18
3.2 Three-dimensional base case models 19
3.2.1 Numerical modeling for 3D slice and 3D long tube models 19
3.2.2 ABAQUS modeling for 3D slice models 20
3.2.3 ABAQUS modeling of 3D long tube models 21
3.3 Material modeling 22

4 Parametric Investigation 26
4.1 Material exponents 26
4.2 Element Type Investigation 31
4.2.1 Three-dimensional slice modeling 31
4.2.2 Results of element investigation 32
4.3 Mesh Investigation 34
4.3.1 Modeling 34
4.3.2 Results of mesh density investigation 35

5 Results for 2D elastic models 37

6 Results for 3D Base Case Models 39
6.1 Three-dimensional slice results 39
6.1.1 Estimation of propagation pressure for 3D slice models 39
6.1.2 Mises Stresses and Logarithmic Strains 46
6.2 Three-dimensional long tubes results 46
6.2.1 Estimation for propagation pressure of 3D long tube base case models 46
6.2.2 Comparison results of C3D20R and SC8R Element types 59

6.2.3 Contact conditions 62
6.3 Summarized results for 3D slice and long tube models 62

7 Conclusions and Discussion 64
7.1 Conclusions for 2D models 64
7.2 Conclusions for 3D slice models 64
7.3 Conclusions for 3D long tube models 65
7.3.1 Comparison between C3D20R and SC8R Element types 66
7.4 Comparison between 3D slice and 3D long tube models 67

8 Future Work 68

Bibliography 70

APPENDIX 77

Matlab codes 78

List of figures

2.1 The variation of external pressure P with volume change dV for a thick-walled collapsible tube ($D/t = 20$) of nonlinear elastic material (Chapter 6). 10

2.2 Pressure-change of Area response, Mawell Line. 12

2.3 Initially ovalized ring. 14

3.1 The two-dimensional slice model of $D/t = 20$ with 100 elements in the circumferential direction and 10 elements in the direction of thickness. . . . 19

3.2 The three-dimensional slice model of $D/t = 20$ used in the finite element analyses of $D/t = 12$ and $D/t = 30$ also. 21

3.3 The three-dimensional long tube model of length $L = 40D$ and $D/t = 20$ used in the finite element analyses of pipes with $D/t = 12$ and $D/t = 30$ also. 22

3.4 Stress-Strain figure with material exponents of Deformation theory utilized for the base case models. 23

3.5 Stress-Strain figure with Ogden hyperelastic formula compared with the selected material exponents of deformation theory model material. 24

3.6 Stress-Strain figure with Ogden hyperelastic formula compared with the selected material exponents of deformation theory model material for a wider range. 24

4.1 Stress-Strain figure with the material exponents of Deformation theory that were investigated. 27

4.2 Pressure-change of area response for the slice with $D/t = 12$, initial ovality 0.2% and material exponent $n = 2$. 27

4.3 Pressure-change of area response for the slice with $D/t = 12$, initial ovality 0.2% and material exponent $n = 2.4$. 28

4.4 Pressure-change of area response for the slice with $D/t = 12$, initial ovality 0.2% and material exponent $n = 2.6$. 28

4.5 Pressure-change of area response for the slice with $D/t = 12$, initial ovality 0.2% and material exponent $n = 2.8$. 29

4.6 Pressure-change of area response for the slice with $D/t = 12$, initial ovality 0.2% and material exponent $n = 2.9$. 29

4.7 Pressure-change of area response for the slice with $D/t = 12$, initial ovality 0.2% and material exponent $n = 3.1$. 30

4.8 Pressure-change of area response for the slice with $D/t = 12$, initial ovality 0.2% and material exponent $n = 3.5$. 30

4.9 Pressure-change of area response of C3D8 finite element type for the elastic ring of $D/t = 40$ with initial ovality 0.2% compared with the theoretical post-buckling curve. 32

4.10 Pressure-change of area response of C3D8R finite element type for the elastic ring of $D/t = 40$ with initial ovality 0.2% compared with the theoretical post-buckling curve. 33

4.11 Pressure-change of area response of SC8R finite element type for the elastic ring of $D/t = 40$ with initial ovality 0.2% compared with the theoretical post-buckling curve. 33

4.12 Pressure-Pressure-change of area response of C3D20R finite element type for the elastic ring of $D/t = 40$ with initial ovality 0.2% compared with the theoretical post-buckling curve. 34

4.13 Pressure-change of area response for the slice with $D/t = 30$, initial ovality 0.2%, exponent $n = 2.6$ and mesh consisting of 40 elements in the circumferential and 5 elements in thickness direction. 35

4.14 Pressure-change of area response for the slice with $D/t = 30$, initial ovality 0.2%, exponent $n = 2.6$ and mesh consisting of 25 elements in the circumferential and 3 elements in thickness direction. 36

4.15 Comparison of Pressure-change of area responses for the slices with $D/t = 30$, initial ovality 0.2%, exponent $n = 2.6$ and mesh consisting of 25,3 and 40,5 elements in the circumferential and in thickness direction respectively. 36

5.1 Responses of ovalities $0.2\%, 0.5\%, 0.7\%, 1\%, 5\%$ and 10% for $D/t = 10$ compared with Theoretical Post-Buckling curve. 37
5.2 Responses of ovalities $0.2\%, 0.5\%, 0.7\%, 1\%, 5\%$ and 10% for $D/t = 20$ compared with Theoretical Post-Buckling curve. 38
5.3 Responses of ovalities $0.2\%, 0.5\%, 0.7\%, 1\%, 5\%$ and 10% for $D/t = 40$ compared with Theoretical Post-Buckling curve. 38

6.1 Pressure-change of area response for slice with $D/t = 20$, initial ovality 0.2% and material exponent $n = 2.4$. 40
6.2 Pressure-change of area response for slice with $D/t = 20$, initial ovality 0.2% and material exponent $n = 2.6$. 40
6.3 Pressure-change of area response for slice with $D/t = 20$, initial ovality 0.2% and material exponent $n = 2.8$. 41
6.4 Pressure-change of area response for slice with $D/t = 20$, initial ovality 0.2% and material exponent $n = 2.9$. 41
6.5 Pressure-change of area response for slice with $D/t = 30$, initial ovality 0.2% and material exponent $n = 2.4$. 42
6.6 Pressure-change of area response for slice with $D/t = 30$, initial ovality 0.2% and material exponent $n = 2.6$. 42
6.7 Pressure-change of area response for slice with $D/t = 30$, initial ovality 0.2% and material exponent $n = 2.8$. 43
6.8 Pressure-change of area response for slice with $D/t = 30$, initial ovality 0.2% and material exponent $n = 2.9$. 43
6.9 Pressure-change of area responses for slice models with $D/t = 12$ and initial ovality 0.2% varying in material exponent values $2.4, 2.6, 2.8$ and 2.9. . . . 44
6.10 Pressure-change of area responses for slice models with $D/t = 20$ and initial ovality 0.2% varying in material exponent values $2.4, 2.6, 2.8$ and 2.9. . . . 45
6.11 Pressure-change of area responses for slice models with $D/t = 30$ and initial ovality 0.2% varying in material exponent values $2.4, 2.6, 2.8$ and 2.9. . . . 45
6.12 Pressure-change of volume response for tube with $D/t = 12$, initial ovality 0.2% and material exponent $n = 2$. 47
6.13 Pressure-change of volume response for tube with $D/t = 12$, initial ovality 0.2% and material exponent $n = 2.4$. 47

6.14 Pressure-change of volume response for tube with $D/t = 12$, initial ovality 0.2% and material exponent $n = 2.6$. 48
6.15 Pressure-change of volume response for tube with $D/t = 12$, initial ovality 0.2% and material exponent $n = 2.8$. 48
6.16 Pressure-change of volume response for tube with $D/t = 12$, initial ovality 0.2% and material exponent $n = 2.9$. 49
6.17 Pressure-change of volume response for tube with $D/t = 20$, initial ovality 0.2% and material exponent $n = 2$. 49
6.18 Pressure-change of volume response for tube with $D/t = 20$, initial ovality 0.2% and material exponent $n = 2.4$. 50
6.19 Pressure-change of volume response for tube with $D/t = 20$, initial ovality 0.2% and material exponent $n = 2.6$. 50
6.20 Pressure-change of volume response fortube with $D/t = 20$, initial ovality 0.2% and material exponent $n = 2.8$. 51
6.21 Pressure-change of volume response for tube with $D/t = 20$, initial ovality 0.2% and material exponent $n = 2.9$. 51
6.22 Pressure-change of volume response for tube with $D/t = 30$, initial ovality 0.2% and material exponent $n = 2$. 52
6.23 Pressure-change of volume response for tube with $D/t = 30$, initial ovality 0.2% and material exponent $n = 2.4$. 52
6.24 Pressure-change of volume response for tube with $D/t = 30$, initial ovality 0.2% and material exponent $n = 2.6$ 53
6.25 Pressure-change of volume response for tube with $D/t = 30$, initial ovality 0.2% and material exponent $n = 2.8$. 53
6.26 Pressure-change of volume response for tube with $D/t = 30$, initial ovality 0.2% and material exponent $n = 2.9$. 54
6.27 The numerical simulations of the sequence of buckle propagation phenomenon for the corresponding (1)-(5) stages of pressure-change in volume response ($D/t = 20, n = 2.6$). 55
6.28 The numerical simulations of the sequence of buckle propagation phenomenon for the corresponding (1)-(5) stages of pressure-change in volume response ($D/t = 30, n = 2$). 56

6.29 Pressure-change of volume responses for 3D long tube models with $D/t = 12$ and initial ovality 0.2% varying in material exponent values $2.4, 2.6, 2.8$ and 2.9. 57
6.30 Pressure-change of volume responses for 3D long tube models with $D/t = 20$ and initial ovality 0.2% varying in material exponent values $2.4, 2.6, 2.8$ and 2.9. 58
6.31 Pressure-change of volume responses for 3D long tube models with $D/t = 30$ and initial ovality 0.2% varying in material exponent values $2.4, 2.6, 2.8$ and 2.9. 58
6.32 Pressure-change of volume response for the tube with $D/t = 12$, initial ovality 0.2%, SC8R elements and material exponent $n = 2.4$. 60
6.33 Pressure-change of volume response for the tube with $D/t = 12$, initial ovality 0.2%, SC8R elements and material exponent $n = 2.6$. 60
6.34 Pressure-change of volume response for the tube with $D/t = 12$, initial ovality 0.2%, SC8R elements and material exponent $n = 2.8$. 61
6.35 Pressure-change of volume response for the tube with $D/t = 12$, initial ovality 0.2%, SC8R elements and material exponent $n = 2.9$. 61

8.1 Experimental setup [1] on the left side and vein's blood flow on the right side. 69

List of tables

3.1 Tube Dimensions of "perfect" cross-section for rings with $D/t = 10$, $D/t = 12$, $D/t = 20$, $D/t = 30$ and $D/t = 40$. 16

3.2 Geometric characteristics of tubes with $D/t = 10$ when initial ovalities of $0.2\%, 0.5\%, 0.7\%, 1\%, 5\%$ and 10% are applied. 17

3.3 Geometric characteristics of tubes with $D/t = 20$ when initial ovalities of $0.2\%, 0.5\%, 0.7\%, 1\%, 5\%$ and 10% are applied. 17

3.4 Geometric characteristics of tubes with $D/t = 40$ when initial ovalities of $0.2\%, 0.5\%, 0.7\%, 1\%, 5\%$ and 10% are applied. 17

3.5 Geometric characteristics of tubes with $D/t = 12, D/t = 20$ and $D/t = 30$ when initial ovality equal to 0.2% is applied. 20

4.1 Geometric characteristics of three-dimensional slices with $D/t = 40$ when initial ovality is applied. 31

6.1 Propagation Pressure Values (Pp) for Different D/t Ratios and Material Exponent values. 44

6.2 Comparison of Mises Stress and Logarithmic Strain for Different D/t Ratios and Material Exponents for the condition of collapse in 3D slice models. . . 46

6.3 Propagation Pressure Values (Pp) for Different D/t Ratios and n Exponents. 57

6.4 Comparison of Contact Conditions and Propagation Pressure (Pp) for Different D/t Ratios and Element Types 59

6.5 Contact Conditions for Different D/t Ratios and Material Exponents 59

6.6 Comparison of 3D slices and long tubes propagation pressure values (Pp) for $D/t = 12$ across a range of material exponent values. 62

6.7 Comparison of 3D slices and long tubes propagation pressure values (Pp) for $D/t = 20$ across a range of material exponent values. 63

6.8 Comparison of 3D slices and long tubes propagation pressure Values (Pp) for different $D/t = 30$ ratio across a range of material exponent values. . . 63

Chapter 1

Introduction

1.1 Problem motivation

The analysis and modeling of collapsible tubes under external pressure constitutes an important problem from a mechanical point of view, as it can provide valuable insight into how these tubes behave and interact with their environment under different conditions. Such tubes are commonly used in a variety of industries, including bio-medical devices, automotive, and aerospace, among others. Understanding the mechanical behavior of collapsible tubes is critical in designing and optimizing these systems for optimal performance, reliability, and safety. By modeling these tubes under external pressure, the forces and stresses involved could be determined along with the occurrence of collapse or failure effects. Also potential design improvements can be identified to enhance their mechanical performance. In particular, modeling of collapsible tubes, such as veins or respiratory tubes, can also be applied in the field of biomechanics. Understanding the mechanical behavior of these tubes can help in developing novel medical devices and surgical procedures. For example, modeling the collapse of the human soft palate can aid in designing more effective surgical procedures and oral appliances for treating obstructive sleep.

Veins are one of the most common types of collapsible tubes. Developing reliable models of venous collapse under external pressure has significant practical implications in medicine and biomedical engineering. The collapse of veins, whether pathological or not, can have significant implications for the body's overall physiological function. In pathological cases, venous collapse can lead to venous insufficiency, deep vein thrombosis, and other related disorders, which can cause pain, swelling, skin ulcers, and other complications that significantly affect the patient's quality of life [2]. Accurate modeling of venous collapse under external

pressure may help in designing more effective therapeutic interventions to prevent or treat these conditions. On the other hand, studying the collapse of veins under physiological conditions can provide insights into the body's normal functioning. For instance, the collapse of veins in the lower limbs during exercise or standing can help regulate blood flow and maintain optimal oxygen delivery to the muscles [3]. Accurately modeling venous collapse under different physiological conditions can help in understanding the underlying mechanisms that control these processes. Studies on this topic have shown promising results and highlight the importance of accurate modeling techniques in advancing our knowledge of venous collapse behavior.

1.2 Literature Review

1.2.1 Airway collapse cases

The upper airway is composed of several soft tissues that are surrounded by muscles that help keep the airway open. During sleep, the upper airway muscles are less responsive to negative intrapharyngeal pressure within the throat, which can lead to a narrowing of the airway and partial or complete airway collapse [4], [5]. The negative pressure causes the soft tissues to be pulled inward, further narrowing the airway and increasing resistance to airflow. If the airway collapses completely, breathing stops, resulting in an episode of apnea. Therefore, during sleep, the airway becomes more susceptible to collapsing [6]. This phenomenon appears in patients with obstructive sleep apnea (OSA), which is a sleep disorder characterized by repetitive episodes of partial or complete upper airway obstruction during sleep. Furthermore, the pharyngeal airway in patients with OSA collapses either due to decreased intraluminal pressure or increased external tissue pressure, or due to reduction in the longitudinal tension of the tube. Obesity may increase the collapsibility of the pharyngeal airway due to excessive fat deposition in two distinct locations [7].

In the context of airway collapse, an early review of this topic was presented by Eastwood et al. [8], who aimed to assess the relationship between upper airway collapsibility during general anesthesia and severity of sleep-disordered breathing in awake patients. The results showed that the propensity for upper airway collapse during anesthesia and sleep are related, especially during REM sleep, and suggest that sleep-disordered breathing should be considered in patients with a propensity for upper airway obstruction during anesthesia or

recovery from it. Additionally, in the study of Xu et al. [9] a 3D finite element modeling approach is described in order to simulate airway collapse mechanics in a rat model of obstructive sleep apnea. The results suggest that material properties of different tissue regions, airway shape, and muscle activity all play important roles in airway collapse. Ibbeken et al. [10] used a 3D printed model of the upper airway to measure the critical closing pressure, which is a parameter that characterizes airway collapsibility in obstructive sleep apnea. The researchers examined the effect of airway resistance on deformation behavior by changing the inflow area size. Airway collapse can also occur animals, such as dogs and it's a common cause of chronic cough in middle-aged to older dogs. Lutchen and Gillis [11] studied the impact of airway constriction on lung function and compared the experimental results with the predictions of their computational model. In the same subject was the work of Maggiore [12] who presented tracheal and airway collapse (bronchomalacia) in dogs, which results from the softening of the tracheal cartilage, causing narrowing and impeding the passage of air. A different case, related to airway collapse, the alveolar collapse during diving, was studied by Fitz-Clarke [13]. The author developed a computational model of the human respiratory tract to study airway and alveolar compression and re-expansion during deep breath-hold dives. The model predicts that human lungs collapse beyond 200 m, and that reopening of closed alveoli occurs on ascent beginning at a depth that depends on the maximum depth reached and surfactant properties.

1.2.2 Collapse Cases of Elastic Tubes

Materials that exhibit the behavior of collapsible tubes are elastomers. Elastomers are materials that have the ability to exhibit significant stretching and return to their original shape when the stress is removed. They are often used as the material of choice for modeling collapsible tubes, due to their ability to deform and collapse under external pressure.

An early study with elastomeric material was carried out by Flaherty et al. [14]. The authors investigated the buckling and collapse behavior of an elastic tube under different levels of pressure, determining numerically the pressures at which the tube buckles and contacts at a single point or straight line, and the corresponding cross-sectional buckling. They also determined the fluid flow through the buckled tube, which could have implications for the collapse of veins and blood flow. Fabian [15] examined the collapse behavior of elastomeric tubes under external pressure, by determining both the limit load and the possibility and sig-

nificance of axial wrinkling of the compressed region of the shell prior to the limit load. The study aimed at measuring the pressure-cross sectional area relation of microtubes made of latex and compare the measured perfusion pressure-flow relation with the calculated relation using Poiseuille's law, finding good agreement between the two. A later study was conducted by Bassez et al. [16] who developed a representative model of the behavior of flexible ducts, such as elastic tubes or veins, based on a phenomenological approach of the inflation and collapse of the tube. This model leads to a single "universal" analytical expression of the tube's response that is valid for a wide range of transmural pressures and is more accurate than previous theoretical studies. The model was applied to both experimental data using silicone tubes and physiological data obtained in vivo on human leg veins, and the results were compared. Another approach was conducted by Zhu et al. [17], who formulated and solved a fully nonlinear partial differential equation governing the axisymmetric deformation of a thick-walled circular cylindrical elastic tube subject to external pressure using a finite element method. They found that the nonlinear results significantly depart from linear ones when external pressure and tube wall strain are large, with short tubes exhibiting "corner bulging" and longer tubes exhibiting multiple modes of deformation. Following their earlier study [17], a subset of the authors pursued further research on elastic tubes and presented a numerical simulation model of three-dimensional finite deformation of a thick-walled circular elastic tube, subjected to internal or external pressure. They derived an analytical form of the Jacobian matrix for fast and better numerical convergence and validated the model through comparison with commercial software and previous works. The study's success opened up the possibility of applying the model to fluid-structure interaction studies and modeling complex physiological systems [18]. Finally, Kozlovsky et al. [1], conducted experiments to explore the contours of post-buckling deformation of the cross-section of thick-wall tubes. The authors presented a general constitutive law for describing the behavior of collapsible thin and thick-wall tubes, including their relationship between pressure and cross-sectional area, which can be used to predict the behavior of tubes when subjected to compressive forces.

1.2.3 Collapse in Veins and Arteries

One of the most common applications of collapsible tubes is modeling the structure of veins. Vein collapse can occur for a variety of reasons, and when it comes to a pathological case it could cause several problems to a living organism.

In clinical settings, vein collapse can occur in humans, and more specific in the juxtathoracic zone, during cardiac catheterization [19]. Collapse may also appear during insertion of a central venous catheter into the internal jugular vein. During this procedure, the use of real-time ultrasound-assisted guidance can cause collapse of the vein, due to the production of transcutaneous pressure, resulting the failure of the puncture for catheter insertion [20].

Non-pathological cases of vein collapse are frequent for veins situated higher than the heart and for those compressed by contractions of skeletal muscles, in order to transport blood from the feet of upright mammals back to the heart [21],[22]. For giraffes, in particular, the collapsing of veins has been demonstrated to have a positive effect on controlling the flow rate while they raise their heads [23].

Although veins can collapse because of insufficient internal pressure, arteries typically remain unaffected by collapse due to their thicker walls and the high blood pressure within their lumen [24]. However, under certain circumstances, arteries might collapse, such as when the intramyocardial coronary arteries collapse while the left ventricle contracts. Additionally, It has been proposed that the collapse of arteries can occur in areas just after a narrowing [25],[26], and this can also be caused by blood pressure cuffs [22].

1.2.4 Collapsible tube models

Models of collapsible tubes have been created utilizing the principle of elastic instability to establish the critical pressure at which a blood vessel collapses [24], [25] Such model, presented by Fung [24], demonstrated the equation for buckling in thin-walled cylindrical tubes of linear elastic material with uniform wall thickness when transmural pressure is applied. Flaherty et al. [14] demonstrated the post-buckling behavior of collapsible tubes. They employed an approach using equilibrium and curvature equations, following Fung's methodology, to compute the cross-sectional shapes of long, inextensible, elastic thin-walled circular tubes subjected to various transmural pressures. Also, Kresch and Noordergraaf [27] presented a mathematical examination of how the cross-sectional configuration of a flexible tube alters as the internal pressure fluctuates, with the intention of quantifying the collapse event in veins.

Furthermore, several studies have demonstrated mathematical and experimental models of collapsible tubes, considering fluid flow inside them. In 1982, both Bitbol et al. [28] and Bertram et al. [21] conducted research on small scale collapsible tubes. Bitbol et al. focused

on the fluid mechanics involved in the tube's closure motion, while Bertram et al. presented a simple mathematical model of the unsteady flow. A later study by Rosar and Peskin [29] offered a 3D numerical model to simulate fluid flow through a flexible, collapsible tube using the immersed boundary method.

1.2.5 Buckle propagation

The buckling propagation of cylindrical tubes under external pressure is a very special instability problem and a topic of significant interest in the field of offshore pipeline engineering. The phenomenon refers to the propagation of local collapse in pipelines and other tubular structures subjected to external pressure. When a buckle starts to propagate in a pipeline, it requires a minimum pressure that is significantly lower than the collapse pressure the pipeline is designed for. This leads to the buckle continuing to collapse a long section of the pipeline unless there is an appropriate arresting device or the ambient pressure does not drop below the minimum pressure level required for propagation [30].

There are several papers that collectively provide theoretical, experimental, and numerical approaches to scrutinize buckle propagation. In more details, Mesloh et al. [31] were the first to report on this phenomenon and in 1975 Palmer and Martin [32] developed the initial and simplest model to estimate the propagation pressure of a pipe, leading to a closed-form expression. According to the work of Palmer and Martin [32], the equation approximating the buckle propagation pressure is as follows.

$$P_{pm} = \frac{\pi}{4}\sigma_0 \left(\frac{t}{R}\right)^2 \tag{1.1}$$

where σ_0 is the plastic flow stress (yield stress), t is the pipeline thickness, and R is the pipeline radius. Another study on the propagation pressure was carried out by Kyriakides and Babcock [33]. They conducted a quantitative experimental study on aluminum tubes and steel alloy tubes, and presented an empirical formula that considers the influence of the strain hardening modulus E_1 of the pipe, on the buckle propagation pressure.

$$P_k = \sigma_0 \left[10.7 + 0.54\left(\frac{E_1}{\sigma_0}\right)\right]\left(\frac{t}{2R}\right)^{2.25} \tag{1.2}$$

Kamalarasa and Calladine [34] in 1988 provided a simple improvement of the formula of Palmer and Martin, for the investigation of the pressure required for propagation of a buckle

in a submarine pipeline, and presented experimental data to support it. Buckle propagation phenomenon in pipes under external pressure was further investigated by Liang et al. [35] utilizing experimental, theoretical and numerical approaches. The results showed that external pressure drops to a specific value called buckle propagation pressure once a buckle is initiated and remains constant at this value until the pipe is entirely flattened into a shape resembling a ”dog bone”. Also, the study provided insight into the phenomenon through a series of parametric studies using authenticated shell model and finite element model.

1.3 Collapse in metal tubes

The collapse under external pressure is a phenomenon that has been examined thoroughly in the past. In the context of collapse under external pressure, an early experimental study has been conducted by Kennedy and Venard [36]. The authors found that the graphical solution, incorporating the Von Karman reduced modulus, effectively predicts the inelastic behavior of the material (304 stainless steel) and agrees with test results of the experiment [36]. Moreover, Bai et al [37] conducted finite element analysis on long, thick-walled metal tubes under external pressure, considering factors such as initial ovality, residual stress, and strain-hardening, and validated their approach using experimental data. Multiple studies [38] have revealed that such factors (geometric imperfections, material properties, material anisotropy, residual stresses) influence the collapse response of pipes. However, it is noted, in the study of Yeh and Kyriakides [39], that the most important factor for the definition of the collapse pressure is the initial ovality of the tube. The authors came up to this conclusion combining both experimental and analytical approach. Their cause was to predict the collapse pressure of relatively thick pipes $D/t \approx 12$–30, for the accuracy of which, it is a necessary prerequisite to define the geometric and material parameters of the tubes [39].

1.4 Problem Statement

In the present thesis a finite element simulation of elastic cylindrical shells under external pressure will be presented, motivated by the applications of this problem in biomedical engineering. In more details, in Chapter 2 theory of tube collapse, buckling propagation, examined materials and initial imperfections is presented. In Chapter 3 the Modeling part is exhibited, including the two and three dimensional models (2D and 3D) as well as the modeling of the material utilized . In Chapter 4 a parametric investigation for material exponents

(based on deformation theory), mesh density and element type employed to the base case models is conducted. In Chapter 5 the results from the 2D analysis are provided. Afterwords, in Chapter 6 the outcomes of the 3D slice and long tube models are cited. Finally, the conclusions drawn from this Diploma Thesis alongside recommendations for future research are noted in Chapter 7 and Chapter 8 respectively.

Chapter 2

Theory of collapse under external pressure

2.1 Buckling of a ring

In this section the buckling phenomenon (collapse) under external pressurisation will be discussed. Consider a long tube subjected to compressive stress with a perfect circular geometry. It is highly probable that the ring wall will reach a state of structural instability, resulting in buckling and causing substantial deformation to the ring. As the pipe undergoes elastic deformation, the pressure incrementally increases in direct proportion to the displacement. Simultaneously, the circular cross-section contracts proportionally to the circumferential stress, denoted by $\sigma_\theta = \frac{PR}{t}$. At a critical point, that can be noticed at stage I of figure 2.1 known as the buckling pressure (P_{cr}), the pipe experiences a uniform, axially elongated oval-shaped deformation, with $w = a\cos 2\theta$ which is energetically favorable. While the tube can still sustain the buckling pressure P_{cr}, its stiffness is significantly diminished, nearly approaching zero. Consequently, the buckling pressure represents a limiting condition or a critical state for the pipe's structural integrity [40]. It can be proved that the P_{cr} can be computed from the following classical analytical solution

$$P_{\text{cr}} = \left(\frac{2E}{1-\nu^2}\right)\left(\frac{t}{D_{\text{m}}}\right)^3 \tag{2.1}$$

where D_{m} is the mean diameter, t is the pipe wall thickness, E is the Young's modulus and ν is the Poisson's ratio.In the presence of initial imperfections, such as initial ovality, the resistance of the pipe against collapse decreases as the amplitude of imperfection increases indicating the sensitivity of buckling pressure to initial imperfections.

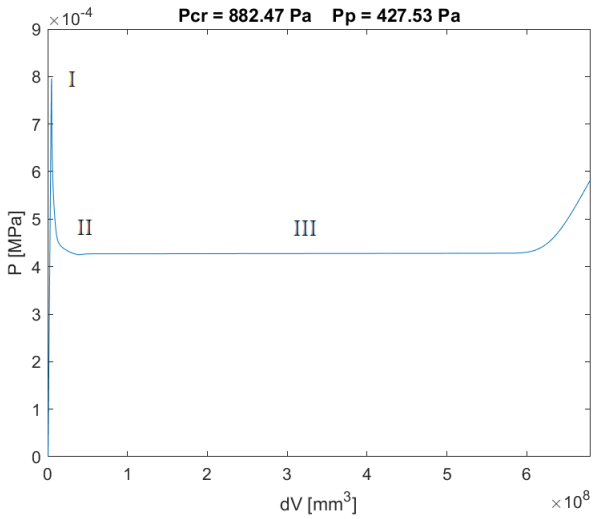

Figure 2.1: The variation of external pressure P with volume change dV for a thick-walled collapsible tube ($D/t = 20$) of nonlinear elastic material (Chapter 6).

2.1.1 Theoretical post-buckling

Budiansky [41] conducted a study on the initial post-buckling response of perfectly elastic rings. Below are the analytical equations derived from this study.

$$P = P_{cr}\left(1 + \frac{27}{32}\Delta^2\right) \tag{2.2}$$

$$P = P_{cr}\left(1 + \frac{9}{16A_0}\Delta A\right) \tag{2.3}$$

where Ao is the initial area enclosed by the undeformed ring, and Δ is a parameter that describes the instant cross-sectional ovalization upon continuing deformation. The ovality parameter will be presented in more detail in section 2.4. Upon reaching the critical pressure, Pcr, the ring undergoes elastic buckling.

2.2 Buckling Propagation

This section focuses in defining the propagation phenomenon and the propagation pressure. As mentioned in subsection 1.2.5 the phenomenon of buckle propagation refers to the propagation of local collapse in tubular structures, such as tubes, subjected to external pressure. In further detail, after the collapse of the pipe's cross-section, the deformation continues and the pressure decreases. Once the cross-section is fully collapsed, with the top and bottom

inner surfaces in contact, the pressure stops decreasing. At this point, depicted in stage II of Figure 2.1, a slight increase in pressure may be observed before the propagation begins and the pressure reaches a constant value in stage III of Figure 2.1. The propagation pressure (P_p) is the minimum pressure needed for the propagation of a buckle. In Figure 2.1, the P_p is represented by the extended horizontal section of the P − ΔV curve following the ”touchdown” point. It serves as a measure of the cylindrical shell’s strength against the phenomenon of progressive flattering, which is determined by the material properties (yield stress) and the diameter-over-thickness ratio. To prevent the buckling propagation in a tube, it is crucial to ensure that the pressure remains below the value of P_p, otherwise, appropriate buckle arrestor devices should be used.

As mentioned in subsection 1.2.5 over the years there have been many attempts to define propagation pressure in the best possible way. One of the earliest estimates was produced by Palmer and Martin [32]. In their approach, they made an assumption that the material was rigid-plastic and exhibited perfect plastic behavior, with no hardening. The dissipated plastic work within the cylinder was determined by considering a ring collapse mechanism, which served as a representation of a specific cross-section of the cylinder during buckle propagation.

2.2.1 Maxwell line

A more accurate estimate of the propagation pressure can be derived using a simple two-dimensional model. Chater and Hutchinson [42] provided a prediction based in the two-dimensional P-ΔA diagram and the balance of energy, which was more accurate than the one proposed by equation 1.1. According to the principle of energy balance, the internal work (W_{int}) must be equal to the external work (W_{ext}). Therefore, according to the authors, the value of buckle propagation can be determined graphically by considering a horizontal line that divides P-ΔA diagram 2.2 into two equal areas (Area1=Area2), above and below it respectively. The numerical formula can be derived by equating the works $W_{\text{int}} = W_{\text{ext}}$, leading to:

$$P_p = \frac{1}{\Delta A} \int_0^{\Delta A} (P\, dA) \tag{2.4}$$

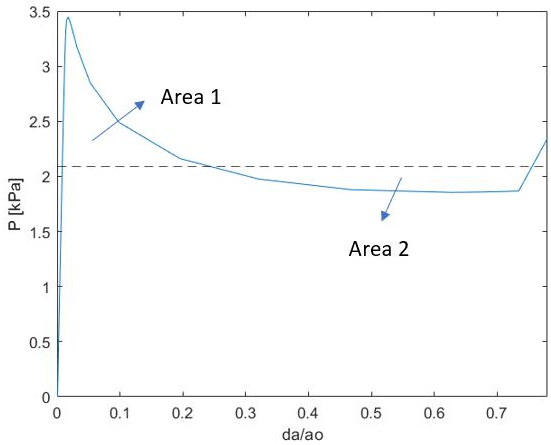

Figure 2.2: Pressure-change of Area response, Mawell Line.

2.3 Material Theory

2.3.1 Deformation Theory

Deformation theory, or total strain theory [43], is a nonlinear elasticity theoretical material model, that under small-displacement conditions, the stress is defined by the total mechanical strain and does not depend on the loading history. The material model, initially proposed by Hencky (1924) [44], posits an unambiguous one-to-one correlation between total strain and total stress, implying that each value of total strain corresponds uniquely to a specific total stress. The one-dimensional model is based on Ramberg-Osgood relationship as described in ABAQUS documentation:

$$E\epsilon = \sigma + \alpha \left(\frac{|\sigma|}{\sigma_0} \right)^{n-1} \sigma \tag{2.5}$$

where σ is the stress, ϵ is the mechanical strain, E is Young's modulus, σ_0 is the "yield" offset, and n is the hardening exponent for the "plastic" (nonlinear) term (n>1).

2.3.2 Hyperelastic Materials

In the context of hyperelastic materials, the behavior is described through a "strain energy potential" that characterizes the amount of strain energy stored per unit of reference volume. This potential is a function of the strain at a given point in the material. Various forms of strain energy potentials exist to model approximately incompressible isotropic elastomers.

These include the Arruda-Boyce form, Marlow form, Mooney-Rivlin form, Neo-Hookean form, Ogden form, Polynomial form, Reduced Polynomial form, Yeoh form, and Van der Waals form.

Among these options, the reduced polynomial and Mooney-Rivlin models can be seen as specific cases of the polynomial model. The Yeoh and neo-Hookean potentials can be considered special cases of the reduced polynomial model. When multiple experimental tests are available, the Ogden and Van der Waals forms tend to provide better accuracy in fitting the experimental results. However, if limited test data are available for calibration, the Arruda-Boyce, Van der Waals, Yeoh, or reduced polynomial forms can still yield reasonable behavior. In cases where only one set of test data (uniaxial, equibiaxial, or planar) is available, the Marlow form is recommended [45].

In this particular thesis, the investigation focused on modeling the material behavior without access to experimental results. To address this limitation, Ogden form for simple extension was utilized [46]:

$$f_1 = \sum_n \mu_n (\lambda_1^{(a_n-1)} - \lambda_1^{((-a_n/2)-1)}) \tag{2.6}$$

where λ is the stretch or extension ratio which approximately relates with the engineering strain (e) with the expression $\lambda = e + 1$.

2.4 Initial Imperfections

As mentioned in the section 1.3 of Chapter1, there are various factors that contribute to the collapse of a tube, with one of the most significant being the presence of initial imperfections in the form of ovality. Ovality measures the extent of a ring's deviation from a perfectly circular shape. This initial ovality can be mathematically represented by the following expression [47].

$$w_o(\theta) = \omega \cos(2\theta) \tag{2.7}$$

where ω is the amplitude of initial oval shape as shown in Figure 2.3. As external pressure is applied, it is anticipated that the amplitude will be increased.

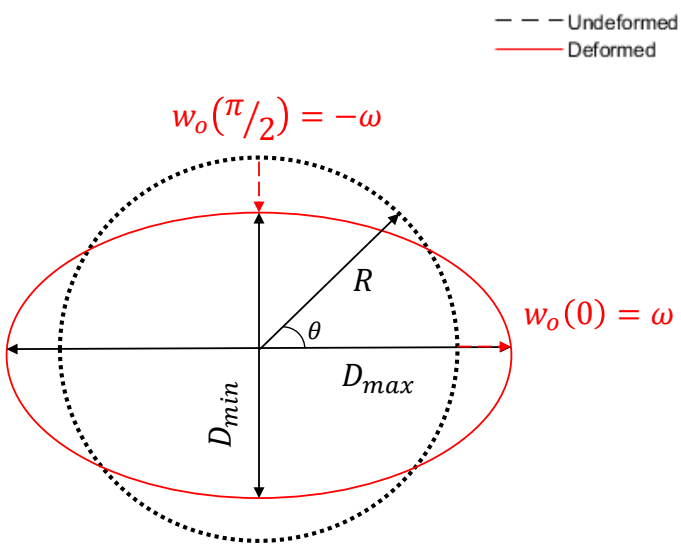

Figure 2.3: Initially ovalized ring.

A more general form of the oval shape of the ring's cross-section is presented in the following form

$$D_\theta = D + 2\omega\cos(2\theta) \tag{2.8}$$

where D_θ is the external diameter of the ellipse at polar angle θ. The value of the initial ovality (Δ_o) that will be applied in the 2D and 3D models is calculated from the following expression [39]:

$$\Delta_o = \frac{D_{\max} - D_{\min}}{D_{\max} + D_{\min}} \tag{2.9}$$

where $D_{\max}$ is the maximum outer diameter of the ring and $D_{\min}$ the minimum. From equation 2.8 maximum and minimum diameters can be exported as:

$$D_{\max} = D + 2\omega \tag{2.10}$$

$$D_{\min} = D - 2\omega \tag{2.11}$$

substituting 2.10 and 2.11 to 2.9 is obtained that

$$\Delta_o = \frac{2\omega}{D} \tag{2.12}$$

where 2/D is the ring's external radius (R), so the final expression for the initial ovality of the ring is

$$\Delta_o = \frac{\omega}{R} \tag{2.13}$$

Chapter 3

Modeling

The modeling part of 2D and 3D dimensional models consists of a numerical modeling part and an ABAQUS modeling part. The construction and analysis of all models took place in ABAQUS software while the post-processing part was conducted using MATLAB. For the numerical part, 2D and 3D slice and 3D long tube models with initial imperfections were created, with different ovalities and variations in wall thickness, using the finite element method. For the two-dimensional models, three different cases of D/t (diameter-to-thickness ratio) were examined ($10, 20$ and 40) across a range of ovality from 0.2% to 10% (0.2%, 0.5%, 0.7%, 1%, 5% and 10%). For the three-dimensional base case models, three different cases of D/t were examined as well but with values equal to 12,20 and 30 only for 0.2% ovality.

Additionally, the application of ovality in models generated elliptical cross-sections in the form of quadrants. Due to the double symmetry of the ring's geometry, only a quarter of the ring is needed for analysis and that's exactly what was considered for all models. For all the cases the same outer diameter ($Dout$) of 550mm was considered. This value refers to very large diameter compared with the extremely small ones of elastic collapsible tubes (e.g veins). Keeping the D/t ratio of the above values the results are also valid for small diameter cases too. Equations 2.10, 2.11 and 2.13 from Section 2.4 were used, given the outer diameter and changing the different ovality values, in order to export the dimensions for the modeling of the tubes. Moreover, dimensions were reduced to the mean diameter (Dm) so, for the processing part, all the results are considered to be in the mean diameter too. In Table 3.1 the geometric characteristics of the "perfect" five different cases of D/t that were investigated in this thesis, are presented.

The values of the diameter-to-thickness ratio considered in this thesis were selected based

on the study conducted by Marzo et al. [48]. The authors performed 3D numerical simulations on thick-walled collapsible tubes. They noted that one of the assumptions of the Kirchhoff–Love thin-shell theory is that the wall thickness of the tube is approximately 20 times smaller than its radius. However, since a significant amount of experimental work focuses on thick-walled tubes ([49], [50]), it is important to extend the analysis beyond thin-shell theory in 3D numerical simulations. Thus, Marzo et al. investigated various cases with different thickness-to-inner radius ratios. Specifically, they examined cases with ratios of $1/20, 0.1/5$, and a thinner case with $t/Rin = 2/20$. Based on the statement of Marzo et al. the diameter-to-thickness ratios (D/t) for this study were selected to be 10, 12, 20, 30 and 40, corresponding to thickness-to-inner radius (t/Rin) values of 0.22, 0.18, 0.11, 0.07 and 0.05, respectively. The selection of the last two cases ($D/t = 30, D/t = 40$) closer to the upper limit of thin-shell theory validity was motivated by the desire to explore the behavior of the tubes near the boundary of thin-shell theory. Therefore, this range range utilized allows for a comprehensive analysis that encompasses both thin and thick walled tubes.

Table 3.1: Tube Dimensions of "perfect" cross-section for rings with $D/t = 10$, $D/t = 12$, $D/t = 20$, $D/t = 30$ and $D/t = 40$.

D/t	D_{out} (mm)	D_{in} (mm)	D_m (mm)	t (mm)	R_{out} (mm)	R_{in} (mm)	R_m (mm)
10	550	450	500	50	275	225	250
12	550	465.38	507.69	42.31	275	232.69	253.845
20	550	497.62	523.81	26.19	275	248.81	261.90
30	550	514.52	532.26	17.74	275	257.26	266.13
40	550	523.17	536.59	13.41	275	261.59	268.29

3.1 Two-dimensional models

3.1.1 Numerical modeling for 2D models

For the two-dimensional cases, three different diameter-to-thickness ratios were examined (10,20 and 40) across a range of ovality from 0.2% to 10% (0.2, 0.5, 0.7, 1, 5 and 10). In Tables 3.2, 3.3 and 3.4 are listed the dimensions that were utilized for the modeling of the tubes with diameter-to-thickness ratio $10, 20$ and 40 respectively.

Table 3.2: Geometric characteristics of tubes with $D/t = 10$ when initial ovalities of $0.2\%, 0.5\%, 0.7\%, 1\%, 5\%$ and 10% are applied.

D/t=10

Δ (%)	R^{out}_{min} (mm)	R^{out}_{max} (mm)	R^{in}_{min} (mm)	R^{in}_{max} (mm)
0.2	274.50	275.50	224.50	225.50
0.7	273.25	276.75	223.25	226.75
5.0	262.50	287.50	212.50	237.50
0.5	273.75	276.25	223.75	226.25
1.0	272.50	277.50	222.50	227.50
10.00	250.00	300.00	200.00	250.00

Table 3.3: Geometric characteristics of tubes with $D/t = 20$ when initial ovalities of $0.2\%, 0.5\%, 0.7\%, 1\%, 5\%$ and 10% are applied.

D/t=20

Δ (%)	R^{out}_{min} (mm)	R^{out}_{max} (mm)	R^{in}_{min} (mm)	R^{in}_{max} (mm)
0.2	274.48	275.52	248.29	249.33
0.7	273.17	276.83	246.98	250.64
5.0	261.90	288.10	235.71	261.90
0.5	273.69	276.31	247.50	250.12
1.0	272.38	277.62	246.19	251.43
10.0	248.81	301.19	222.62	275.00

Table 3.4: Geometric characteristics of tubes with $D/t = 40$ when initial ovalities of $0.2\%, 0.5\%, 0.7\%, 1\%, 5\%$ and 10% are applied.

D/t=40

Δ (%)	R^{out}_{min} (mm)	R^{out}_{max} (mm)	R^{in}_{min} (mm)	R^{in}_{max} (mm)
0.2	274.46	275.54	261.05	262.12
0.7	273.12	276.88	259.71	263.46
5.0	261.59	288.41	248.17	275.00
0.5	273.66	276.34	260.24	262.93
1.0	272.32	277.68	258.90	264.27
10.0	248.17	301.83	234.76	288.41

3.1.2 ABAQUS modeling for 2D models

The goal of this thesis is to simulate the behaviour of a tube under the application of external pressure. ABAQUS Standard Software was utilized, in order to create two-dimensional ring models with initial imperfection in the form of ovality, and MATLAB was used for the post-processing procedure. The model consists of two parts, a two-dimensional deformable body (part 1. in Figure 3.1) that represents the elliptical quadrant and a two-dimensional analytical rigid body (part 2. in Figure 3.1) that is essential for the restriction of the ring's movement. For the modeling of the deformable part a very dense mesh was employed in all cases. More specifically, 100 elements were applied in the circumferential direction for both $D/t = 10$ and $D/t = 20$ cases, and 130 elements for the $D/t = 40$. In the direction of the thickness, 20, 10 and 7 elements were considered for the D/t ratios 10, 20 and 40 respectively. Therefore, the three models were discretized by 2000, 1000 and 910 total number of elements.The descretization for all ring models was made with ”CPE4R” elements, which stands for four-node, reduced-integration, plane-strain elements.

In addition the boundary conditions that were applied to the quadrant elliptic models were ”YSYMM” at the bottom side and ”XSYMM” at the top side and ”ENCASTRE” at a reference point ”RP” of the rigid body. Analytically, ”YSYMM” ensured the restriction of the quadrant's displacement in the y direction and it's rotation about x and z axes, while the ”XSYMM” restricted the movement in x direction and the rotation about y and z axes. Additionally, when the quadrant starts to buckle, the movement of it's top side in the negative y axis is limited by the two-dimensional analytical rigid surface, as mentioned in the beginning of this paragraph. Thus, in order to restrict the displacements and the rotations of the rigid body, it is necessary to include the ”ENCASTRE” boundary condition at an already defined «Reference Point (RP)» of it.

Subsequently, the contact interaction between the two parts had to be defined. For that purpose, the ”surface-to-surface” method was utilized, with the ”master surface” to stand for the analytical rigid surface and the ”slave surface” for the inner surface of the ring. As for the interaction properties of the contact, in order to avoid the translation of the ring through the rigid body, ”Tangential Behavior” with ”Penalty” formulation, ”Isotropic” directionality and friction coefficient equal to zero were applied. Also, ”Normal Behavior” was added to the contact properties, and the pressure-overclosure was selected to be ”Hard Contact”.

Afterwards, a ”Step” needed to be included with the purpose of defining the method

that the analysis of the ring will follow. ”Static,Ricks” method was selected so that the pre-buckling response, the collapse pressure, and the unstable post-buckling response could be obtained. As for the incrementation of the method, estimated total arc length was defined equal to one and the maximum number of increments and the arc length increment depended on each case and changed continuously in order to obtain the desirable outcome of the ring’s collapse. Finally, the external pressure was applied on the outer surface of the quadrant, with ”Uniform” distribution and magnitude equivalent to 0.003.

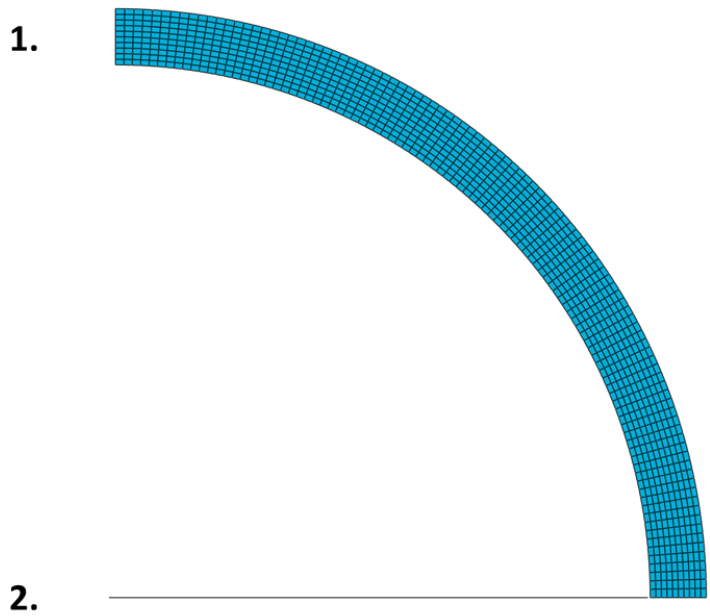

Figure 3.1: The two-dimensional slice model of $D/t = 20$ with 100 elements in the circumferential direction and 10 elements in the direction of thickness.

3.2 Three-dimensional base case models

3.2.1 Numerical modeling for 3D slice and 3D long tube models

For the construction of three-dimensional slice and long tube models with $D/t = 12$, $D/t = 20$ and $D/t = 30$ were considered with an imperfection of initial ovality 0.2%. For the three-dimensional cases, the longitudinal length was deemed to be forty times the diameter of the tube ($L = 40D$). The geometric characteristics of them without the application of initial ovality are presented in Table 3.5 and without the initial ovality in Table 3.1.

Table 3.5: Geometric characteristics of tubes with $D/t = 12$, $D/t = 20$ and $D/t = 30$ when initial ovality equal to 0.2% is applied.

Δ = 0.2 %	$\mathbf{R}^{out}_{min}$ (mm)	$\mathbf{R}^{out}_{max}$ (mm)	$\mathbf{R}^{in}_{min}$ (mm)	$\mathbf{R}^{in}_{max}$ (mm)
D/t=12	274.49	275.51	232.18	233.20
D/t=20	274.48	275.52	248.29	249.33
D/t=30	274.47	275.53	256.73	257.79

3.2.2 ABAQUS modeling for 3D slice models

Similarly to the two-dimensional, three-dimensional models also consists of two parts, a deformable body (part 1. in Figure 3.2) and an analytical rigid body (part 2. in Figure 3.2) except that in this case they are expanding in z direction while serving the same purpose. Commencing with the meshing aspect of ABAQUS modeling, the mesh for the 3D slice models consisted of 25 elements in the circumferential direction, 3 elements in the thickness direction, and 1 element in the longitudinal direction. This discretization approach resulted in a total of 75 elements. The applied mesh can be obtained in Figure 3.2. Additionally, for all the models, a longitudinal length of L=40mm was used as a consistent parameter. The boundary conditions applied to the slice models were ”XSYMM” at the top side of the model along z direction to restrict the displacements x direction and node rotations about the y and z axes, ”YSYMM” to the boundary nodes of the bottom side to constrain the displacements in y direction and rotations about the x and z axes. Also, ”ZSYMM” boundary condition was implemented at the cross sections of planes Z=0 and Z=40mm in order to avoid displacements in z direction and rotations about the x and y axes. Last boundary condition was ”ENCASTRE” that was applied in a ”Reference Point” (RP) that was placed in the analytical rigid surface in order to restrict it’s displacements and rotations. The analysis follows a similar approach as the one explained in Section 3.1.2, utilizing a two-step incremental process. The collapse pressure is computed incrementally using the Riks’ continuation algorithm in the second step of the analysis.

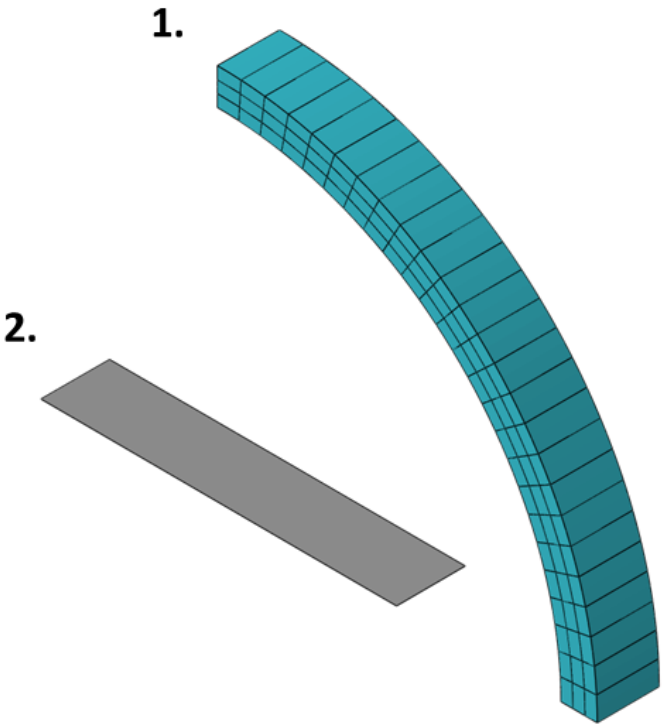

Figure 3.2: The three-dimensional slice model of $D/t = 20$ used in the finite element analyses of $D/t = 12$ and $D/t = 30$ also.

3.2.3 ABAQUS modeling of 3D long tube models

ABAQUS software was utilized for the modeling of three-dimensional models, similar to its application in two-dimensional counterparts and the results extracted were processed in MATLAB. The three-dimensional long tube models consisted of two parts a 3D deformable body (part 1. in Figure 3.3) and an analytical rigid body (part 2. in Figure 3.3) just like the three-dimensional slice case. In more details, the deformable body, considering that its a very long pipe that in a specific spot has an imperfection of elliptical shape, was modeled with one ”perfect” cross-section in the one side and one ”imperfect” with ovality in the other. The ovality applied was 0.2% for each model and the cases examined had diameter to thickness ratio $12, 20$ and 30. The longitudinal length chosen was L=40D for every case. Also, the three boundary conditions of the two-dimensional models are valid for all three-dimensional models extended in the 3-dimensional space, i.e. in the z direction. To the boundary conditions are also considered the symmetry ”ZSYMM”, applied to the ovalized side of the pipe, and

symmetry ”ENCASTRE” to the opposite-with ”perfect” cross section-side. In more details the ”ZSYMM” constrained the displacements in the z axis and zero rotation about y and z axes, while ”ENCASTRE” guaranteed that the ”perfect” side of the ring would remain undeformed. In addition, for the meshing part of the modeling, all three-dimensional cases of D/t consisted 25 elements in the circumferential and 3 elements in the through-thickness direction. As for the axial direction, 250 elements were applied, so the models are descritized by 18750 elements totally. The discretization for the models was performed using ”C3D20R” elements, as determined through the investigation of 3D slice analysis discussed in Section 4.2.2. Also, the contact interaction, the interaction properties, the additional ”Step” and the definition of external pressure are implemented exactly as the ones stated in subsection 3.1.2 for two-dimensional models.

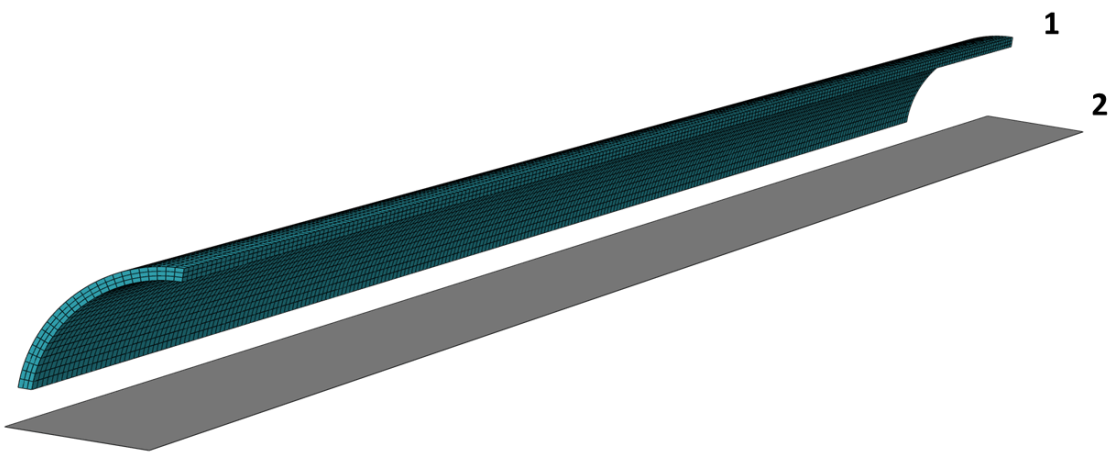

Figure 3.3: The three-dimensional long tube model of length $L = 40D$ and $D/t = 20$ used in the finite element analyses of pipes with $D/t = 12$ and $D/t = 30$ also.

3.3 Material modeling

The material considered for the modeling part in ABAQUS interface was deformation theory. Deformation theory is an idealized material model that represents nonlinear elastic response and the stress-strain curve is given by equation 2.5. The aim of this thesis was to develop models capable of simulating biological tubular structures found in living organisms, such as veins, arteries, upper airways, and other similar biological tubular systems. Based on existing literature, it was determined that collapsible tubes could be effectively represented using hyperelastic materials like silicone rubber [1], considering the potential for significant

displacements and strains in the tube walls. The objective was to use a material that exhibits small deviations from the linear elastic stress-strain curve for a logarithmic strain range of $10.1 - 36.41.4\%$ and stress range 128-652 kPa. These ranges were exported for the condition of contact when the collapse occurs for 3D slice models that are presented in Chapter6. In these ranges, both hyperelastic and deformation theory material model, for specific values of exponent, fulfilled the requirement of small deviations. Also, deformation theory in small stress-strain ranges can be considered as the first part of a hyper-elastic material. However, after conducting research on Ogden hyperelastic model, it was concluded that local instabilities didn't appear, but rather resulted in uniform collapse.

So, in order to investigate the buckling propagation phenomenon, deformation theory was adopted as theoretical nonlinear elastic material model because local instabilities occur in this case. The values of parameters utilized in this thesis encompassed a Young's Modulus of 3.43 MPa, a Poisson's ratio of 0.4 [1], a proportional limit stress of 0.004, and a proportional limit offset of 0.00631, spanning across a range of exponents (n) selected as 2, 2.4, 2.6, 2.8 and 2.9. The selection of these exponents is discussed in Section 4.1 analytically.

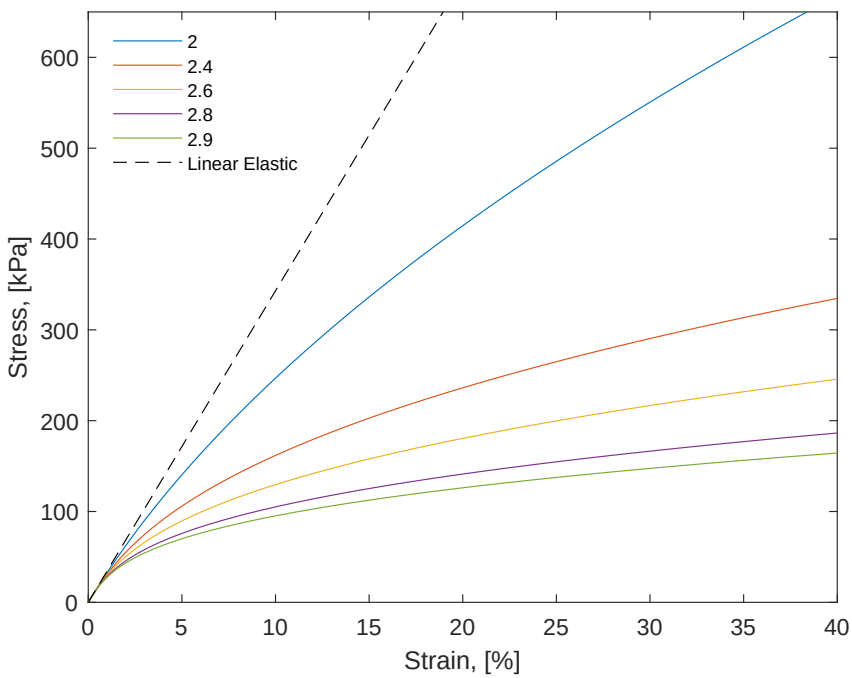

Figure 3.4: Stress-Strain figure with material exponents of Deformation theory utilized for the base case models.

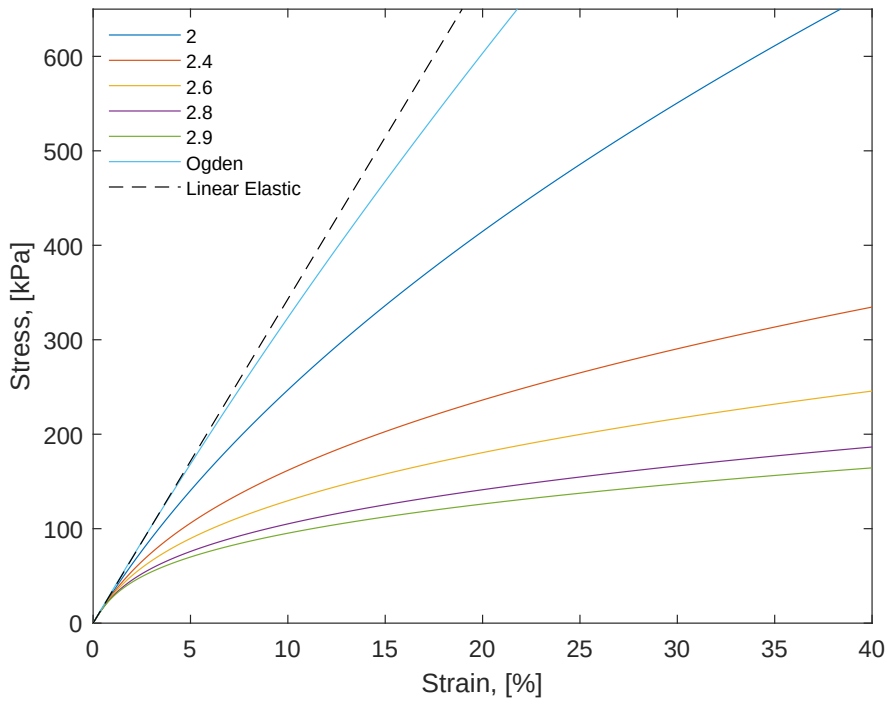

Figure 3.5: Stress-Strain figure with Ogden hyperelastic formula compared with the selected material exponents of deformation theory model material.

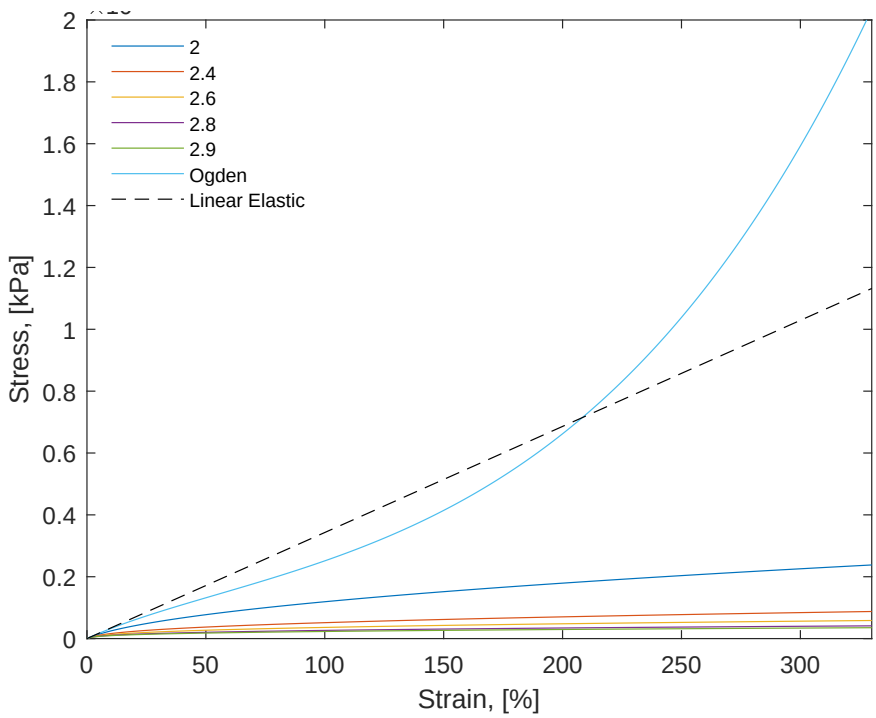

Figure 3.6: Stress-Strain figure with Ogden hyperelastic formula compared with the selected material exponents of deformation theory model material for a wider range.

The Ogden formula utilized for this investigation was extracted from ” The physics of rubber elasticity ” of Treloar [46] and its described in Section 2.3.2. The personalized parameters for the Ogden formula were chosen to be for n=4 : $\alpha_1 = 2$, $\mu_1 = 1.2$, $\alpha_2 = 5$, $\mu_2 = 0.05$, $\alpha_3 = 3$, $\mu_3 = -0.1$, $\alpha_4 = -5$, $\mu_4 = 0$ in order the stress-strain curve to have similar behavior with the picked material exponents of deformation theory model material for the examined range. For a wider range it is observed that Ogden formula's behavior changes, as shown in Figure 3.6. The stress-strain of Ogden formula compared with deformation theory exponents is presented in Figure 3.5.

Chapter 4

Parametric Investigation

This chapter demonstrates the examination that was conducted for the decision-making process, regarding the production of the base case models that are analytically presented in Section 3.2. Firstly, a parametric investigation on the material exponents of deformation theory model material is exhibited. Subsequently, four element types will be examined in order to ascertain which of is more accurate.Finally, two meshes with different densities will be tested with the purpose of determining if the difference in density affects the propagation pressure.

4.1 Material exponents

A parametric study has been conducted in order to investigate the effect of exponent(n) in the parameters of deformation theory model material. In more details, utilizing the Ramberg-Osgood relationship, described in Section 2.3.1, eight different values of exponent (2, 2.4, 2.6, 2.8, 2.9, 3, 3.1, 3.5) were tested and compared with Linear Elastic curve. The results are presented in Figure 4.1, illustrating that as the material exponent decreases, the tangent modulus undergoes an increase. This leads to the stress-strain response approaching the linear elastic curve and exhibiting similar behavior.

Additionaly, the eight different values of exponent were tested for the three-dimensional slice model with diameter-over-thickness ratio 12, the constuction of which was outlined in section 3.2.1. The response obtained by varying the exponents, while keeping the other parameters of deformation theory constant, is presented in the following Figures.

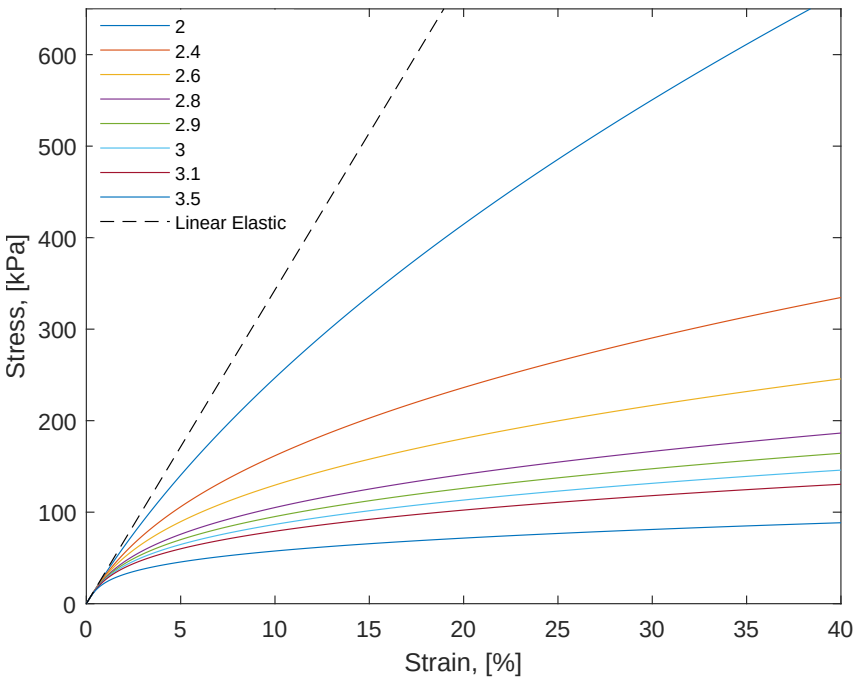

Figure 4.1: Stress-Strain figure with the material exponents of Deformation theory that were investigated.

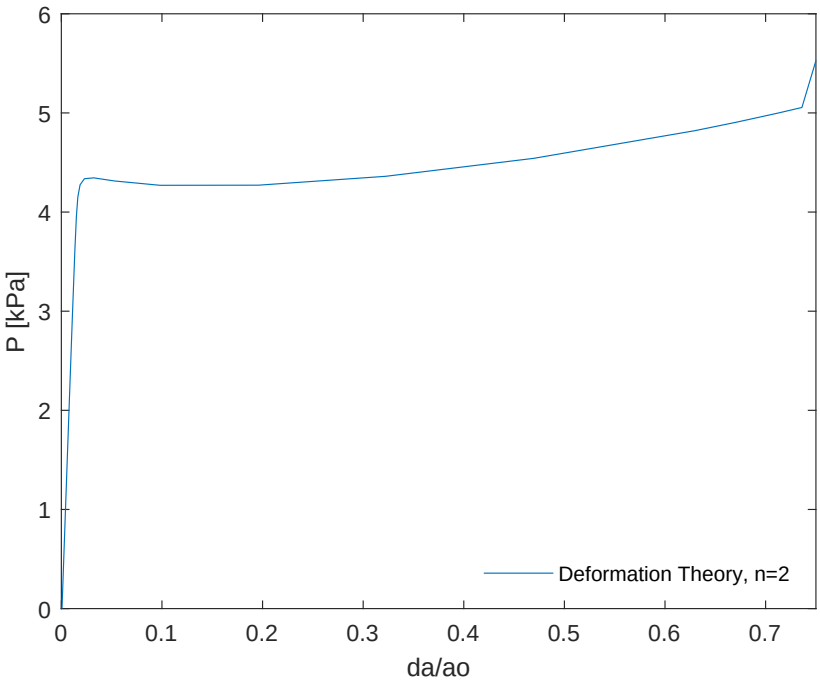

Figure 4.2: Pressure-change of area response for the slice with $D/t = 12$, initial ovality 0.2% and material exponent $n = 2$.

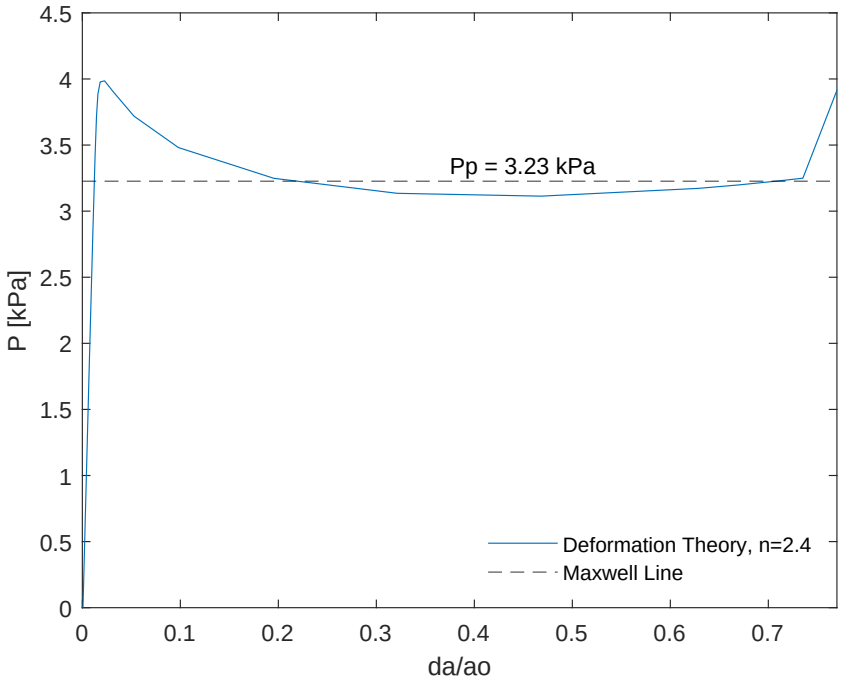

Figure 4.3: Pressure-change of area response for the slice with $D/t = 12$, initial ovality 0.2% and material exponent $n = 2.4$.

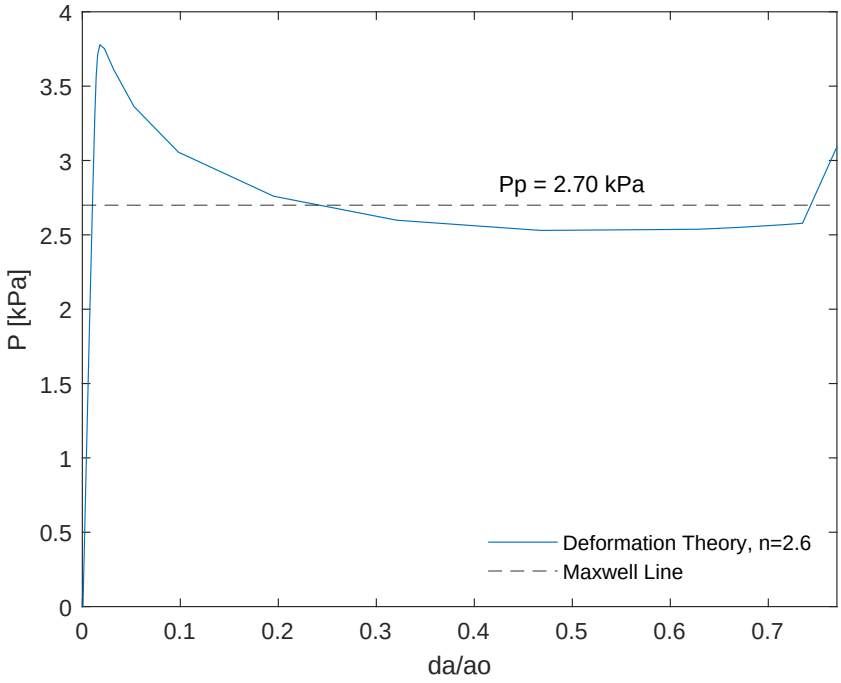

Figure 4.4: Pressure-change of area response for the slice with $D/t = 12$, initial ovality 0.2% and material exponent $n = 2.6$.

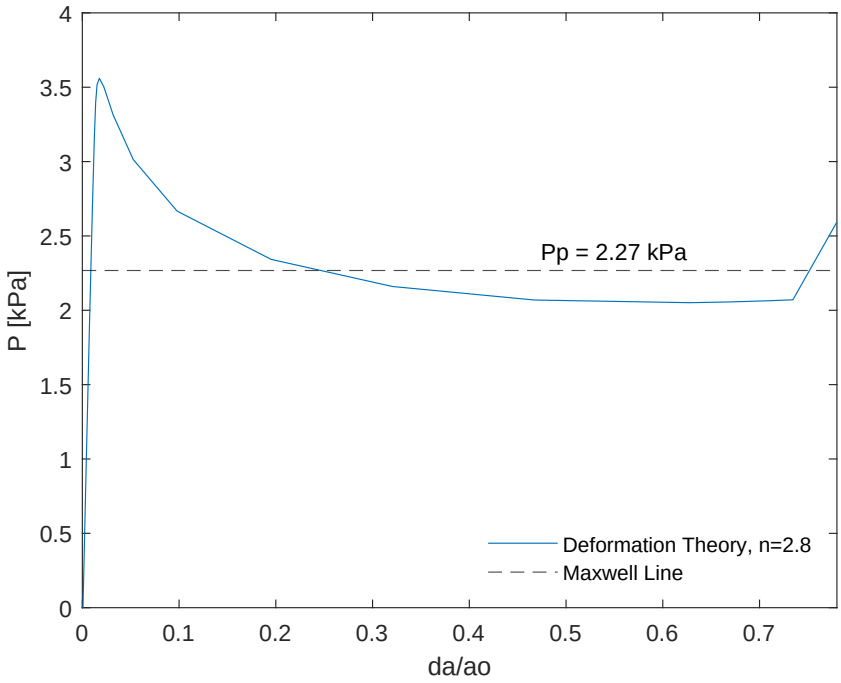

Figure 4.5: Pressure-change of area response for the slice with $D/t = 12$, initial ovality 0.2% and material exponent $n = 2.8$.

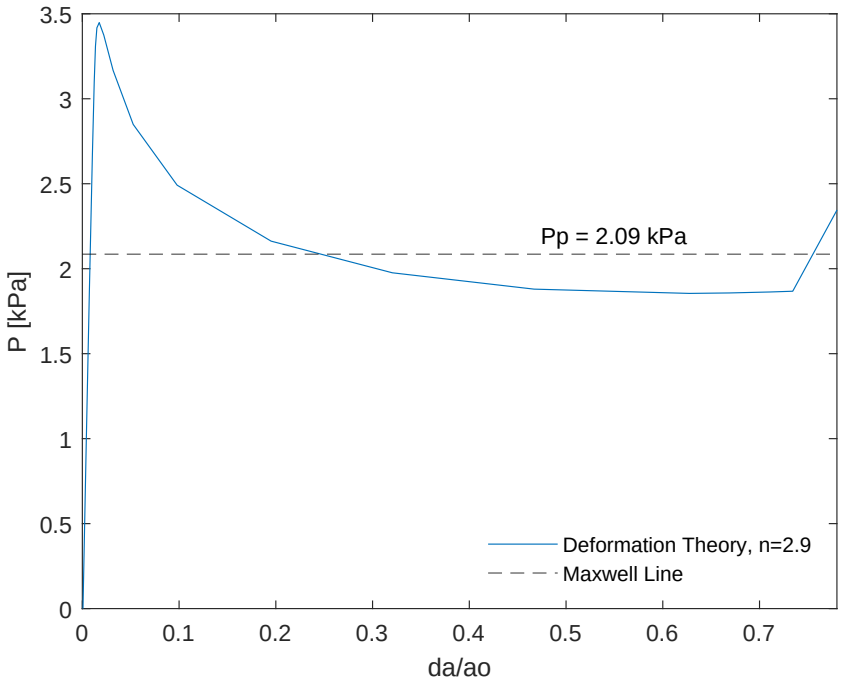

Figure 4.6: Pressure-change of area response for the slice with $D/t = 12$, initial ovality 0.2% and material exponent $n = 2.9$.

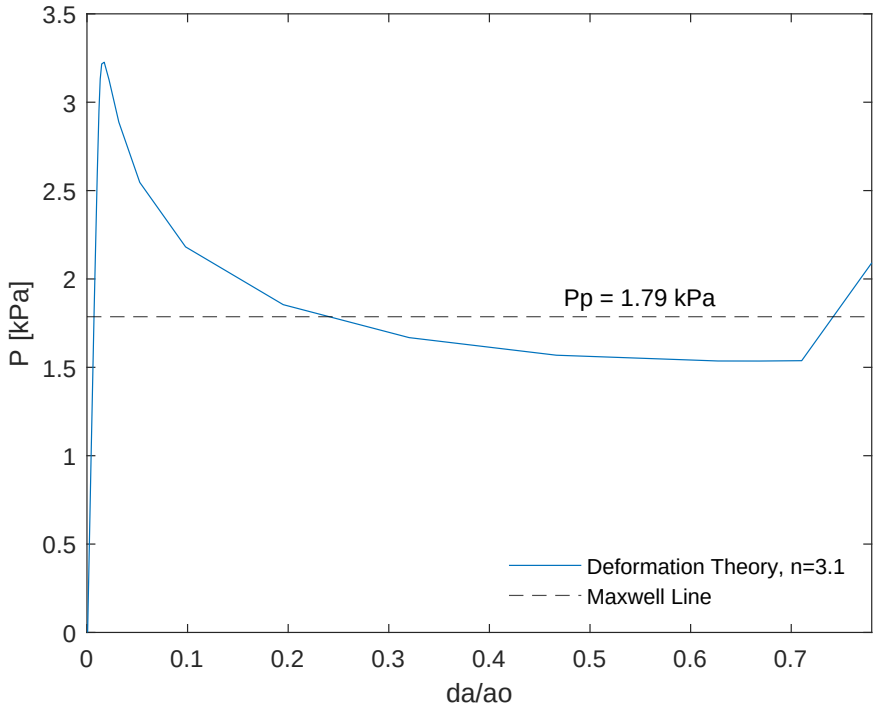

Figure 4.7: Pressure-change of area response for the slice with $D/t = 12$, initial ovality 0.2% and material exponent $n = 3.1$.

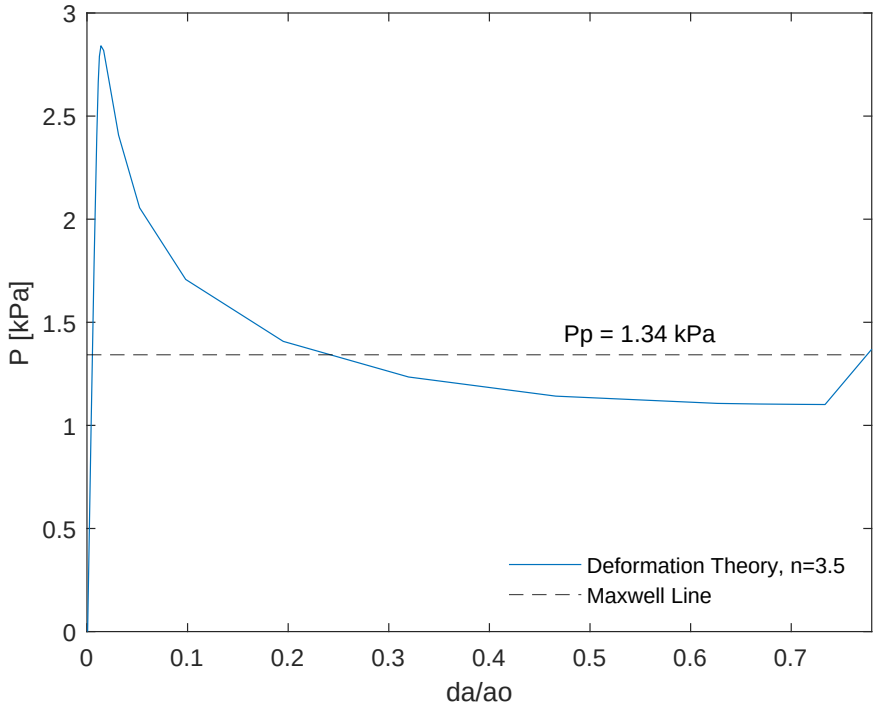

Figure 4.8: Pressure-change of area response for the slice with $D/t = 12$, initial ovality 0.2% and material exponent $n = 3.5$.

From the results of the material exponents above it is concluded that exponent with value $n = 2$ is the one exhibiting smaller deviations from Linear Elastic curve. However,from analyzing the response derived from the 3D slice analysis for D/t=12 in Figure 4.2, it is observed that the post-buckling behavior is significant enough so that the propagation pressure cannot be predicted using the Maxwell line. Additionally, in the analysis of the same model and same case (D/t=12, n=2) in the 3D long tube, as discussed in Chapter 6, it is noted that the propagation pressure can be marginally derived. Therefore, for the purpose of investigating deformation theory material exponents in this thesis and distinguish possible limit cases, values equal to 2, 2.4, 2.6, 2.8 and 2.9 will be examined, while excluding the 3, 3.1 and 3.5 cases because of their big deviation from linear-elastic case exhibited in Figure 4.1.

4.2 Element Type Investigation

In this section the examination of the element typed used in the base case models ($D/t = 12$, $D/t = 20$, $D/t = 30$) presented in Chapter 3, is exhibited. Specifically, four element types were employed: C3D8, C3D8R, C3D20R, and SC8R. The C3D8 elements represent 8-node linear brick elements of full integration, C3D8R denotes 8-node linear brick elements of reduced integration, C3D20R refers to 20-node quadratic brick elements with reduced integration, and SC8R represents 8-node quadrilateral in-plane general-purpose continuum shell elements with reduced integration.

4.2.1 Three-dimensional slice modeling

For the investigation an elastic three-dimensional slice of $D/t = 40$ was considered with initial ovality 0.2%. The geometric characteristics of slices without the application of initial ovality are presented in Table 4.1, and without the initial ovality in Table 3.1. Also, the material of the models was assumed to be elastic, characterized by the following parameters: Young's Modulus (E) of 3.43 MPa and Poisson's ratio (ν) of 0.4. The remainder of the ABAQUS modeling process, regarding the boundary conditions, the analysis and the creation of the "Steps" follows the same procedures outlined in Section 3.2.2.

Table 4.1: Geometric characteristics of three-dimensional slices with $D/t = 40$ when initial ovality is applied.

Δ (%)	R^{out}_{min} (mm)	R^{out}_{max} (mm)	R^{in}_{min} (mm)	R^{in}_{max} (mm)
0.20	274.46	275.54	261.05	262.12

4.2.2 Results of element investigation

For the discretization with eight-node biquadratic plane strain finite elements of reduced and full integration, which are denoted in ABAQUS as C3D8 and C3D8R, the corresponding pressure-change of area responses are shown in Figures 4.9 and 4.10 respectively. Furthermore, the slopes of the post-buckling region for the responses of SC8R, C3D20R can be obtained in Figures 4.11 and 4.12 respectively. The theoretical post-buckling analytical curve 2.3 is included in figures for comparison with the plots derived from the numerical results. For the construction of all figures numerical results were extracted from ABAQUS and processed in MATLAB.

Based on the responses of the following figures, it can be concluded that the C3D20R element type performs better than S3D8, C3D8R, and SC8R element types. This conclusion is drawn from observing that the slope of the post-buckling region of the C3D20R element type is closer to the theoretical post-buckling curve compared to the other cases. Therefore, C3D20R element type was utilized for the construction of the base case models.

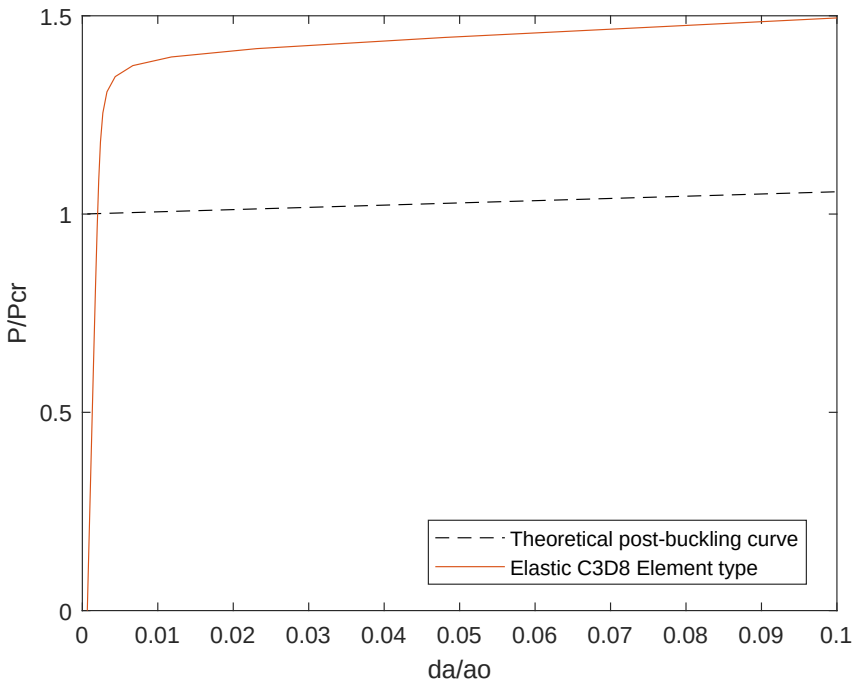

Figure 4.9: Pressure-change of area response of C3D8 finite element type for the elastic ring of $D/t = 40$ with initial ovality 0.2% compared with the theoretical post-buckling curve.

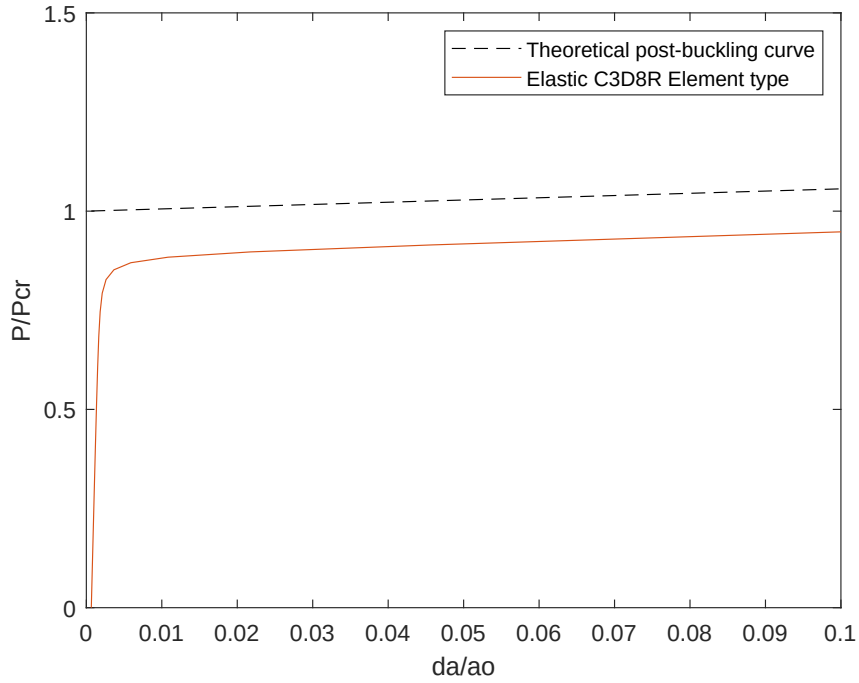

Figure 4.10: Pressure-change of area response of C3D8R finite element type for the elastic ring of $D/t = 40$ with initial ovality 0.2% compared with the theoretical post-buckling curve.

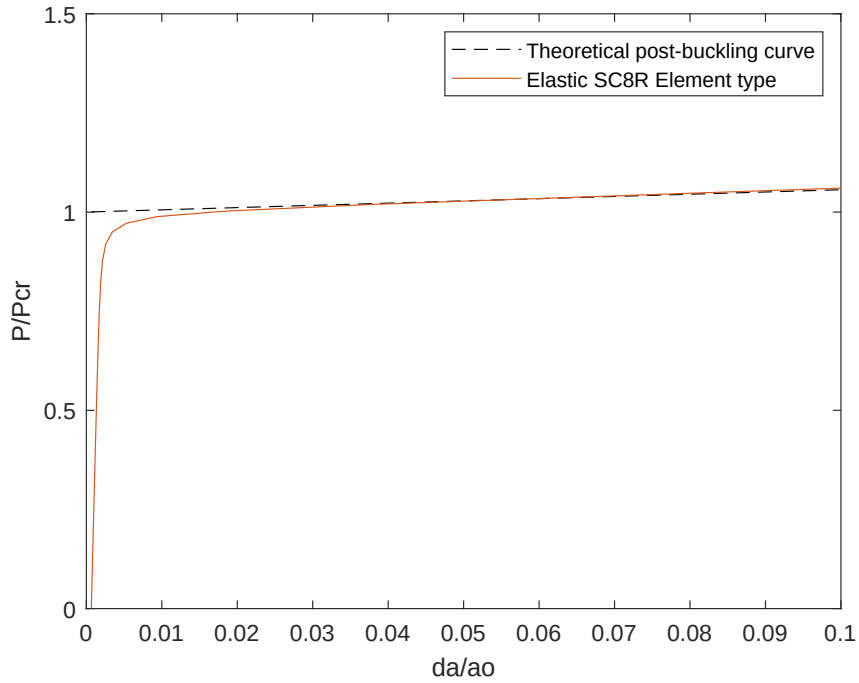

Figure 4.11: Pressure-change of area response of SC8R finite element type for the elastic ring of $D/t = 40$ with initial ovality 0.2% compared with the theoretical post-buckling curve.

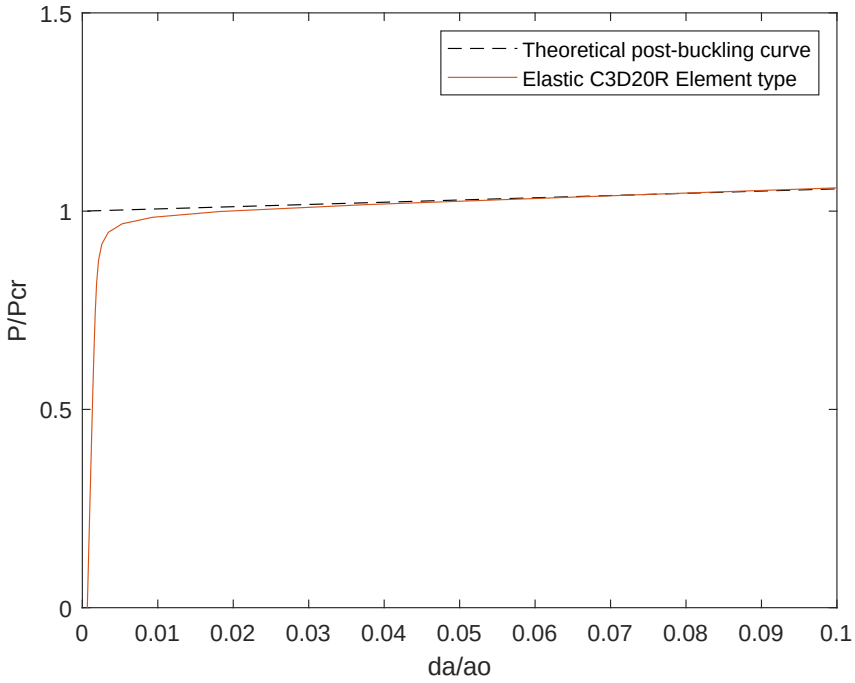

Figure 4.12: Pressure-Pressure-change of area response of C3D20R finite element type for the elastic ring of $D/t = 40$ with initial ovality 0.2% compared with the theoretical post-buckling curve.

4.3 Mesh Investigation

4.3.1 Modeling

In this section, the focus is on examining and discussing the mesh density for the base case models. A three-dimensional slice model was chosen for this examination to obtain quicker and more convenient results. The analysis in this section utilizes a model discussed in Section 3.2.1 with diameter-over-thickness ratio of 30 and material as described in 3.3 with exponent value of $n = 2.6$, Young Modulus of 3.43 MPa, Poisson's ratio of 0.4, yield stress of 0.004, and yield offset of 0.00631. Based on the findings from the previous section, it was determined that the C3D20R element type is the most suitable and accurate choice. So for the investigation regarding the mesh density, the element type remains constant, i.e. C3D20R. However, two different cases were studied, each with a varying number of elements in the hoop and width directions. In more details, for the first case, 25 elements were considered for the hoop direction and 3 for the thickness direction. For the second case, a denser mesh was employed, consisting of 40 elements in the circumferential direction and 5 elements by thickness.

4.3.2 Results of mesh density investigation

The response of the two different cases of mesh density that were investigated is visually presented in the following figures. In order to perform a comparison between them, the estimation of propagation pressure with Maxwell line, as described in Section 2.2.1, was utilized.

From the results of the mesh density investigation in can be concluded that both cases work correctly, with the results in the prediction of propagation pressure to be same for both cases (Figures 4.13 and 4.14). For validation of this conclusion, Figure 4.15 which combines the two responses has been conducted, where it can be obtained that the curves coincide. Consequently, for the construction of the base case models, a mesh density of 25 elements in the circumferential direction and 3 elements in the thickness direction was chosen. This selection was made for the sake of convenience and speed in analyzing the 3D models.

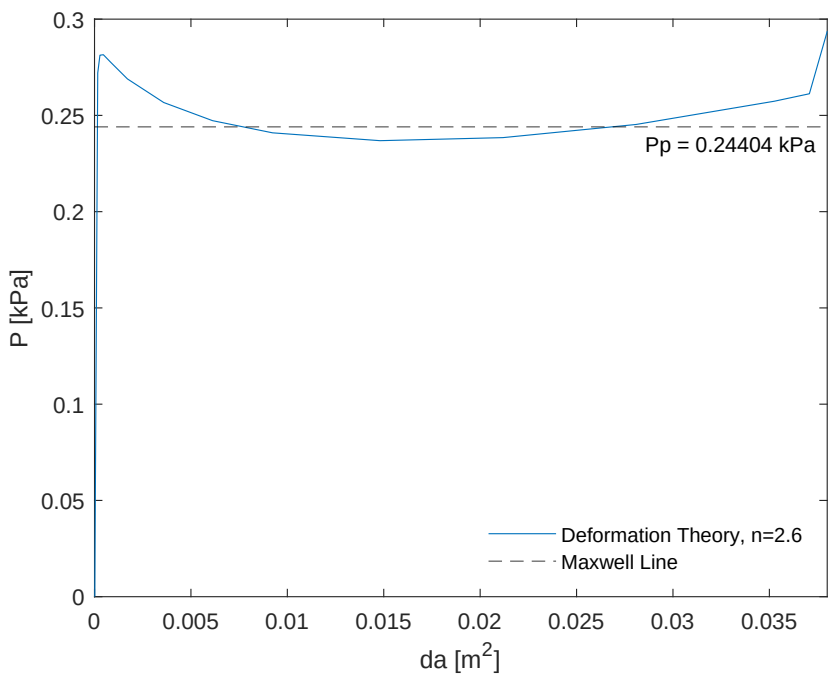

Figure 4.13: Pressure-change of area response for the slice with $D/t = 30$, initial ovality 0.2%, exponent $n = 2.6$ and mesh consisting of 40 elements in the circumferential and 5 elements in thickness direction.

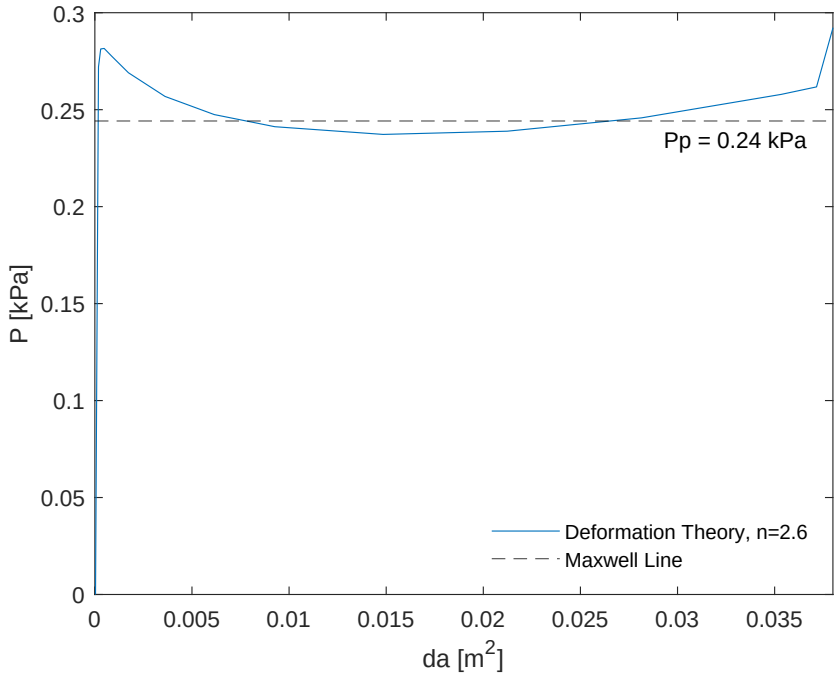

Figure 4.14: Pressure-change of area response for the slice with $D/t = 30$, initial ovality 0.2%, exponent $n = 2.6$ and mesh consisting of 25 elements in the circumferential and 3 elements in thickness direction.

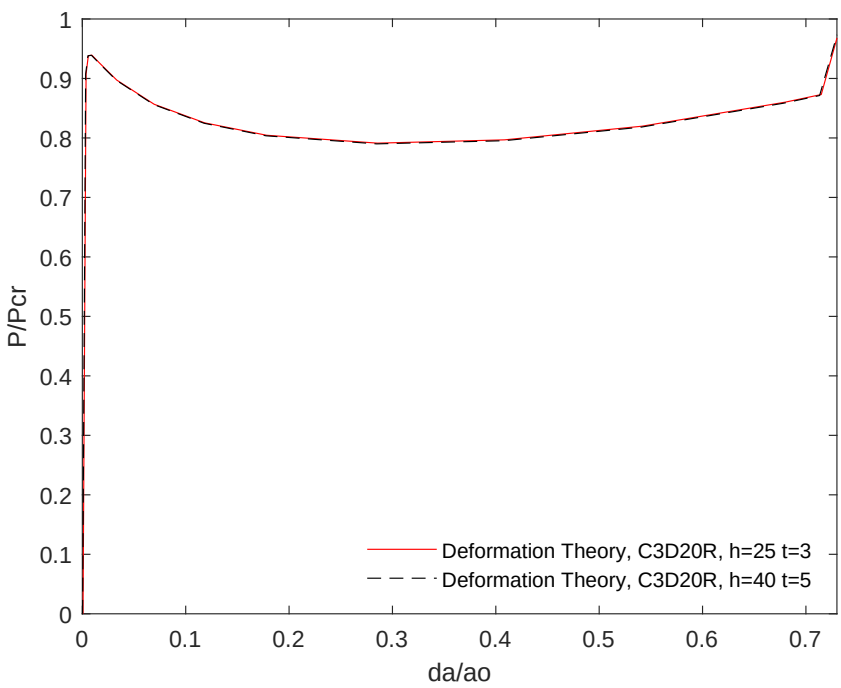

Figure 4.15: Comparison of Pressure-change of area responses for the slices with $D/t = 30$, initial ovality 0.2%, exponent $n = 2.6$ and mesh consisting of 25,3 and 40,5 elements in the circumferential and in thickness direction respectively.

Chapter 5

Results for 2D elastic models

In this Chapter the results for the 2D models described in section 3.1 will be presented. The responses of every geometry examined, namely $D/t = 10$, $D/t = 20$ and $D/t = 40$ are depicted in Figures 5.1, 5.2 and 5.3 respectively. The sensitivity of each tube's response is examined in terms of the initial ovalities embed to the system. These imperfections encapsulate the geometry's deviation from the perfect circle. For every case the plot includes the response of the material for initial ovalities of $0.2\%, 0.5\%, 0.7\%, 1\%, 5\%$ and 10%, alongside the response for a perfect cylindrical tube described from Budiansky [41]. The axis have been non dimensionalized based on the value for buckling pressure (P_{cr} 2.1) and the initial value for the volume enclosed by the tube. An extensive analysis of the results is being conducted in Chapter 7.

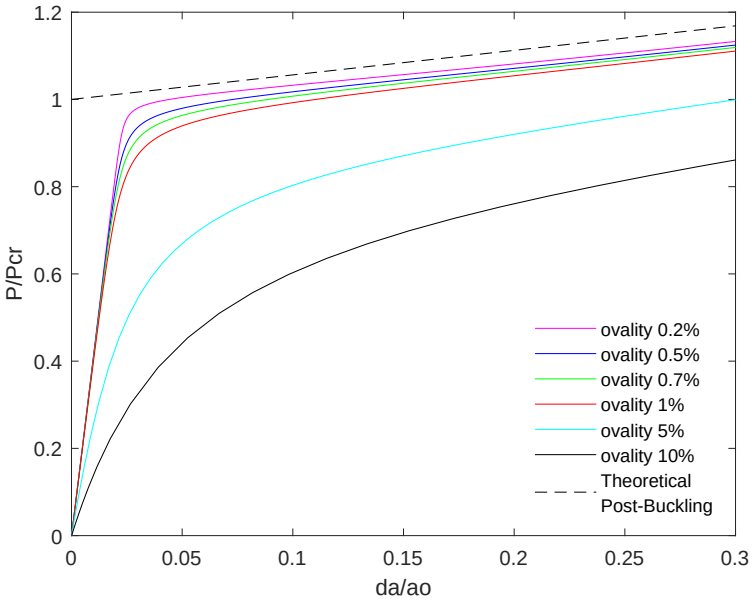

Figure 5.1: Responses of ovalities $0.2\%, 0.5\%, 0.7\%, 1\%, 5\%$ and 10% for $D/t = 10$ compared with Theoretical Post-Buckling curve.

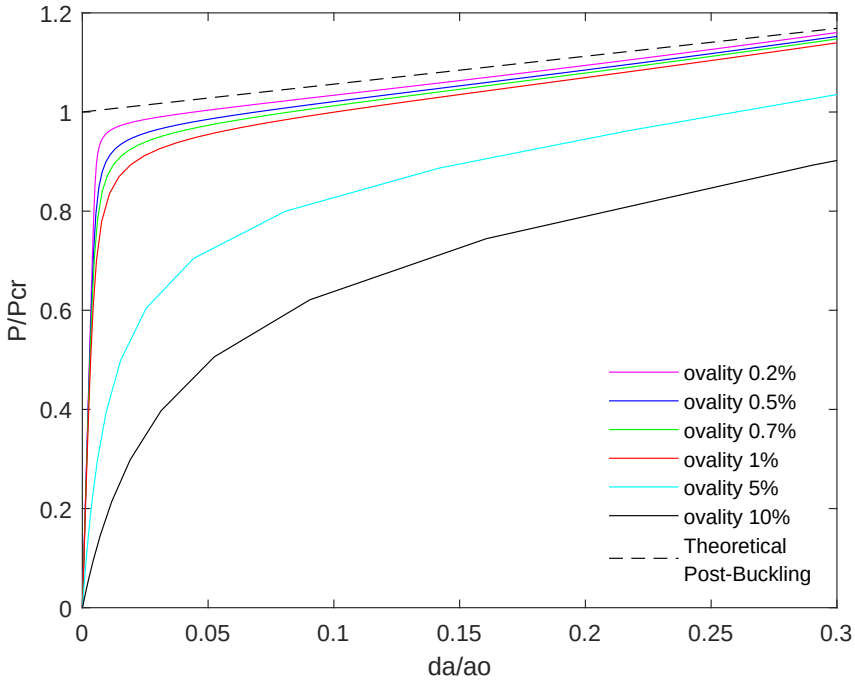

Figure 5.2: Responses of ovalities $0.2\%, 0.5\%, 0.7\%, 1\%, 5\%$ and 10% for $D/t = 20$ compared with Theoretical Post-Buckling curve.

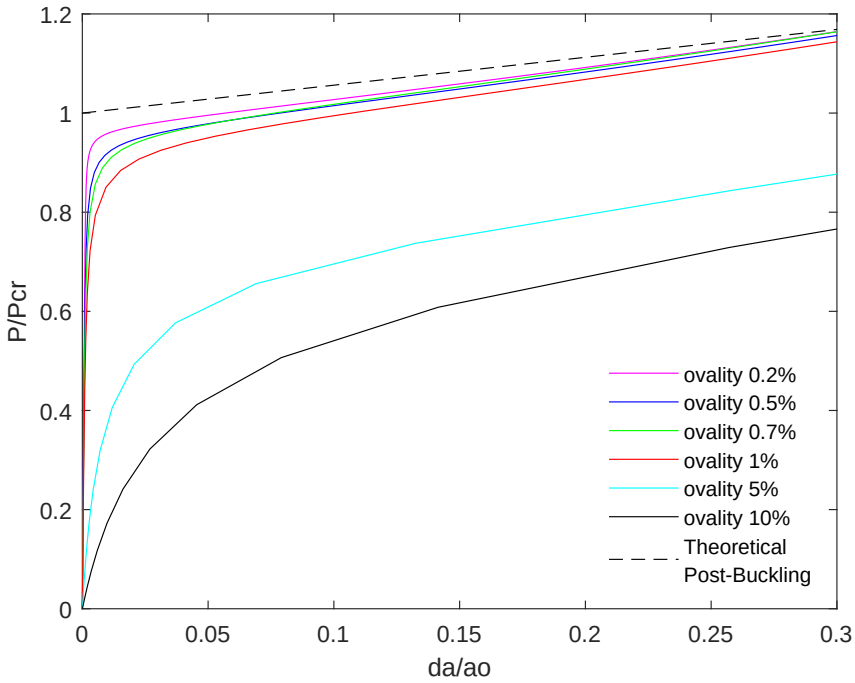

Figure 5.3: Responses of ovalities $0.2\%, 0.5\%, 0.7\%, 1\%, 5\%$ and 10% for $D/t = 40$ compared with Theoretical Post-Buckling curve.

Chapter 6

Results for 3D Base Case Models

In this Chapter the results from the 3D slices and 3D long tube base case models that are described in section 3.2 will be presented. In more details, the estimated propagation pressure will be imported from the three-dimensional slices and long tube models for the three different cases of diameter-over-thickness ratio ($D/t = 12, D/t = 20, D/t = 30$) when ovality of 0.2% is implemented. Subsequently, a comparative assessment will be conducted, juxtaposing the propagation pressure estimates derived from 3D long tubes with those obtained from the slice-based approach. Also, contact conditions of propagation for 3D long tube models will be exhibited.

6.1 Three-dimensional slice results

Based on the numerical modeling of 3D slice models that was presented in section 3.2.1, analysis with ABAQUS numerical framework (Section 3.2.2), has been conducted in order to obtain the response and extract an estimation for propagation pressure of each case.

6.1.1 Estimation of propagation pressure for 3D slice models

For the estimation of the propagation pressure in three-dimensional slice models the theory of Maxwell line, that was described analytically in section 2.2.1, was utilized. The results for the case of diameter-over-thickness ratio equal to 12 with material exponents $2.4, 2.6, 2.8$ and 2.9 have already presented in Section 4.1, were an examination on the exponents was conducted in order to decide what values will be more suitable for utilizing for the base cases of this thesis. Thus, in the following figures the results for the other two cases with $D/t = 20$ and $D/t = 30$ will be exhibited.

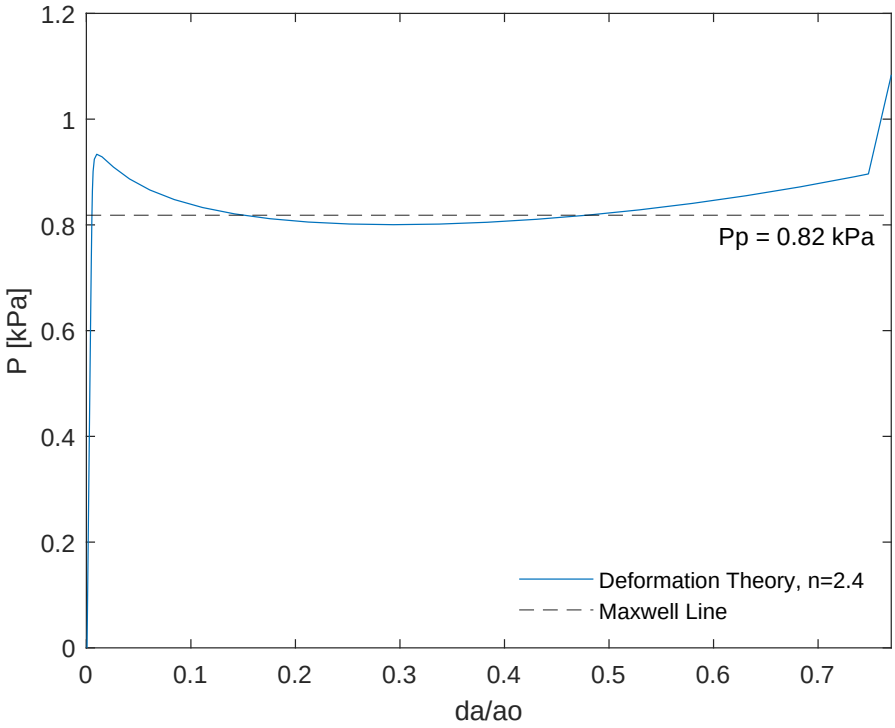

Figure 6.1: Pressure-change of area response for slice with $D/t = 20$, initial ovality 0.2% and material exponent $n = 2.4$.

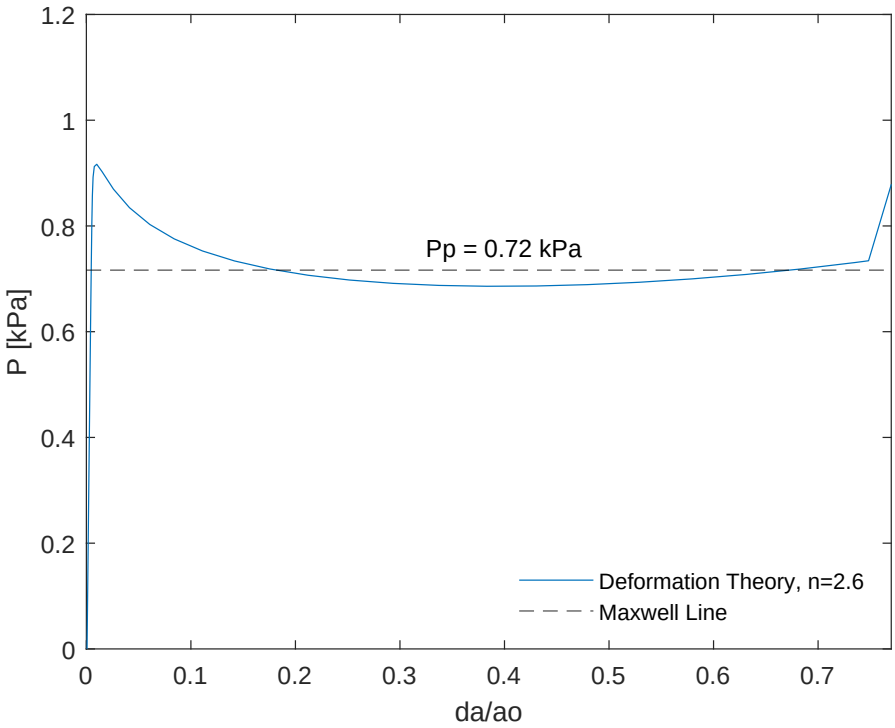

Figure 6.2: Pressure-change of area response for slice with $D/t = 20$, initial ovality 0.2% and material exponent $n = 2.6$.

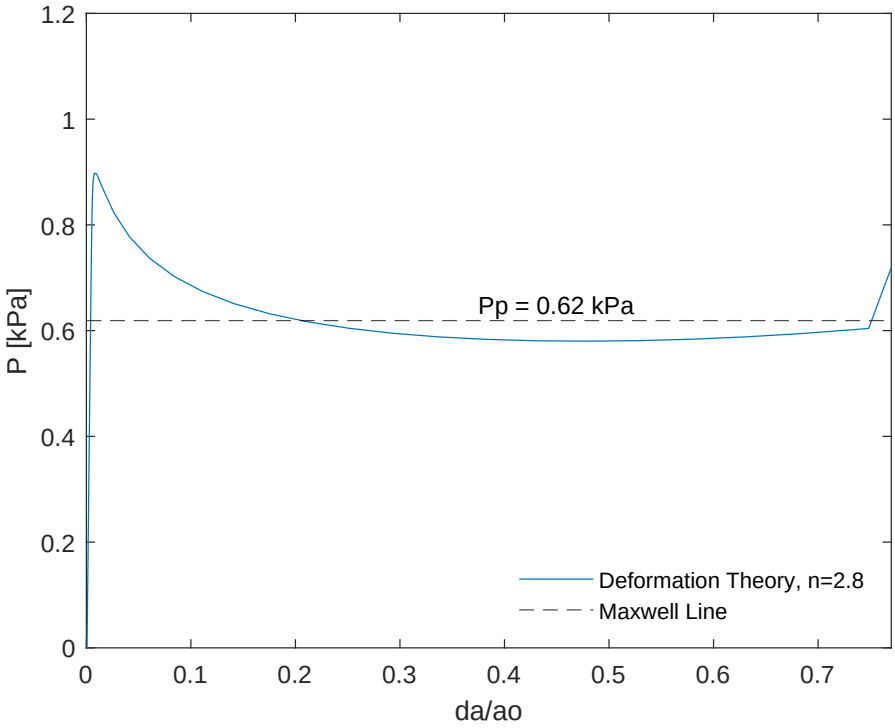

Figure 6.3: Pressure-change of area response for slice with $D/t = 20$, initial ovality 0.2% and material exponent $n = 2.8$.

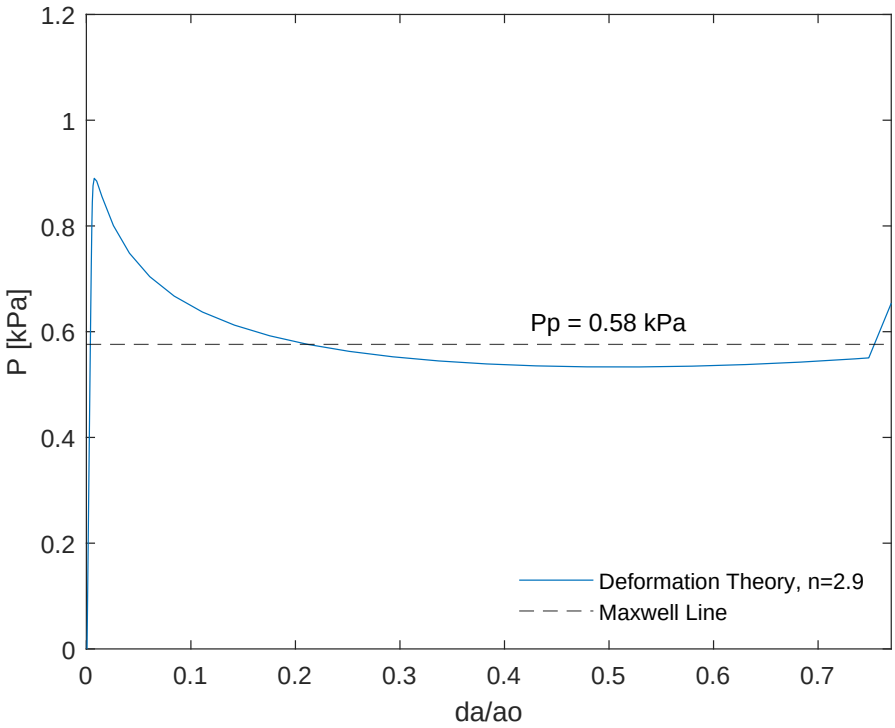

Figure 6.4: Pressure-change of area response for slice with $D/t = 20$, initial ovality 0.2% and material exponent $n = 2.9$.

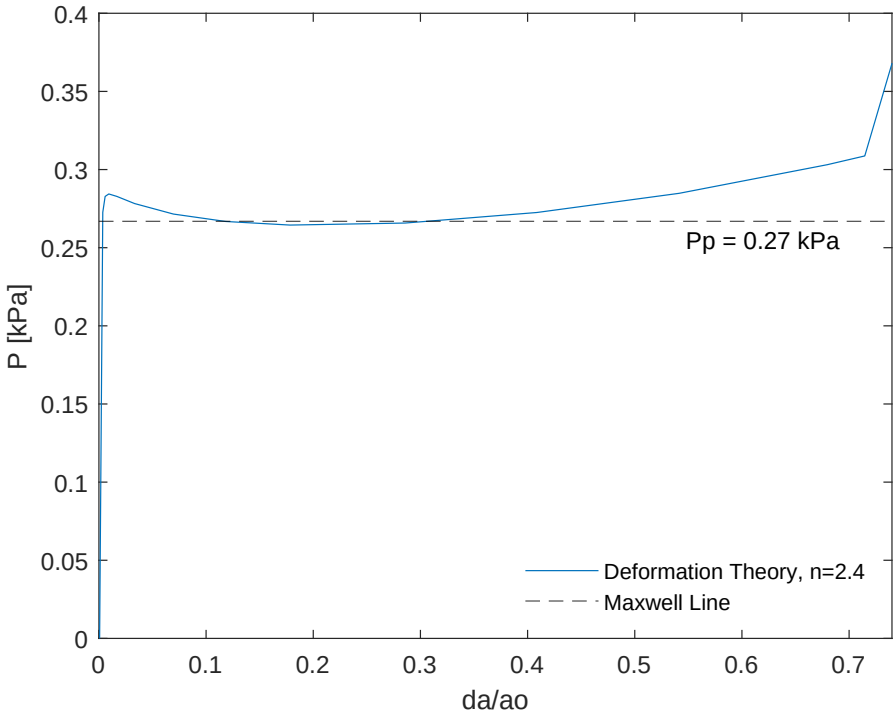

Figure 6.5: Pressure-change of area response for slice with $D/t = 30$, initial ovality 0.2% and material exponent $n = 2.4$.

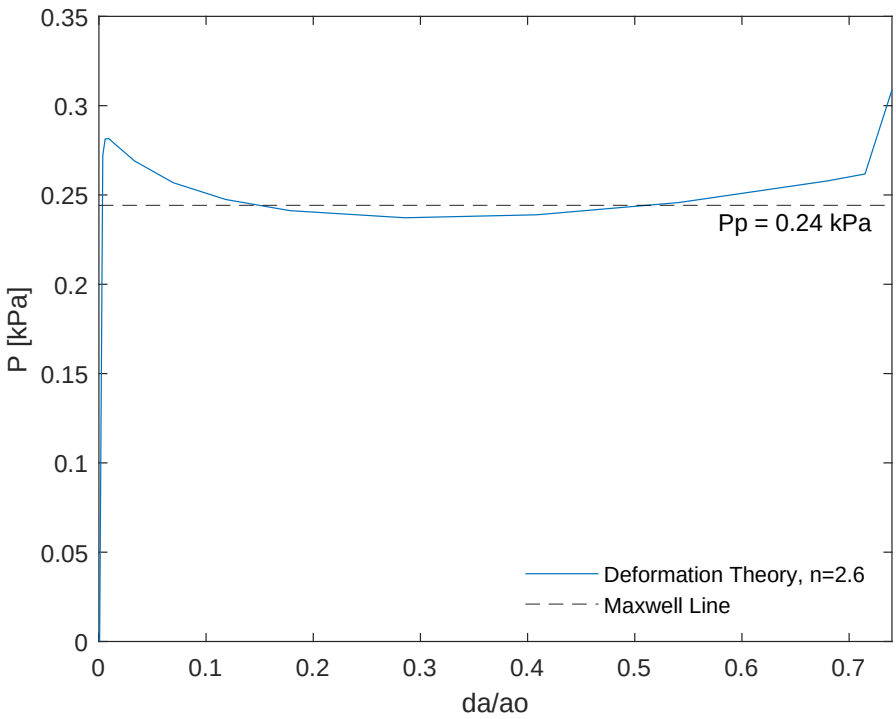

Figure 6.6: Pressure-change of area response for slice with $D/t = 30$, initial ovality 0.2% and material exponent $n = 2.6$.

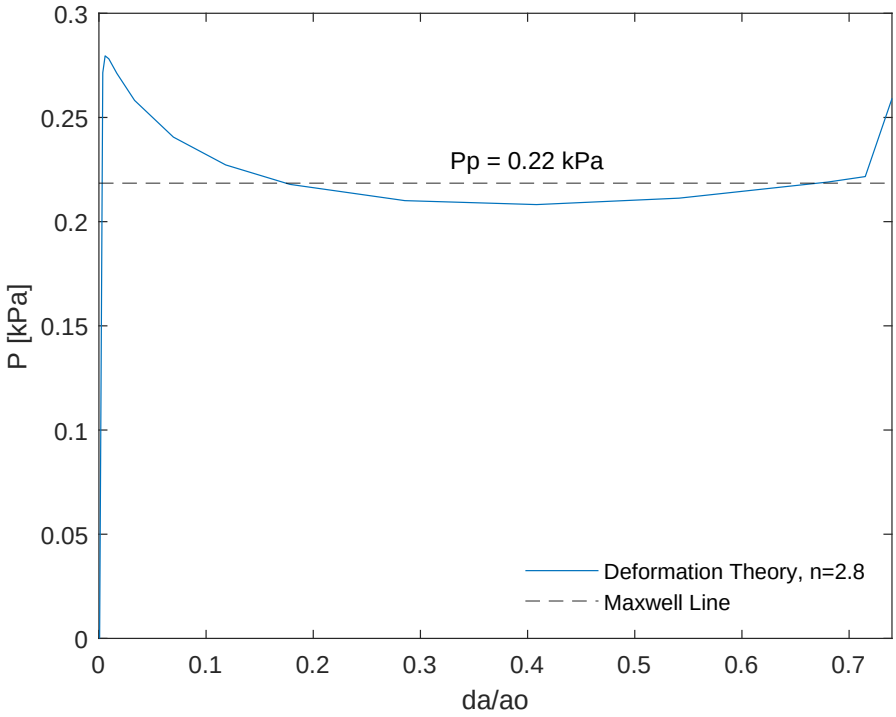

Figure 6.7: Pressure-change of area response for slice with $D/t = 30$, initial ovality 0.2% and material exponent $n = 2.8$.

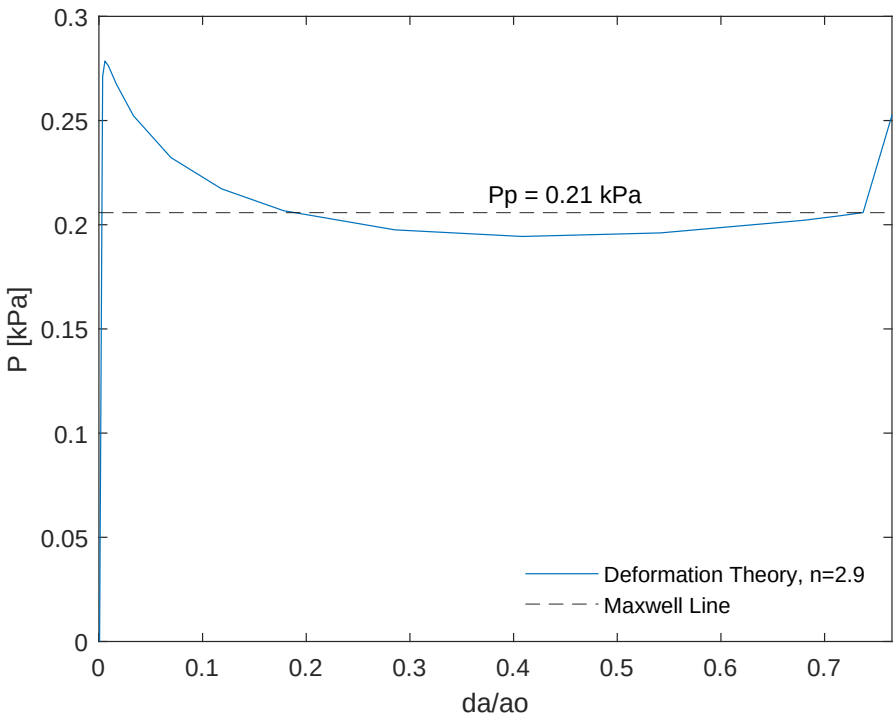

Figure 6.8: Pressure-change of area response for slice with $D/t = 30$, initial ovality 0.2% and material exponent $n = 2.9$.

The estimations of propagation pressure (Pp) for the base case 3D slice models, using a constant mesh ($h = 25$, $t = 5$, $l = 1$) and element type C3D20R, across different material exponents are summarized in Table 6.1. Responses for each case of D/t with different material exponents, presented above, have been merged in Figures 6.9, 6.10 and 6.11 for cases $D/t = 12$, $D/t = 20$ and $D/t = 30$ respectively.

Table 6.1: Propagation Pressure Values (Pp) for Different D/t Ratios and Material Exponent values.

Pp (kPa)	$n = 2.4$	$n = 2.6$	$n = 2.8$	$n = 2.9$
D/t=12	3.23	2.70	2.27	2.09
D/t=20	0.82	0.72	0.62	0.58
D/t=30	0.27	0.24	0.22	0.21

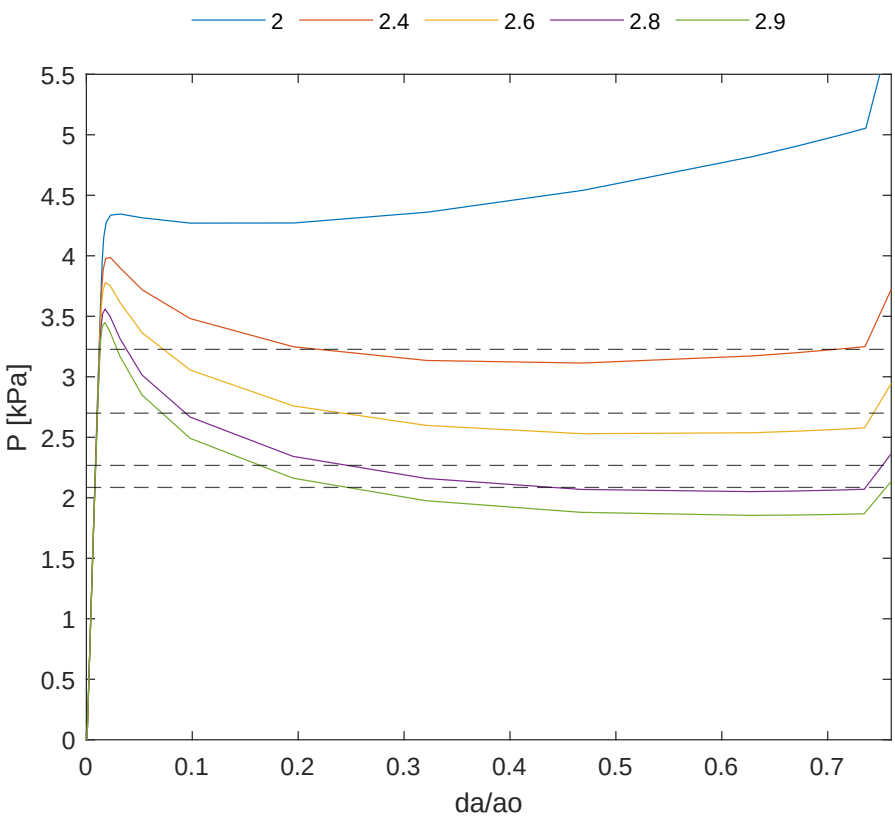

Figure 6.9: Pressure-change of area responses for slice models with $D/t = 12$ and initial ovality 0.2% varying in material exponent values $2.4, 2.6, 2.8$ and 2.9.

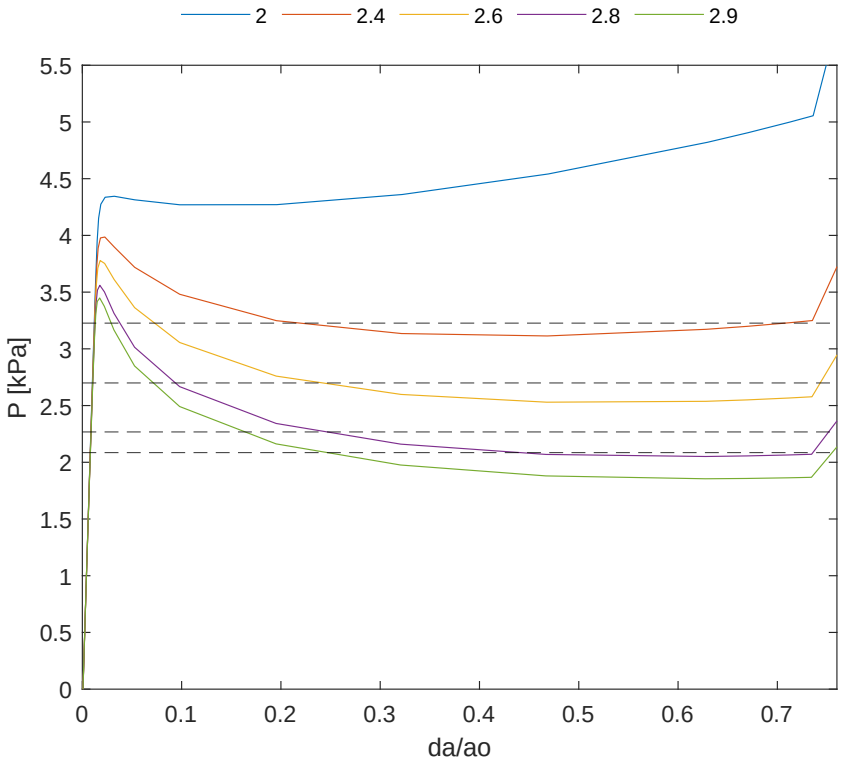

Figure 6.10: Pressure-change of area responses for slice models with $D/t = 20$ and initial ovality 0.2% varying in material exponent values $2.4, 2.6, 2.8$ and 2.9.

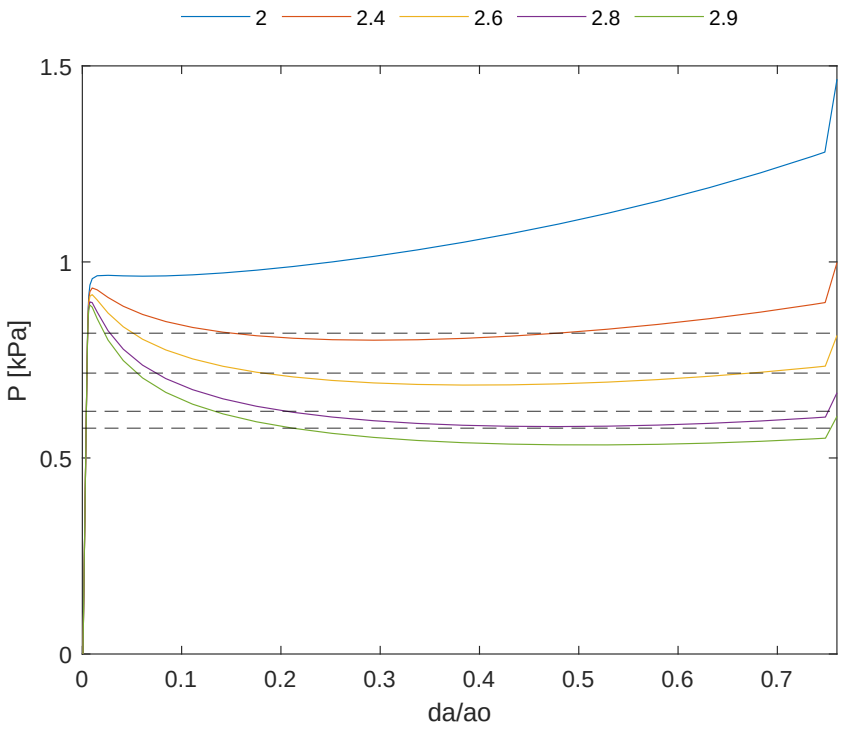

Figure 6.11: Pressure-change of area responses for slice models with $D/t = 30$ and initial ovality 0.2% varying in material exponent values $2.4, 2.6, 2.8$ and 2.9.

6.1.2 Mises Stresses and Logarithmic Strains

From the analyses of the base case three-dimensional slice models Mises Stress and logarithmic strain have also been exported for the condition of contact when the collapse occurs. The findings of these peak values are revealed in the Table 6.2 that follows.

Table 6.2: Comparison of Mises Stress and Logarithmic Strain for Different D/t Ratios and Material Exponents for the condition of collapse in 3D slice models.

Exponent (n)	D/t=12		D/t=20		D/t=30	
	Mises [kPa]	log strain [%]	Mises [kPa]	log strain [%]	Mises [kPa]	log strain [%]
2	652	26.4	407	14.7	293	10.1
2.4	361 ↓	32.5 ↑	259 ↓	17.1 ↑	216 ↓	12.5 ↑
2.6	276 ↓	36.1 ↑	206 ↓	19.3 ↑	177 ↓	13.9 ↑
2.8	216 ↓	39.5 ↑	167 ↓	21.6 ↑	146 ↓	15.6 ↑
2.9	193 ↓	41.4 ↑	143 ↓	19.9 ↓	128 ↓	14.9 ↓

6.2 Three-dimensional long tubes results

In this section, the Pressure-Change of area responses from the base case three-dimensional long tube models, as discussed in Section 3.2.3, will be presented. Additionally, estimations for the propagation pressure of each case will be provided.

6.2.1 Estimation for propagation pressure of 3D long tube base case models

For the approximation of propagation pressure in three-dimensional long tube models the theory presented in section 2.2 was utilized. Particularly, in Figure 2.1 it can be observed that pressure reaches a constant value in stage III which determines propagation pressure. Figures 6.12 - 6.26 present the responses for $D/t = 12$, $D/t = 20$, and $D/t = 30$ across a range of material exponent values $2.4, 2.6, 2.8$, and 2.9. The configuration stages from the three-dimensional collapse (Stage I) until the propagation reaches the end where boundary conditions are applied (Stage V) are extracted from the ODB file which resulted from ABAQUS analysis. These stages, for the cases with $D/t = 20, n = 2.6$ and $D/t = 30, n = 2$ are illustrated in Figures 6.27 and 6.28 respectively.

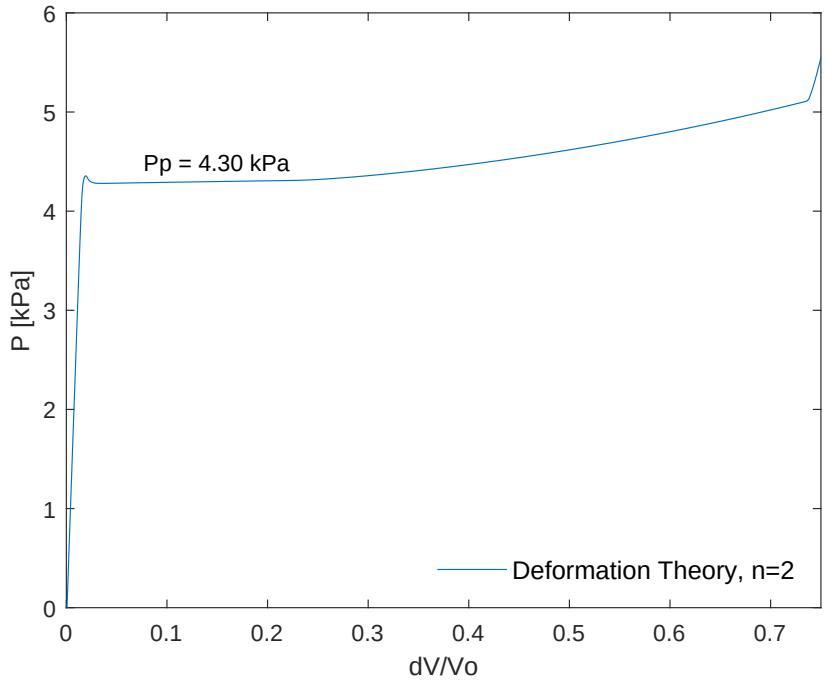

Figure 6.12: Pressure-change of volume response for tube with $D/t = 12$, initial ovality 0.2% and material exponent $n = 2$.

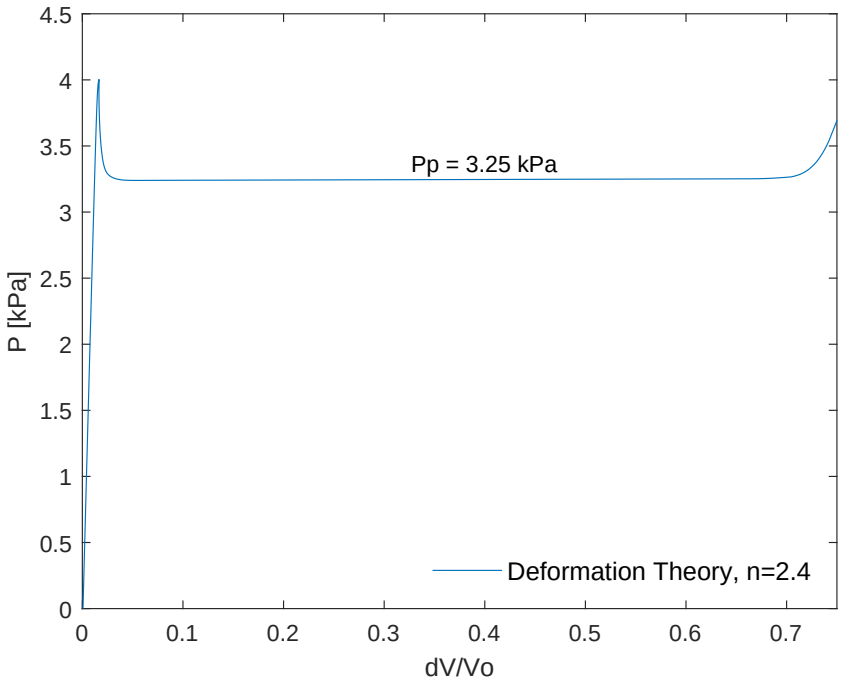

Figure 6.13: Pressure-change of volume response for tube with $D/t = 12$, initial ovality 0.2% and material exponent $n = 2.4$.

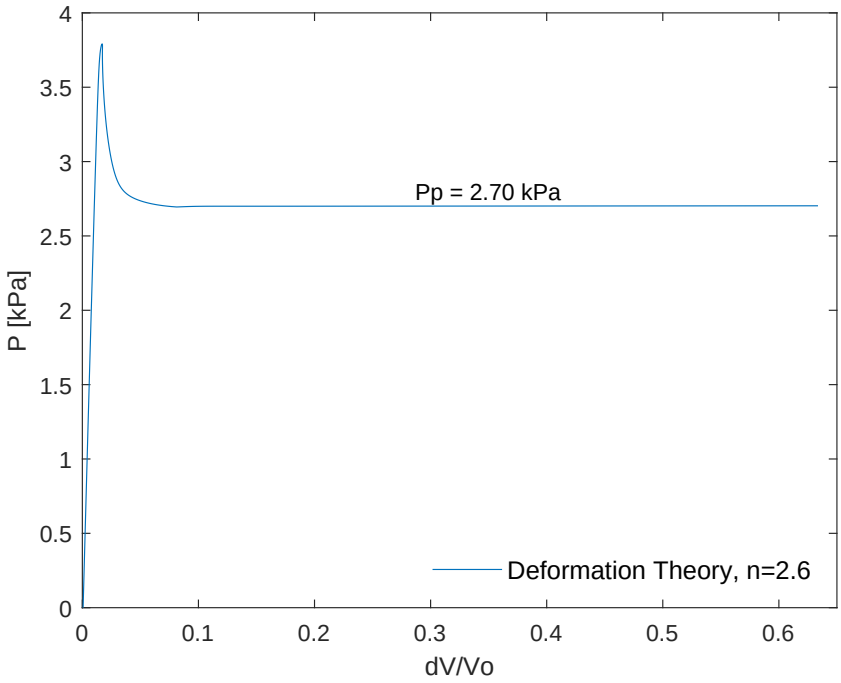

Figure 6.14: Pressure-change of volume response for tube with $D/t = 12$, initial ovality 0.2% and material exponent $n = 2.6$.

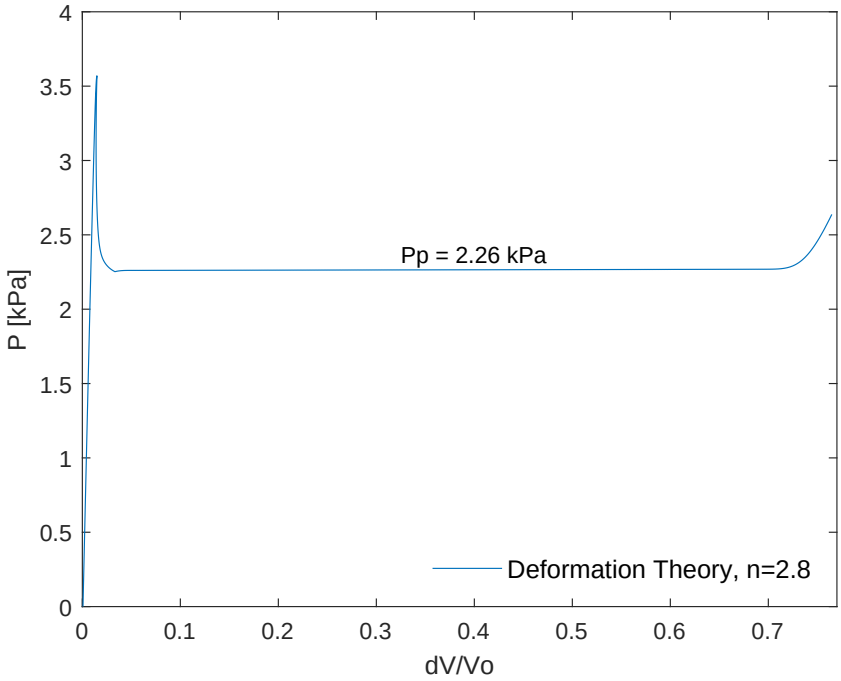

Figure 6.15: Pressure-change of volume response for tube with $D/t = 12$, initial ovality 0.2% and material exponent $n = 2.8$.

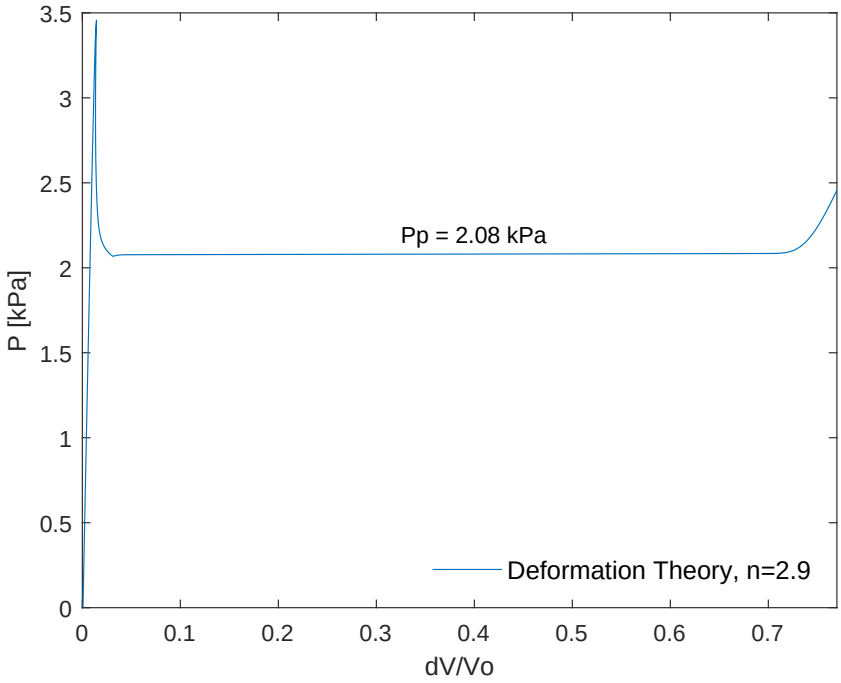

Figure 6.16: Pressure-change of volume response for tube with $D/t = 12$, initial ovality 0.2% and material exponent $n = 2.9$.

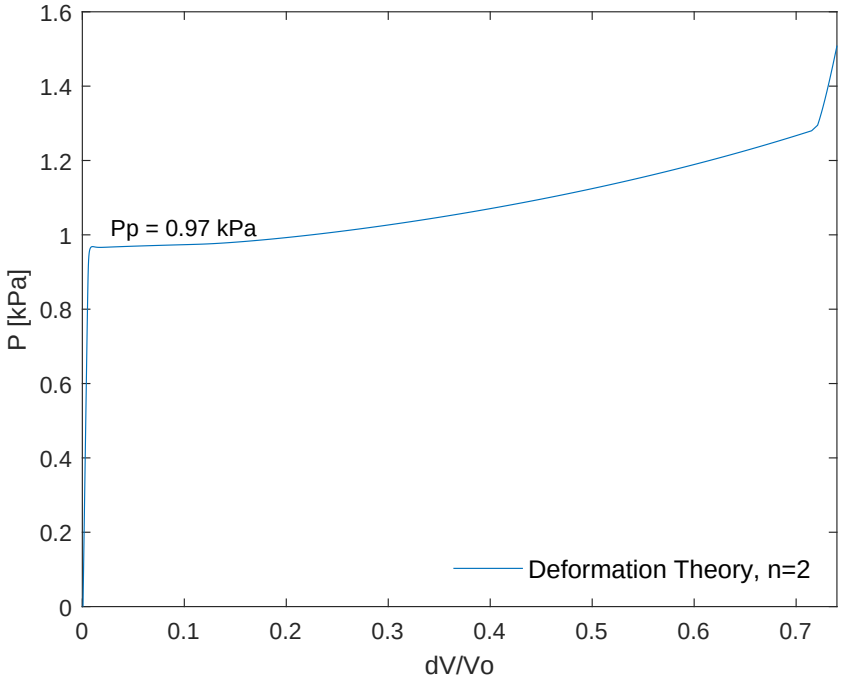

Figure 6.17: Pressure-change of volume response for tube with $D/t = 20$, initial ovality 0.2% and material exponent $n = 2$.

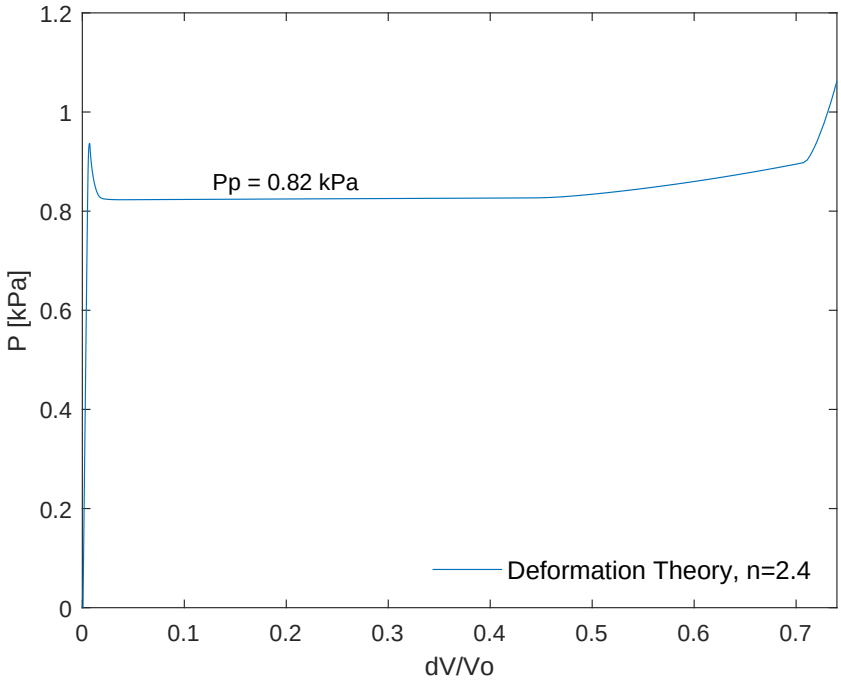

Figure 6.18: Pressure-change of volume response for tube with $D/t = 20$, initial ovality 0.2% and material exponent $n = 2.4$.

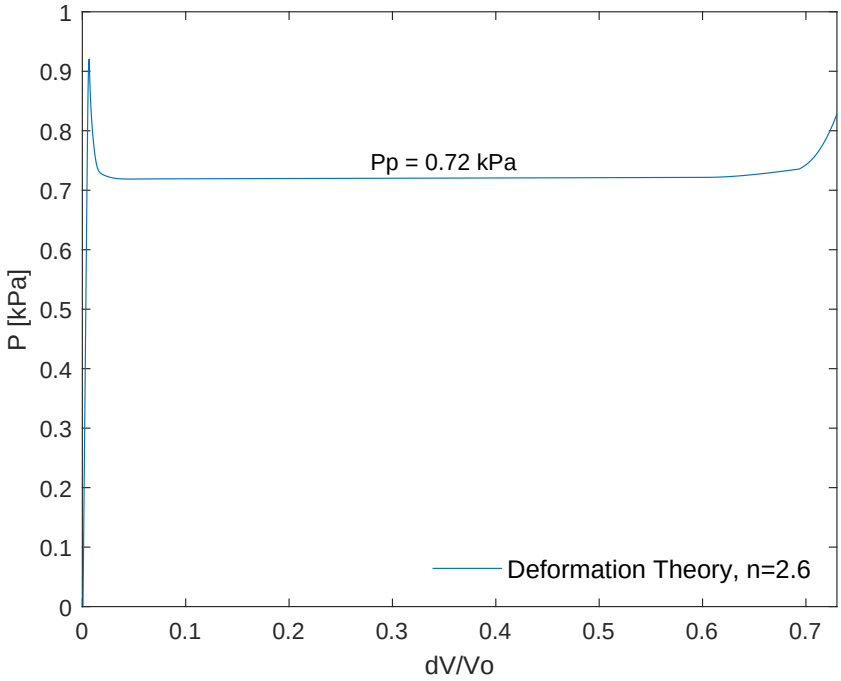

Figure 6.19: Pressure-change of volume response for tube with $D/t = 20$, initial ovality 0.2% and material exponent $n = 2.6$.

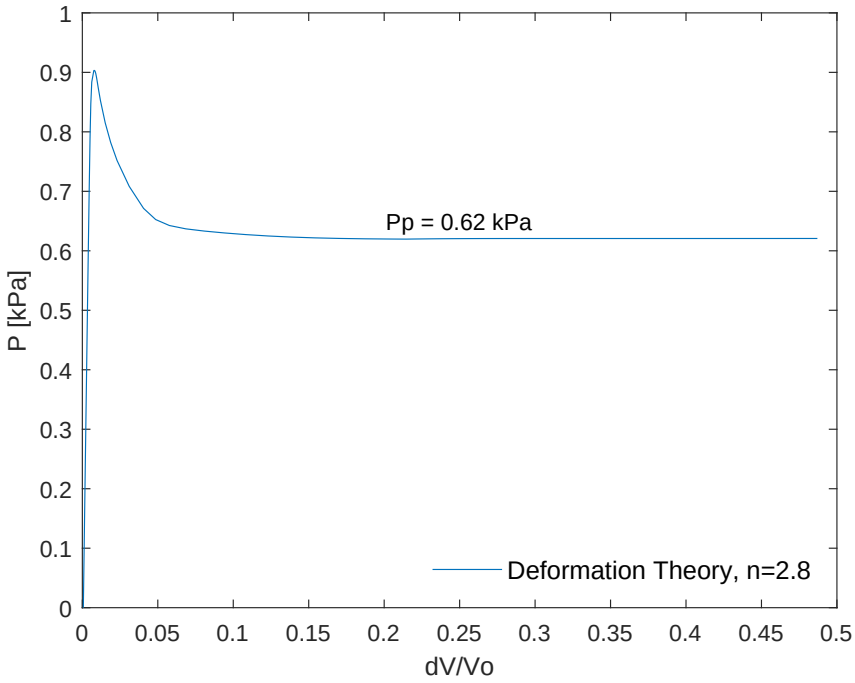

Figure 6.20: Pressure-change of volume response fortube with $D/t = 20$, initial ovality 0.2% and material exponent $n = 2.8$.

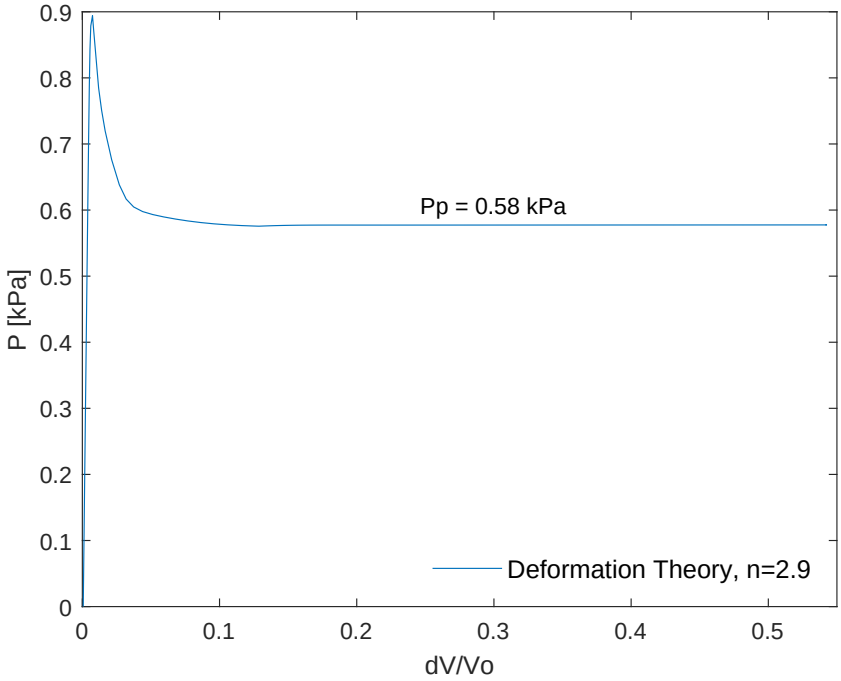

Figure 6.21: Pressure-change of volume response for tube with $D/t = 20$, initial ovality 0.2% and material exponent $n = 2.9$.

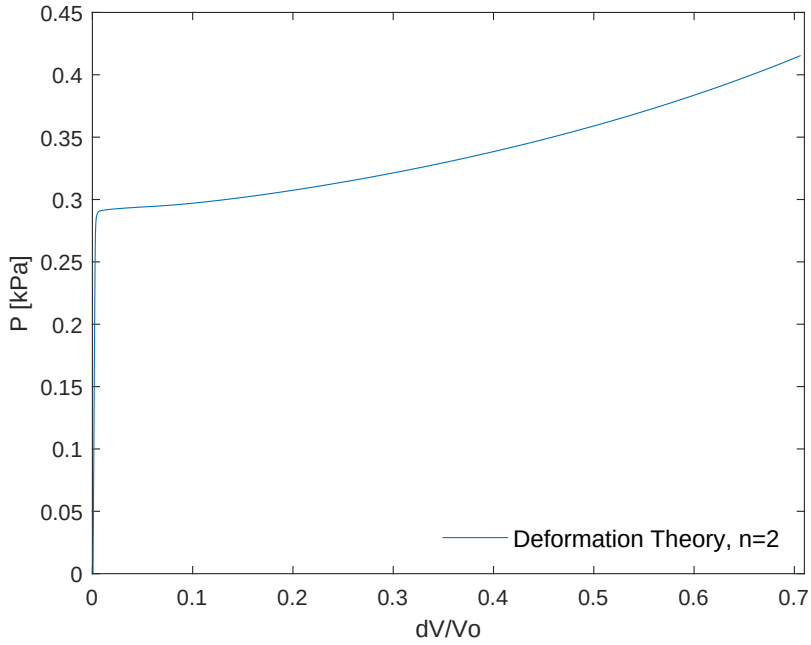

Figure 6.22: Pressure-change of volume response for tube with $D/t = 30$, initial ovality 0.2% and material exponent $n = 2$.

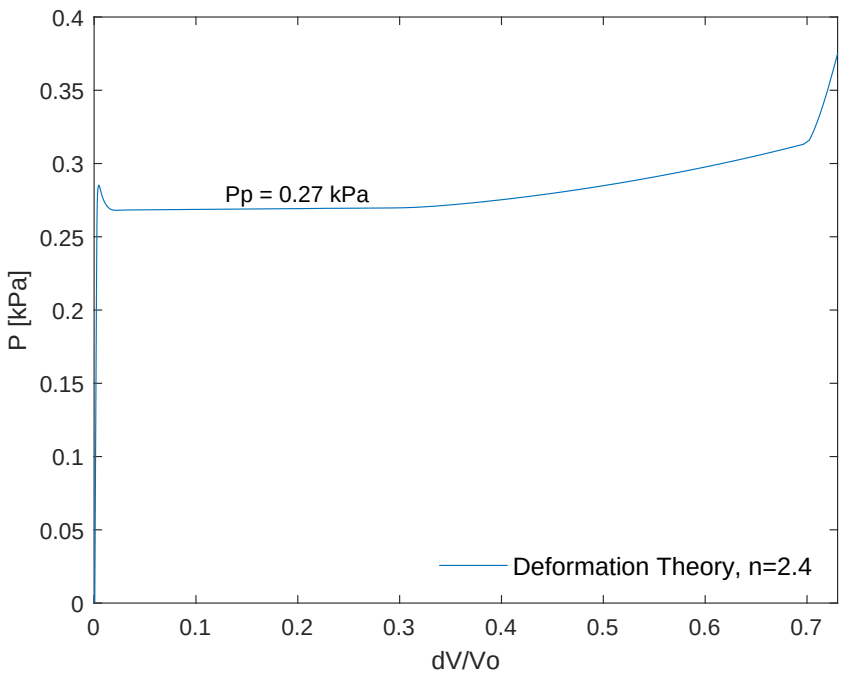

Figure 6.23: Pressure-change of volume response for tube with $D/t = 30$, initial ovality 0.2% and material exponent $n = 2.4$.

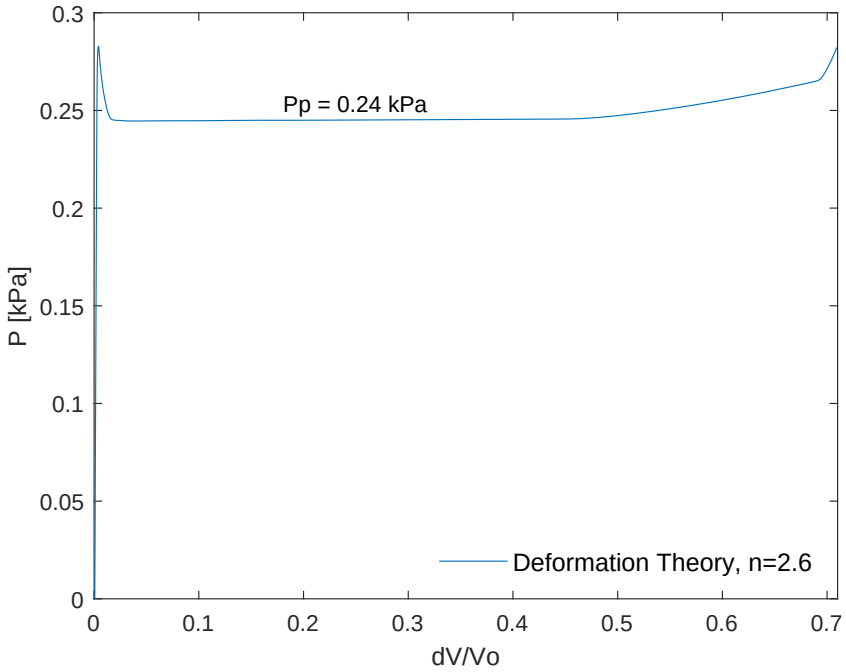

Figure 6.24: Pressure-change of volume response for tube with $D/t = 30$, initial ovality 0.2% and material exponent $n = 2.6$.

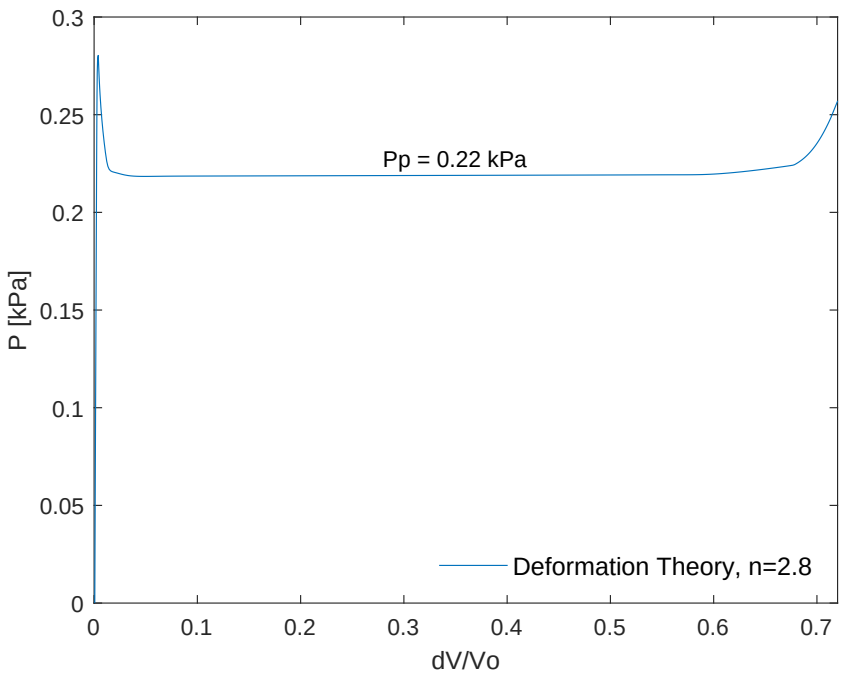

Figure 6.25: Pressure-change of volume response for tube with $D/t = 30$, initial ovality 0.2% and material exponent $n = 2.8$.

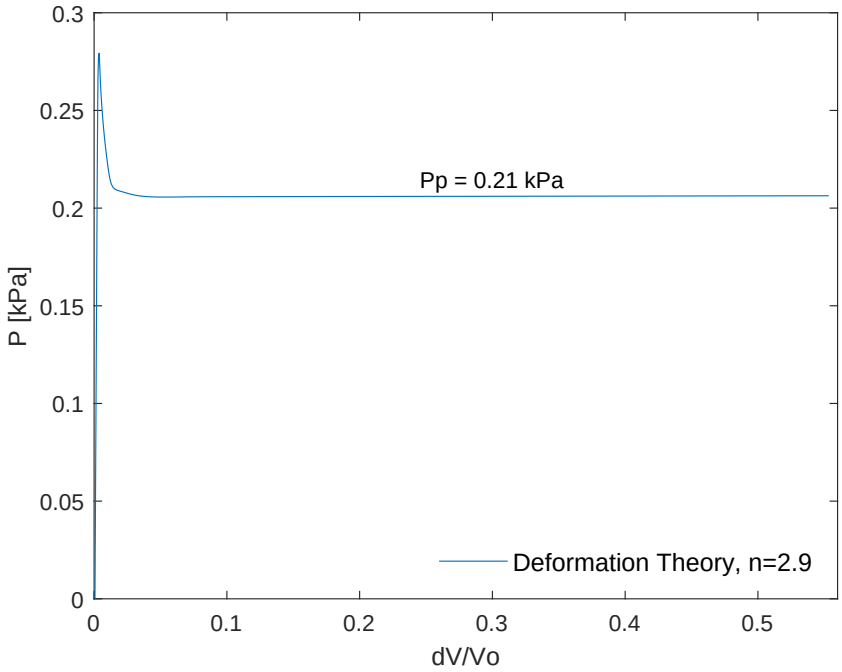

Figure 6.26: Pressure-change of volume response for tube with $D/t = 30$, initial ovality 0.2% and material exponent $n = 2.9$.

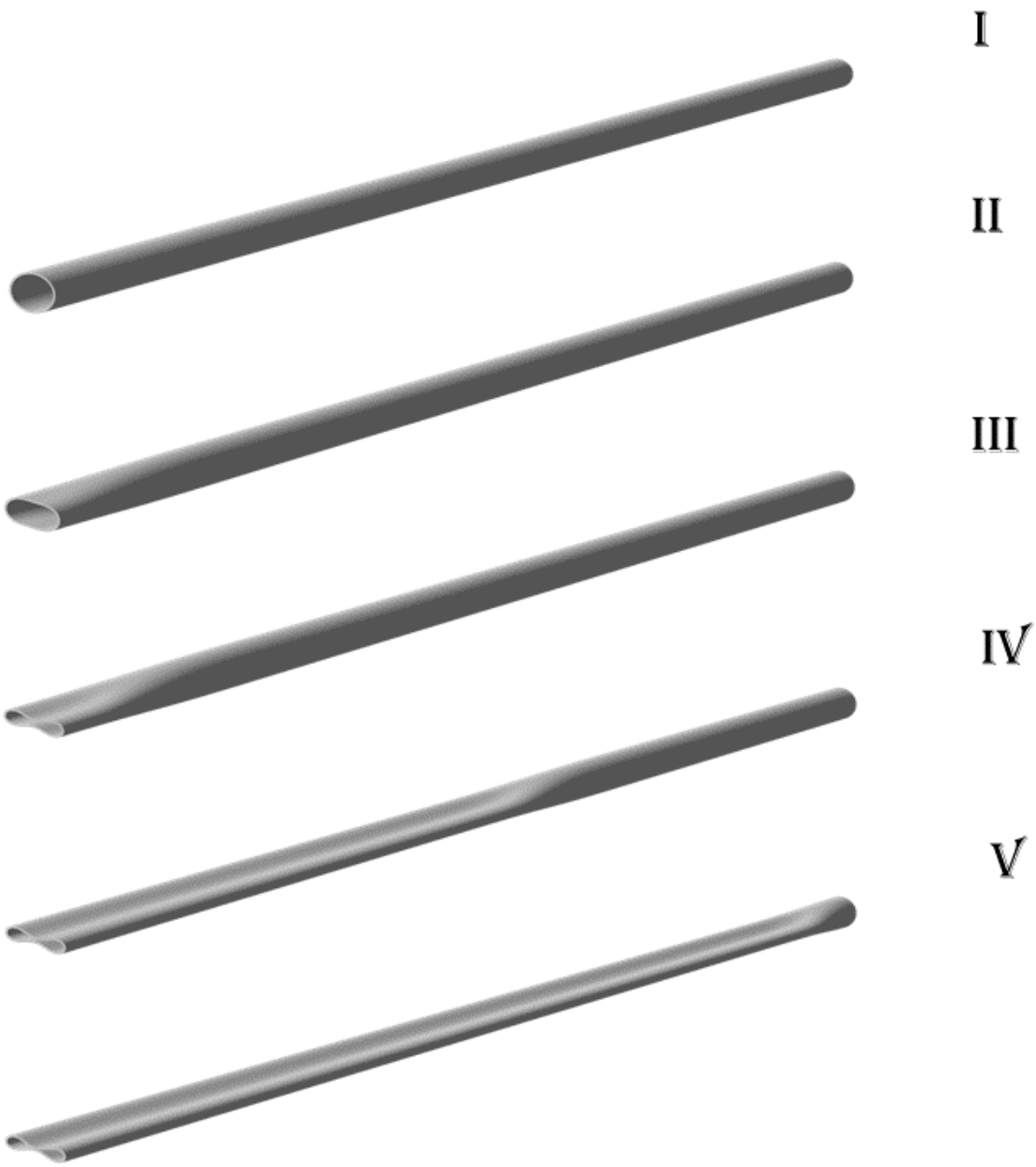

Figure 6.27: The numerical simulations of the sequence of buckle propagation phenomenon for the corresponding (1)-(5) stages of pressure-change in volume response ($D/t = 20, n = 2.6$).

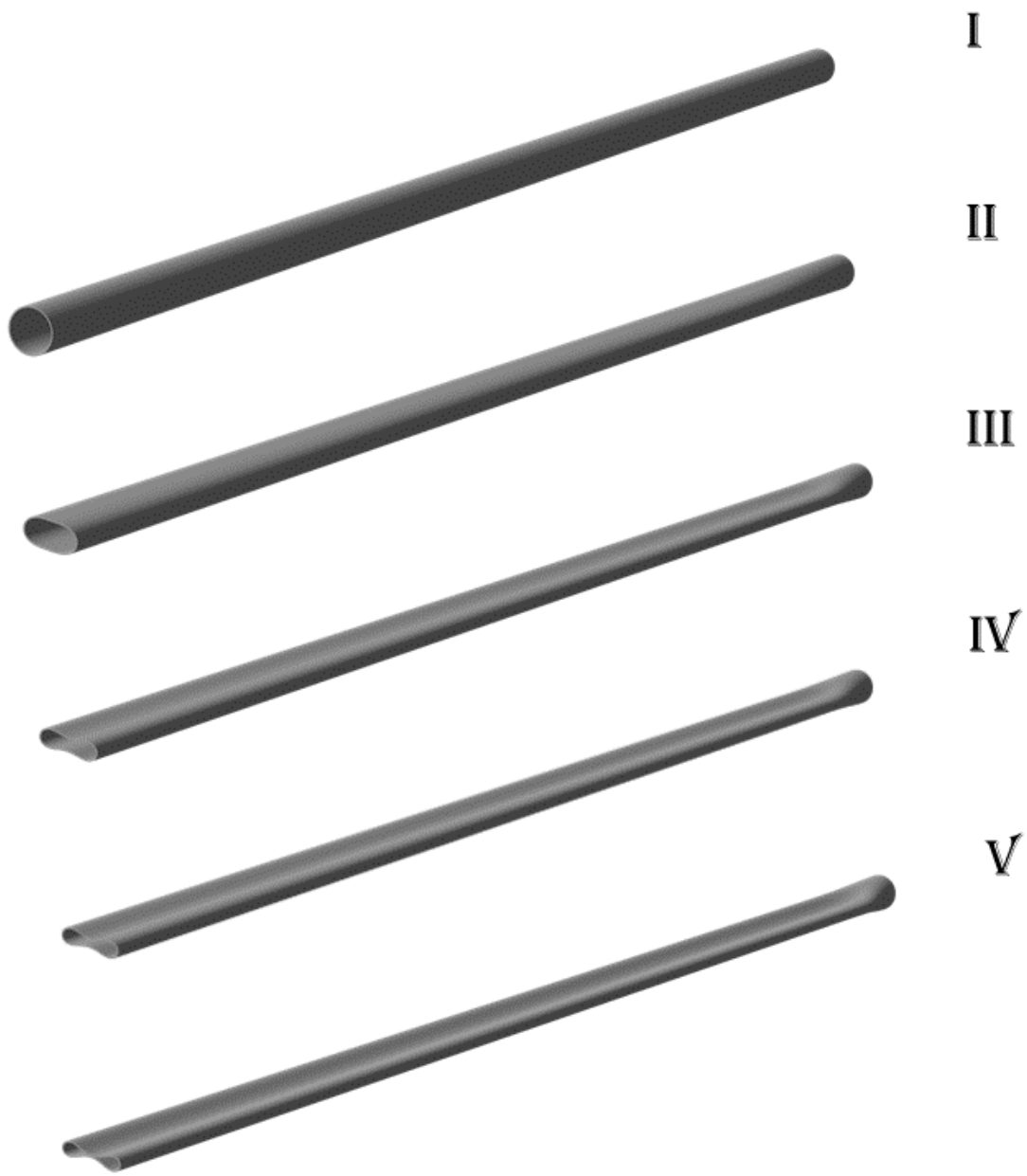

Figure 6.28: The numerical simulations of the sequence of buckle propagation phenomenon for the corresponding (1)-(5) stages of pressure-change in volume response ($D/t = 30, n = 2$).

The estimations of propagation pressure (Pp) for the base case 3D long tube models, using a constant mesh ($h = 25, t = 5, l = 250$) and element type C3D20R, across different material exponents are summarized in Table 6.3. Responses for each case of D/t with different material exponents, presented above, have been merged in Figures 6.29, 6.30 and 6.31 for cases $D/t = 12$, $D/t = 20$ and $D/t = 30$ respectively.

Table 6.3: Propagation Pressure Values (Pp) for Different D/t Ratios and n Exponents.

Pp (kPa)	$n = 2$	$n = 2.4$	$n = 2.6$	$n = 2.8$	$n = 2.9$
D/t=12	4.30	3.25	2.70	2.26	2.08
D/t=20	0.97	0.82	0.72	0.62	0.58
D/t=30	-	0.27	0.24	0.22	0.21

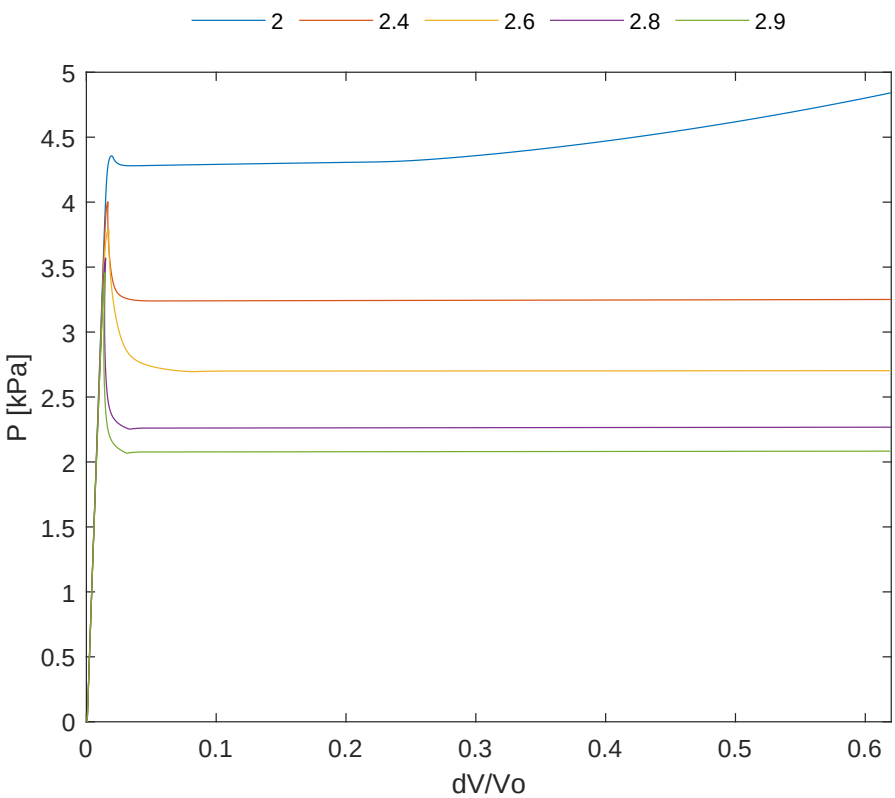

Figure 6.29: Pressure-change of volume responses for 3D long tube models with $D/t = 12$ and initial ovality 0.2% varying in material exponent values $2.4, 2.6, 2.8$ and 2.9.

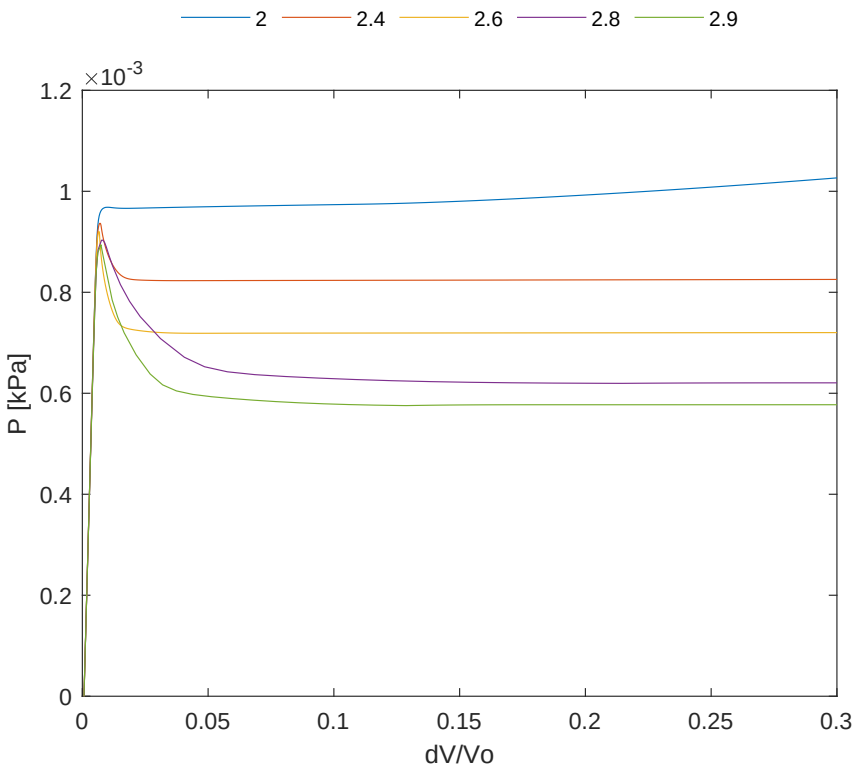

Figure 6.30: Pressure-change of volume responses for 3D long tube models with $D/t = 20$ and initial ovality 0.2% varying in material exponent values $2.4, 2.6, 2.8$ and 2.9.

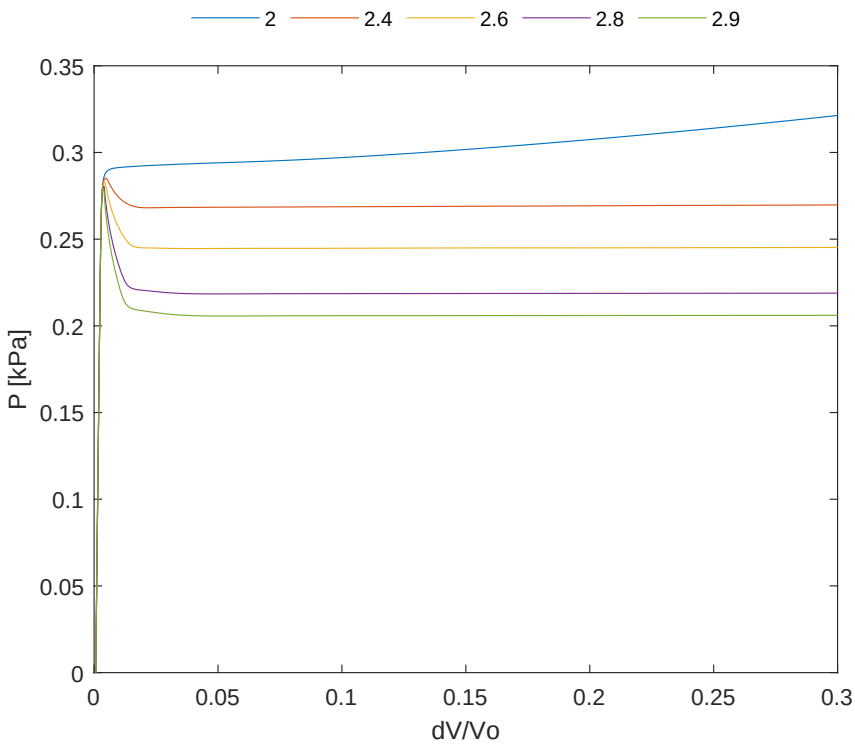

Figure 6.31: Pressure-change of volume responses for 3D long tube models with $D/t = 30$ and initial ovality 0.2% varying in material exponent values $2.4, 2.6, 2.8$ and 2.9.

6.2.2 Comparison results of C3D20R and SC8R Element types

Chapter 3 of the thesis involved an examination of the element type utilized for the base case models. The investigation revealed that the element types C3D20R and SC8R are the most appropriate for the base case models in this thesis with C3D20R type the final option. In order to facilitate comparison, a model with a diameter-to-thickness ratio of 12, similar to the base case model, but employing the SC8R element type was created. This model was then evaluated for material exponents of $2.4, 2.6, 2.8$ and 2.9. The results of the analysis are exhibited in the following Figures. Consequently, the estimations of propagation pressure and contact conditions of propagation, along with the corresponding results that came up from the analysis of the base case model (Section 6.2.1), are summarized in the Table 6.4.

Table 6.4: Comparison of Contact Conditions and Propagation Pressure (Pp) for Different D/t Ratios and Element Types

D/t=12	**C3D20R**		**SC8R**	
	Contact	**Pp [Pa]**	**Contact**	**Pp [Pa]**
n=2.4	No	3245.98	No	2898.64
n=2.6	Yes	2701.07	Yes	2440.43
n=2.8	Yes	2262.00	Yes	2059.94
n=2.9	Yes	2080.56	Yes	1898.36

Table 6.5: Contact Conditions for Different D/t Ratios and Material Exponents

Contact	**D/t=12**	**D/t=20**	**D/t=30**
n=2	No	No	No
n=2.4	No	No	No
n=2.6	Yes	No	No
n=2.8	Yes	Yes	No
n=2.9	Yes	Yes	Yes

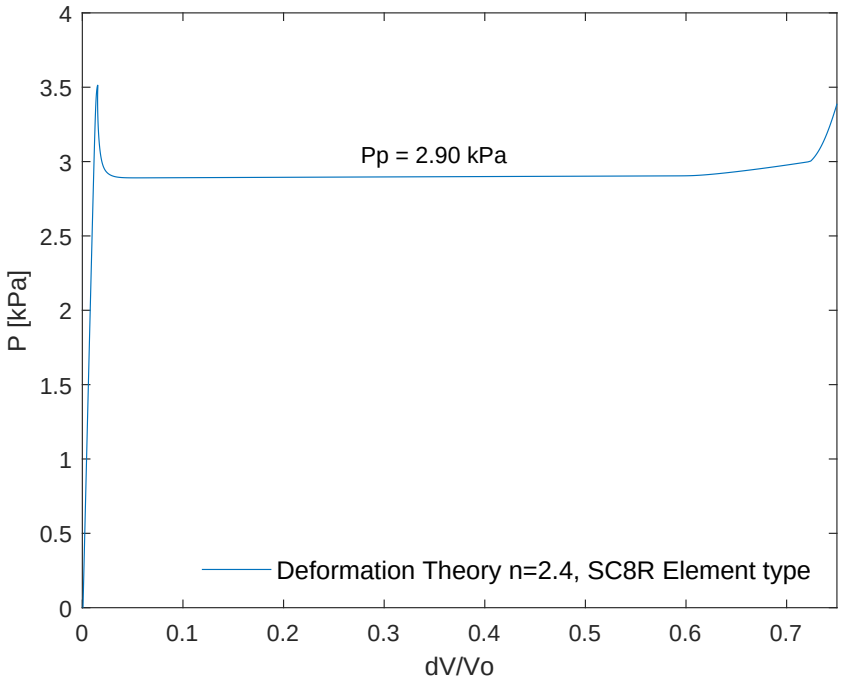

Figure 6.32: Pressure-change of volume response for the tube with $D/t = 12$, initial ovality 0.2%, SC8R elements and material exponent $n = 2.4$.

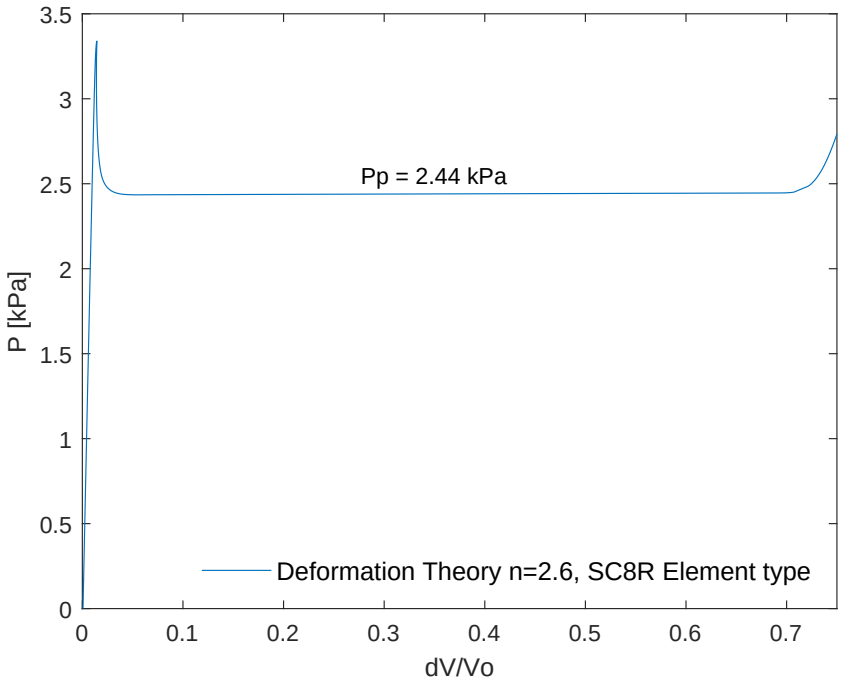

Figure 6.33: Pressure-change of volume response for the tube with $D/t = 12$, initial ovality 0.2%, SC8R elements and material exponent $n = 2.6$.

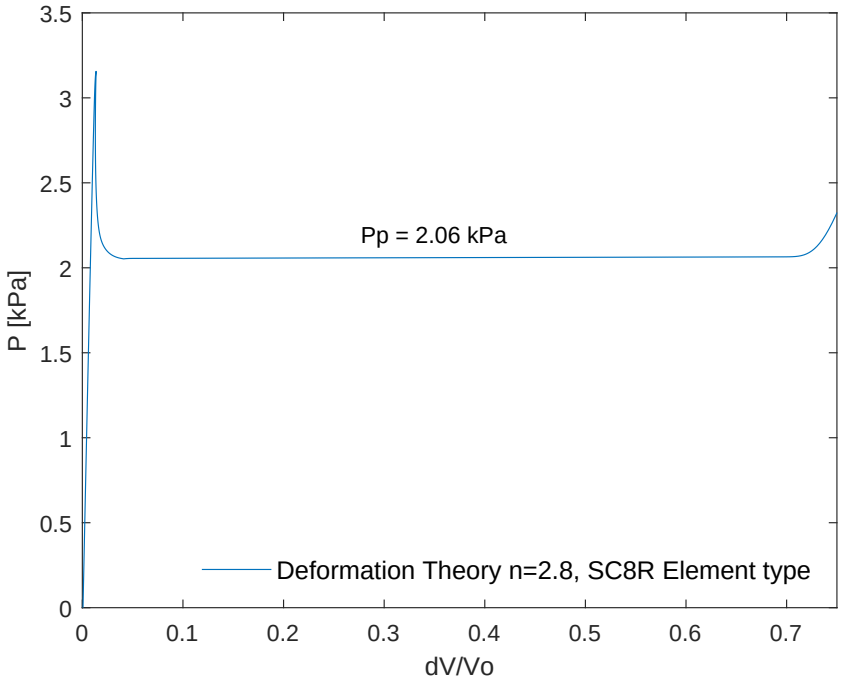

Figure 6.34: Pressure-change of volume response for the tube with $D/t = 12$, initial ovality 0.2%, SC8R elements and material exponent $n = 2.8$.

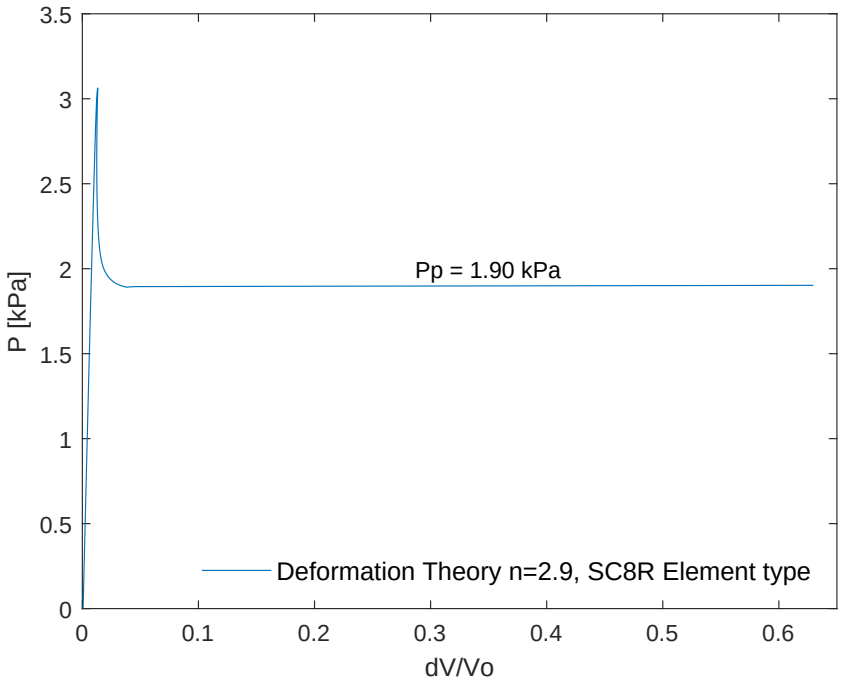

Figure 6.35: Pressure-change of volume response for the tube with $D/t = 12$, initial ovality 0.2%, SC8R elements and material exponent $n = 2.9$.

6.2.3 Contact conditions

For the three-dimensional long tube base case models an investigation on the contact conditions of propagation has been performed. In particular, in some of the long tubes studied, collapse and propagation were observed to occur without contact. The results are displayed in Table 6.5.

6.3 Summarized results for 3D slice and long tube models

For comparison causes between the three-dimensional slice models and three-dimensional long tube models Tables 6.6, 6.7 and 6.8, for D/t equal to $12, 20$ and 30 respectively, were constructed. The Tables presented in this section provide a summary of the estimated propagation pressure, in Pa units, and contact conditions for each case, excluding the case with a material exponent of 2. The reason for excluding this specific case will be discussed in Chapter 7. Also in the following Tables a ”diff” value is being calculated which determines a percentage of the difference between the estimated propagation pressure of 3D slice and long tube models and its calculated from the equation:

$$\text{Diff}(\%) = \left| \frac{P_p^{(\text{3D})} - P_p^{(\text{slice})}}{P_p^{(\text{slice})}} \right| \times 100$$

Table 6.6: Comparison of 3D slices and long tubes propagation pressure values (Pp) for $D/t = 12$ across a range of material exponent values.

D/t=12

Pp (Pa)	**n=2.4**	**n=2.6**	**n=2.8**	**n=2.9**
slice	3226.57	2699.34	2267.54	2085.48
3D	3245.98	2701.07	2262.00	2080.56
Diff %	0.60	0.06 ↓	0.24 ↑	0.24
Contact	No	Yes	Yes	Yes

Table 6.7: Comparison of 3D slices and long tubes propagation pressure values (Pp) for $D/t = 20$ across a range of material exponent values.

D/t=20

Pp (Pa)	n=2.4	n=2.6	n=2.8	n=2.9
slice	818.20	716.42	619.00	575.95
3D	824.85	720.29	620.65	577.34
Diff %	0.81	0.54 ↓	0.27 ↓	0.24 ↓
Contact	No	No	Yes	Yes

Table 6.8: Comparison of 3D slices and long tubes propagation pressure Values (Pp) for different $D/t = 30$ ratio across a range of material exponent values.

D/t=30

Pp (Pa)	n=2.4	n=2.6	n=2.8	n=2.9
slice	266.88	244.16	218.46	205.82
3D	269.09	245.00	218.81	206.09
Diff %	0.83	0.34 ↓	0.16 ↓	0.13 ↓
Contact	No	No	No	Yes

Chapter 7

Conclusions and Discussion

The focus of this thesis revolves around the investigation of collapse and buckle propagation phenomena in collapsible tubes for biomedical applications. The numerical framework of ABAQUS was employed to analyze two-dimensional elastic models and three-dimensional slice and long tube models as base cases, aiming to understand their behavior under external pressure. MATLAB was used for data processing and analysis. In this section, the conclusions derived from this study will be exhibited. Starting with the conclusions for two-dimensional elastic models, and subsequently with the conclusions from the analysis of three-dimensional slice models and three-dimensional long tube models. Finally, a comparison between the 3D slice and long tube models will be presented.

7.1 Conclusions for 2D models

In Chapter 5 are presented the responses derived from the analysis of the two-dimensional elastic models. Figures 5.1, 5.2 and 5.3 illustrate the impact of initial ovality on the pre-buckling and post-buckling behaviors of cases with $D/t = 10$, $D/t = 20$, and $D/t = 40$ respectively, when various initial ovalities are applied. The plots also feature the analytical post-buckling curve 2.3 for the ideal ring case. The conclusion that can be exported from these figures is that, as the initial imperfection value increases, the deviation of the collapse pressure from curve of the ideal case also increases leading to the softening of the ring and collapsing at lower pressures.

7.2 Conclusions for 3D slice models

In Chapter 3 an analytical study on three-dimensional slice models is presented. The study involved the construction of three slice models with different diameter-to-thickness

ratios $(12, 20, 30)$, and these models were subjected to analysis using various material exponents $(2, 2.4, 2.6, 2.8, 2.9)$. Moving forward, section 6.1 presents the results obtained from the analysis of these models. The responses for all cases were monitored until the tube walls made contact. The analysis led to the estimation of the propagation pressure for every case of material exponent, except $n = 2$, and D/t, which is summarized in Table 6.1. From these results it can be obtained that for the same diameter-to-thickness ratio the propagation pressure decreases as the material exponent increases from 2.4 to 2.9. This can also be derived from the Figures 6.9, 6.10 and 6.11 which shows the P-da responses for the 5 different cases of material exponents with D/t equal to 12, 20 and 30 respectively. However, in Section 4.1, it was noted that as the material exponent decreases, the tangent modulus increases, resulting in the stress-strain response approaching the linear elastic curve and exhibiting similar behavior. So, for the case with material exponent $n = 2$, there is no pressure maximum observed because the post-buckling behavior of its response is very high making the application of the Maxwell line method infeasible, and thus the estimation of the propagation pressure impossible in three-dimensional slice models. Furthermore, for the rest material exponents, it can be observed that as the diameter-to-thickness ratio (D/t) increases, the propagation pressure tends to decrease for the same material exponent.

7.3 Conclusions for 3D long tube models

The study of three-dimensional long tube models was presented analytically in Chapter 3 where for the three cases of diameter-to-thickness ratios $(12, 20, 30)$, five different material exponents were applied $(2, 2.4, 2.6, 2.8, 2.9)$. The results from these models analyses were exhibited in Chapter 3 and involved estimation for the propagation pressure of each case and contact conditions of propagation.

In the previous section, it was noted that the estimation of propagation pressure for a material exponent of $n = 2$ was not feasible in the analysis of three-dimensional slice models. Although, propagation pressure can be derived from the response of three-dimensional long tube models as described in Section 2.2 but only for the cases with $D/t = 12$ and $D/t = 20$. In Figures 6.29, 6.30 and 6.31 the responses of base case models with D/t equal to 12, 20 and 30 and material exponents 2, 2.4, 2.6, 2.8, followed until propagation reaches the end where boundary condition applied, are presented. These figures reveal a similar trend to that of the 3D slice models. Regarding the case with diameter-to-thickness ration equal to 30 and

n=2, Figure 6.22 reveals that the pressure does not exhibit a plateau but instead follows an increasing rate until propagation reaches the end of the tube length. This behavior indicates the presence of uniform collapse rather than the development of propagating buckles. From these findings it is derived that this case can be characterized as limit case. The above conclusions are also supported by the configuration of the model analysis displayed in Figure 6.28, which illustrates that a uniform collapse appears (Stage II) rather than the formation of propagating buckles. In this case, the contact condition during propagation is characterized as contactless which can be observed at ”Stage II” till ”Stage IV”. However, in ”Stage V,” when the propagation reaches the end of the tube length, the boundary conditions start to influence the propagation behavior. As a result, there is a sudden contact between the two walls at this stage (Stage IV). Furthermore, it is noteworthy that for the cases with $D/t = 12$ and $D/t = 20$, the observed contactless plateau is particularly small, with the plateau for $D/t = 20$ being smaller than the one for $D/t = 12$. This significant decrease in the size of the plateau indicates an important finding: as the cross-section of the tube becomes thinner (as indicated by the increase in D/t ratio), the extension of propagation plateau diminishes.

Moreover, in Table 6.3, which summarizes the results for the estimated propagation pressure of each case, it can be observed that for the same diameter-to-thickness ratio, the propagation pressure decreases as the material exponent increases. The same trend can be observed in the analysis of the three-dimensional slice models as noted in previous section. Also, for the same material exponent, the propagation pressure increases as the diameter-to-thickness ratio also increases, which was noted for 3D slice models as well.

Finally, in Table 6.5 contact conditions of propagation for each case are showcased. The conclusion that could be derived is that as the diameter-to-thickness ratio increases, the propagation with contact occurs for bigger value of material exponent. For cases with a material exponent below 2.6, propagation occurs without contact between the tube walls.

7.3.1 Comparison between C3D20R and SC8R Element types

Section 6.2.2 provides a comparison between the C3D20R and SC8R elements for three-dimensional long tubes. The outcomes are presented in Table 6.4, revealing that element type desn’t affect the contact propagation conditions when material exponent remain constant. Additionally, the estimated propagation pressure increases as the material undergoes hardening. Notably, for each material exponent case, the propagation pressure derived from the C3D20R element type is significantly larger than the value obtained from the SC8R element type.

7.4 Comparison between 3D slice and 3D long tube models

In Section 6.3 are summarized some results for the base case thee-dimensional slice and long tube models. Specifically, Tables 6.6, 6.7 and 6.8 the estimations for the propagation pressure, in Pa units, and contact conditions of propagation are presented for diameter-to-thickness ratio 12, 20 and 30 respectively. For the case of D/t equal to 12 it is observed from the "diff" values, varying from 0.06 to 0.6, that the the approximate propagation pressure for the 3D slice and long tube models are particularly close. The percentage difference decreases for n=2.6 and then increases at $n = 2.8$, but it stabilizes at 0.24% for $n = 2.9$. An unexpected finding is that, for material exponents $n = 2.8$ and $n = 2.9$, the propagation pressure values obtained from the long tube models are slightly higher than those obtained from the slice models. However, for the other two cases ($n = 2.4, n = 2.6$), the propagation pressure of the long tube models is somewhat greater than that of the slice models as expected. In the remaining two Tables 6.7 and 6.8 where the conclusions align, the outcomes are as anticipated. Specifically, the numeric measurements of propagation pressure in both the 3D long tube and slice models are quite similar, with slightly higher values observed in the long tube models. Moreover, as the material exponent increases, the percentage difference between the two propagation pressure values decreases.

Chapter 8

Future Work

This thesis examined the response of collpasible tubes, with different diameter-to-thickness ratios, subjected to uniform external pressure when applying a non-linear elastic material model, the Deformation Theory. Specifically, the focus of the investigation was on the behavior of material hardening and its impact on the estimation of propagation pressure for different D/t. To achieve this, three-dimensional slice and long tube models were constructed. The collapsible models aimed to simulate the collapsible tubes that can be found in living organisms.

However, in the analysis of this thesis there wasn't any consideration of fluid flow inside the tube models which could simulate the blood flow in veins or the air in airway (Figure 8.1). Thus, in a future work there could be flow considered inside the tubes in order to investigate its behavior, like the study conducted by M. E. Rosar and Charles S. Peskin [51]. Additionally, an experimental analysis could be conducted like Katz et al. did [52], where experimental data were utilized to establish the functional relationship between cross-sectional area and transmural pressure, as well as the correlation between the energy loss coefficient and cross-sectional area. Another experimental study that could inspire future work is the one conducted by Kozlovsky et al. [1] who developed an experimental method to validate the computational results (Figure 8.1). Moreover, investigation in the structure of the tube as well as pressure and flow measurements during static loading and during steady-state fluid flow could take place, like the experimental study made by Elad et al. [53] who utilized a remote setup suitable for measurements of objects embedded in water-filled chambers such as laboratory models of collapsible tubes. Other inspiring studies, that include fluid flow, for future work on this thesis are : [54], [55], [56].

Another aspect of future work for the optimization of the conclusions of Deformation

Theory, that was utilized in this thesis as a material model simulating the behavior of collapsible tubes, could be the examination of more material exponents. As noted in Chapter 7 the material exponent with value equal with 2 is a limit case of exponent between uniform collapse and propagation. Thus, for an extension of this study, material exponents with value between 2 and 2.4 could be scrutinized.

Finally an extension of this study could be conducted by utilizing hyperelastic materials, instead Deformation Theory material model, while investigating the existing hyperelastic forms and their parameters available in literature and in ABAQUS documentation.

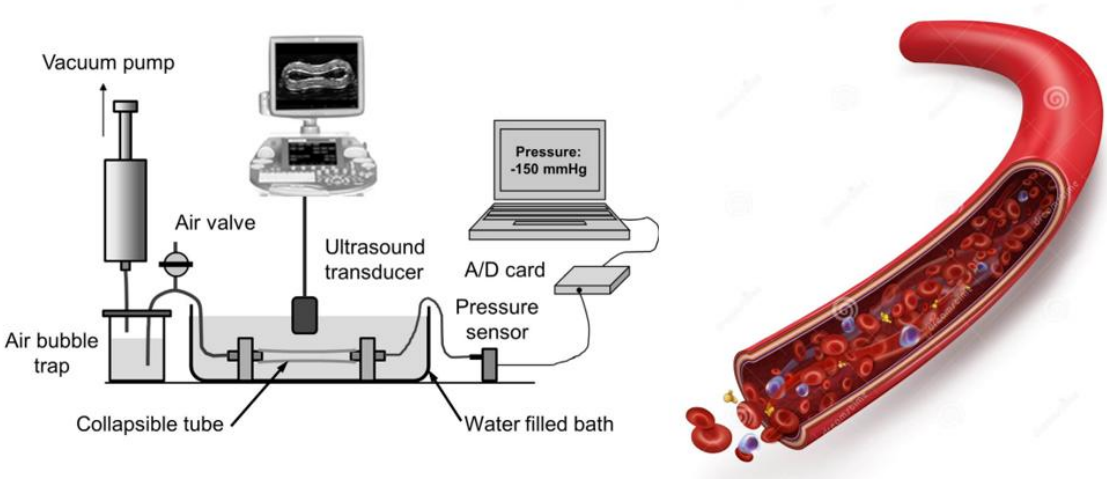

Figure 8.1: Experimental setup [1] on the left side and vein's blood flow on the right side.

Bibliography

[1] Pavel Kozlovsky, Uri Zaretsky, Ariel J. Jaffa, and David Elad. General tube law for collapsible thin and thick-wall tubes. *Journal of Biomechanics*, 47(10):2378–2384, July 2014.

[2] PM Vanhoutte, S Corcaud, C De Montrion, and Paul M Vanhoutte. Venous disease: from pathophysiology to quality of life. *Angiology*, 48(7):559–567, 1997.

[3] Michael J Joyner and Darren P Casey. Regulation of increased blood flow (hyperemia) to muscles during exercise: a hierarchy of competing physiological needs. *Physiological reviews*, 2015.

[4] Horner RL, Innes JA, Morrell MJ, Shea SA, and Guz A. The effect of sleep on reflex genioglossus muscle activation by stimuli of negative airway pressure in humans. *The Journal of Physiology*, 476(1):141–51, April 1994.

[5] Thach BT, Abu-Osba Y, and Mathew OP. Influence of upper airway pressure changes on genioglossus muscle respiratory activity. *J Appl Physiol Respir Environ Exerc Physiol.*, 52(2):438– 444, February 1982.

[6] Malhotra A, Pillar G, Fogel R, Beauregard J, Edwards J, and White DP. Upper-airway collapsibility: measurements and sleep effects. *Chest.*, 120(1):156–161, July 2001.

[7] Isono S. Obesity and obstructive sleep apnoea: Mechanisms for increased collapsibility of the passive pharyngeal airway. *Respirology*, 17(1):32–42, January 2012.

[8] Peter R Eastwood, Irene Szollosi, Peter R Platt, and David R Hillman. Comparison of upper airway collapse during general anesthesia and sleep. *The Lancet*, 359(9313):1207–1209, April 06 2002.

[9] Chun Xu, Michael J. Brennick, Lawrence Dougherty, and David M. Wootton. Modeling upper airway collapse by a finite element model with regional tissue properties. *Medical Engineering & Physics*, 31(10):1343–1348, December 2009.

[10] A. Ibbeken, C. Hagen, F. Zell, A. Steffen, U. Grzyska, A. Frydrychowicz, and T. Buzug. Determination of the critical closing pressure for a 3d printed collapsible model of an idealized upper airway geometry. *Transactions on Additive Manufacturing Meets Medicine*, 2(1), September 09 2020.

[11] K. R. Lutchen and H. Gillis. Relationship between heterogeneous changes in airway morphometry and lung resistance and elastance. *Journal of Applied Physiology*, 83(4):1192–1201, October 01 1997.

[12] Ann Della Maggiore. Tracheal and airway collapse in dogs. *Veterinary Clinics of North America: Small Animal Practice*, 44(1):117–127, January 2014.

[13] John R. Fitz-Clarke. Mechanics of airway and alveolar collapse in human breath-hold diving. *Respiratory Physiology and Neurobiology*, 159(2):202–210, November 15 2007.

[14] Joseph E. Flaherty, Joseph B. Keller, and S. I. Rubinow. Post buckling behavior of elastic tubes and rings with opposite sides in contact. *SIAM Journal on Applied Mathematics*, 23(4):446–455, 1972.

[15] Ole Fabian. Collapse of cylindrical, elastic tubes under combined bending, pressure and axial loads. *International Journal of Solids and Structures*, 13(12):1257–1270, 1977.

[16] S. Bassez, P. Flaud, and M. Chauveau. Modeling of the deformation of flexible tubes using a single law: Application to veins of the lower limb in man. *Journal of Biomechanical Engineering*, 123(1):58, 2001.

[17] Y. Zhu, X.Y. Luo, and R.W. Ogden. Nonlinear axisymmetric deformations of an elastic tube under external pressure. *European Journal of Mechanics - A/Solids*, 29(2):216–229, March–April 2010.

[18] Y. Zhu, X.Y. Luo, H.M. Wang, R.W. Ogden, and C. Berry. Three-dimensional nonlinear buckling of thick-walled elastic tubes under pressure. *International Journal of Non-Linear Mechanics*, 48:1–14, 2013.

[19] J. Duomarco, R. Rimini, C. E. Giambruno, R. Seoane, and M. Haendel. Systemic venous collapse in man. *The American Journal of Cardiology*, 11(3):357–361, 1963.

[20] W.J. Joo, M. Fukui, K. Kooguchi, M. Sakaguchi, and T. Shinzato. Transcutaneous pressure at which the internal jugular vein is collapsed on ultrasonic imaging predicts easiness of the venous puncture. *Journal of Anesthesia*, 25(2):308–311, April 2011.

[21] C.D. Bertram and T.J. Pedley. A mathematical model of unsteady collapsible tube behaviour. *Journal of Biomechanics*, 15(1):39–50, 1982.

[22] T. Pedley and X. Luo. Modelling flow and oscillations in collapsible tubes. *Theoretical and Computational Fluid Dynamics*, 10:277–294, January 1998.

[23] B.S. Brook and T.J. Pedley. A model for time-dependent flow in (giraffe jugular) veins: uniform tube properties. *Journal of Biomechanics*, 35(1):95–107, 2002.

[24] Y. C. Fung. *Biomechanics: Circulation*. Springer, New York, 2nd edition, April 17 1997.

[25] J.M. Downing and D.N. Ku. Effects of frictional losses and pulsatile flow on the collapse of stenotic arteries. *Journal of Biomechanical Engineering*, 119(3):317–324, August 1997.

[26] Dalin Tang, Chun Yang, Shigeo Kobayashi, and David N. Ku. Steady flow and wall compression in stenotic arteries: a three-dimensional thick-wall model with fluid-wall interactions. *Journal of Biomechanical Engineering*, 123(6):548–557, December 2001.

[27] E. Kresch and A. Noordergraaf. Cross-sectional shape of collapsible tubes. *Biophysical Journal*, 12(3):274–294, 1972.

[28] Michel Bitbol, Philippe Dantan, P. Perrot, and Christian Oddou. Collapsible tube model for the dynamics of closure of the mitral valve. *Journal of Fluid Mechanics*, 114:187 – 211, 1982.

[29] Peskin Rosar. *A three-dimensional computer model for fluid flow through a collapsible tube*. New York University, 1994.

[30] S.A. Karamanos. *Structural Mechanics and Design of Metal Pipes: A Systematic Approach for Onshore and Offshore Pipelines*. Elsevier, 2023.

[31] Mesloh R.E., Sorenson J. E., and Atterbury T. J. Buckling–and offshore pipelines. 49(7):40–43, July 01 1973.

[32] Martin J. H. Palmer A. C. Buckle propagation in submarine pipelines. *Nature*, 254(5495):46–48, 1975.

[33] Lee L.-H. Kyriakides S. Buckle propagation in confined steel tubes. *International Journal of Mechanical Sciences*, 47(4-5):603–620, 2005.

[34] Calladine C. R. Kamalarasa S. Buckle propagation in submarine pipelines. *International Journal of Mechanical Sciences*, 30(3-4):217–228, 1988.

[35] Haofeng Liang, Jiahui Zhou, Jixin Lin, Fusong Jin, Fei Xia andJianghong Xue, and Jiachu Xu. Buckle propagation in steel pipes of ultra-high strength: Experiments, theories and numerical simulations. *Acta Mechanica Solida Sinica*, 33(4):546–563, 2020.

[36] C. R. Kennedy and J. T. Venard. Collapse of tubes by external pressure. Technical report, United States, 1962.

[37] Y. Bai, R. T. Igland, and T. Moan. Tube collapse under combined external pressure, tension and bending. *Marine Structures*, 10(5):389–410, 1997.

[38] M. K. Yeh and S. Kyriakides. Collapse of deepwater pipelines. In *Proceedings of Offshore Technology Conference*, Houston, TX, USA, 1986.

[39] Kyriakides S. Yeh M. K. On the collapse of inelastic thick-walled tubes under external pressure. *Journal of Energy Resources Technology*, 108(1):35–47, March 1986.

[40] S. Kyriakides and L.H. Lee. *Mechanics of Offshore Pipelines: Vol. 2 Buckle Propagation and Arrest*, volume 2. Gulf Professional Publishing, 2020.

[41] B. Budiansky. Theory of buckling and post-buckling behavior of elastic structures. *Advances in Applied Mechanics*, 14:1–65, 1974.

[42] E. Chater and J. W. Hutchinson. On the propagation of bulges and buckles. *Journal of Applied Mechanics*, 51(2):269–277, 1984.

[43] J. Chakrabarty. *Theory of Plasticity*. Butterworth-Heinemann, 2005.

[44] H. Hencky. Zur theorie plastischer deformationen und der hierdurch im material hervorgerufenen nachspannungen. *ZAMM - Zeitschrift Für Angewandte Mathematik Und Mechanik*, 4(4):323–334, 1924.

[45] ABAQUS Version 6.6 Documentation. Hyperelastic behavior of rubberlike materials (17.5.1). Analysis User's Manual.

[46] L. R. G. Treloar. *The Physics of Rubber Elasticity*. Oxford University Press, 3rd edition, 2005.

[47] Babcock C. D. Kyriakides S. Large deflection collapse analysis of an inelastic inextensional ring under external pressure. *International Journal of Solids and Structures*, 17(10):981–993, 11 1981.

[48] C.D. Bertram A. Marzo, X.Y. Luo. Three-dimensional collapse and steady flow in thick-walled flexible tubes. *Journal of Fluids and Structures*, 20(6):817–835, 2005.

[49] C.D. Bertram. The effects of wall thickness, axial strain and end proximity on the pressure-area relation of collapsible tubes. *Journal of Biomechanics*, 20(9):863–876, 1987.

[50] R.J. Castles C.D. Bertram. Flow limitation in uniform thick-walled collapsible tubes. *Journal of Fluids and Structures*, 13(3):399–418, 1999.

[51] Peskin Charles Rosar M. Fluid flow in collapsible elastic tubes: A three-dimensional numerical model. *New York Journal of Mathematics New York J. Math*, 7:281–302, 01 2001.

[52] Moreno A.H. Katz A.I., Chen Y. Flow through a collapsible tube. experimental analysis and mathematical model. *Biophysical Journal*, 9(10):1261–1279, 1969.

[53] Elad D., Sahar M., Avidor J.M., and Einav S. Steady flow through collapsible tubes: measurements of flow and geometry. *Journal of Biomechanical Engineering*, 114(1):84–91, 1992.

[54] Jensen Oliver Grotberg James. Biofluid mechanics in flexible tubes. annu rev fluid mech. *Annu. Rev. Fluid Mech*, 36:121–47, 01 2004.

[55] A. H. Shapiro. Steady flow in collapsible tubes. *Journal of Biomechanical Engineering*, 99(3):126–147, 1977.

[56] Timothy J Pedley and Xiaoyu Luo. Modelling flow and oscillations in collapsible tubes. *Theoretical and Computational Fluid Dynamics*, 10:277–294, 1998.

APPENDIX

Appendix

Matlab codes

The developed matlab codes that were created for this Diploma Thesis are presented below. They consist of 3 different .m files and a function that should be saved separately.

```
%% 1: Plot the stress-strain curve for different material exponents alongside the linear elastic stress-strain cuve
clear all;close all;clc
%-----------------------------------------------------------
% Specify the folder path
folderPath = 'C:\Users\Ioanna\Desktop\Material_Exponents';
%-----------------------------------------------------------
% Get a list of all text files in the folder
fileList = dir(fullfile(folderPath, '*.txt'));
numFiles = numel(fileList);
% Iterate over each file
for fileIndex = 1:numFiles
    % Get the file name
    fileName = fileList(fileIndex).name;
    % Create the full file path
    filePath = fullfile(folderPath, fileName);
    % Read the data from the text file
    data = dlmread(filePath);
    % Extract the two columns
    strain = data(:, 1);
```

```
    stress = data(:, 2)*1e-3;
    % Plot the figures
    plot(strain,stress)
    xlabel('Strain, [%]')
    ylabel('Stress, [kPa]')
    hold on
end
legend('2.4','2.8','2.6','2.9','linear elastic')
xlim([0,10])
%% 2: Plot the dimentionless pressure-volume curves for the 2D case for the 6 different ovalities
clear all;close all;clc
%% First Step: Get all the data
% Specify the paths to the main folders
mainFolderPaths = {'C:\Users\Ioanna\Desktop\2D_plots\Dt_10', 'C:\Users\Ioanna\Desktop\2D_plots\Dt_20', 'C:\Users\Ioanna\Desktop\2D_plots\Dt_40'};
cellArray = cell(3, 6, 3); % 3 folders, 6 subfolders, 3 rpt files
% Loop through the main folders
for mainFolderIndex = 1:numel(mainFolderPaths)
    mainFolderPath = mainFolderPaths{mainFolderIndex};
    % Get the list of subfolders within the main folder
    subFolderPaths = dir(mainFolderPath);
    subFolderPaths = subFolderPaths([subFolderPaths.isdir]);
    subFolderPaths = subFolderPaths(~ismember({subFolderPaths.name}, {'.', '..'}));
    % Loop through the subfolders
    for subFolderIndex = 1:numel(subFolderPaths)
        subFolderPath = fullfile(mainFolderPath, subFolderPaths(subFolderIndex).name);
        % Get the list of rpt files within the subfolder
```

```
46          rptFiles = dir(fullfile(subFolderPath, '*.rpt'));
47          % Loop through the rpt files
48          % Coord1
49          rptFilePath = fullfile(subFolderPath, rptFiles(1).
               name);
50          cellArray{mainFolderIndex, subFolderIndex, 1} =
               importdata(rptFilePath);
51          % Coord2
52          rptFilePath = fullfile(subFolderPath, rptFiles(2).
               name);
53          cellArray{mainFolderIndex, subFolderIndex, 2} =
               importdata(rptFilePath);
54          % Pressure
55          rptFilePath = fullfile(subFolderPath, rptFiles(3).
               name);
56          cellArray{mainFolderIndex, subFolderIndex, 3} =
               importdata(rptFilePath);
57      end
58  end
59  %% Second Step: Plots
60  E=3.4;
61  poisson=0.4;
62  % Ovality 02
63  %--- Dt_10
64  t(1) = 50;
65  Dnom(1) = t(1)*10;
66  Pcr(1) = (2*E/(1-poisson^2))*(t(1)/Dnom(1))^3;
67  INRmin2(1) = 224.5;
68  INRmax2(1) = 225.5;
69  ao2(1) = (1/4)*pi*(INRmax2(1)*INRmin2(1));
70  numel_hoop(1) = 100;
71  %--- Dt_20
```

```
t(2) = 26.1904762;
Dnom(2) = t(2)*20;
Pcr(2) = (2*E/(1-poisson^2))*(t(2)/Dnom(2))^3;
INRmin2(2) = 248.29;
INRmax2(2) = 249.33;
numel_hoop(2) = 100;
ao2(2) = (1/4)*pi*(INRmax2(2)*INRmin2(2));
%--- Dt_40
t(3) = 13.4146341;
Dnom(3) = t(3)*40;
Pcr(3) = (2*E/(1-poisson^2))*(t(3)/Dnom(3))^3;
INRmin2(3) = 261.05;
INRmax2(3) = 262.12;
ao2(3) = (1/4)*pi*(INRmax2(3)*INRmin2(3));
numel_hoop(3) = 130;
figure;
for j = 1:3
%import data from rpt file
x2 = cellArray{j,1,1};
y2 = cellArray{j,1,2};
p2 = cellArray{j,1,3};
%initialization of arrays
ainc2=zeros(size(x2,1),1);
da2=zeros(size(x2,1),1);
daao2=zeros(size(x2,1),1);
% calculation of the area enclosed by the quadrant at every
    increment
for i=1:size(x2,1)        % moving through increments
    n=1;
        slice=0;
        for k=n:numel_hoop(j)
```

```
                slice=slice+abs((x2(i,k)-x2(i,k+1)))*(y2(i,k+1)+
                    y2(i,k))/2;
            end
            n=k+2;
            ainc2(i,1)=slice;
            da2(i,1)=(ao2(j)-ainc2(i,1))*(1e-06); % da in [m]
            daao2(i,1)=(1/ao2(j))*(abs(ao2(j)-ainc2(i,1)));
end
plot(daao2,p2/Pcr(j))
hold on
end
xlabel('da/ao')
ylabel('P/Pcr')
legend('Dt=10','Dt=20','Dt=40','Location', 'southeast', '
    EdgeColor', 'w', 'FontSize', 11)
xlim([0 0.8])
ylim([0 2])
hold off
% Save the plot as PDF
fileName = sprintf('ovality_02.pdf');
saveas(gcf, fileName, 'pdf');
% Close the figure
close(gcf);
%%%%%%%%%%%%%%%%%%%%%%%%%%%%%%%%%%%%%%%%%%%%%%%%%%%%%%%%%%%%%%%%%%%
% Ovality 05
%--- Dt_10
t(1) = 50;
Dnom(1) = t(1)*10;
Pcr(1) = (2*E/(1-poisson^2))*(t(1)/Dnom(1))^3;
INRmin2(1) = 223.75;
INRmax2(1) = 226.25;
ao2(1) = (1/4)*pi*(INRmax2(1)*INRmin2(1));
```

```
numel_hoop(1) = 100;
%--- Dt_20
t(2) = 26.1904762;
Dnom(2) = t(2)*20;
Pcr(2) = (2*E/(1-poisson^2))*(t(2)/Dnom(2))^3;
INRmin2(2) = 247.5;
INRmax2(2) = 250.12;
numel_hoop(2) = 100;
ao2(2) = (1/4)*pi*(INRmax2(2)*INRmin2(2));
%--- Dt_40
t(3) = 13.4146341;
Dnom(3) = t(3)*40;
Pcr(3) = (2*E/(1-poisson^2))*(t(3)/Dnom(3))^3;
INRmin2(3) = 260.24;
INRmax2(3) = 262.93;
ao2(3) = (1/4)*pi*(INRmax2(3)*INRmin2(3));
numel_hoop(3) = 130;
figure;
for j = 1:3
%import data from rpt file
x2 = cellArray{j,2,1};
y2 = cellArray{j,2,2};
p2 = cellArray{j,2,3};
%initialization of arrays
ainc2=zeros(size(x2,1),1);
da2=zeros(size(x2,1),1);
daao2=zeros(size(x2,1),1);
% calculation of the area enclosed by the quadrant at every
    increment
for i=1:size(x2,1)        % moving through increments
    n=1;
        slice=0;
```

```
            for k=n:numel_hoop(j)
                slice=slice+abs((x2(i,k)-x2(i,k+1)))*(y2(i,k+1)+
                    y2(i,k))/2;
            end
            n=k+2;
            ainc2(i,1)=slice;
            da2(i,1)=(ao2(j)-ainc2(i,1))*(1e-06); % da in [m]
            daao2(i,1)=(1/ao2(j))*(abs(ao2(j)-ainc2(i,1)));
end
plot(daao2,p2/Pcr(j))
hold on
end
xlabel('da/ao')
ylabel('P/Pcr')
legend('Dt=10','Dt=20','Dt=40','Location', 'southeast', '
    EdgeColor', 'w', 'FontSize', 11)
xlim([0 0.8])
ylim([0 2])
hold off
% Save the plot as PDF
fileName = sprintf('ovality_05.pdf');
saveas(gcf, fileName, 'pdf');
% Close the figure
close(gcf);
%%%%%%%%%%%%%%%%%%%%%%%%%%%%%%%%%%%%%%%%%%%%%%%%%%%%%%%%%%%%
% Ovality 07
%--- Dt_10
t(1) = 50;
Dnom(1) = t(1)*10;
Pcr(1) = (2*E/(1-poisson^2))*(t(1)/Dnom(1))^3;
INRmin2(1) = 223.25;
INRmax2(1) = 226.75;
```

```
ao2(1) = (1/4)*pi*(INRmax2(1)*INRmin2(1));
numel_hoop(1) = 100;
%--- Dt_20
t(2) = 26.1904762;
Dnom(2) = t(2)*20;
Pcr(2) = (2*E/(1-poisson^2))*(t(2)/Dnom(2))^3;
INRmin2(2) = 246.98;
INRmax2(2) = 250.64;
numel_hoop(2) = 100;
ao2(2) = (1/4)*pi*(INRmax2(2)*INRmin2(2));
%--- Dt_40
t(3) = 13.4146341;
Dnom(3) = t(3)*40;
Pcr(3) = (2*E/(1-poisson^2))*(t(3)/Dnom(3))^3;
INRmin2(3) = 259.71;
INRmax2(3) = 263.46;
ao2(3) = (1/4)*pi*(INRmax2(3)*INRmin2(3));
numel_hoop(3) = 130;
figure;
for j = 1:3
%import data from rpt file
x2 = cellArray{j,3,1};
y2 = cellArray{j,3,2};
p2 = cellArray{j,3,3};
%initialization of arrays
ainc2=zeros(size(x2,1),1);
da2=zeros(size(x2,1),1);
daao2=zeros(size(x2,1),1);
% calculation of the area enclosed by the quadrant at every
    increment
for i=1:size(x2,1)        % moving through increments
    n=1;
```

```
            slice=0;
            for k=n:numel_hoop(j)
                slice=slice+abs((x2(i,k)-x2(i,k+1)))*(y2(i,k+1)+y2(i,k))/2;
            end
            n=k+2;
            ainc2(i,1)=slice;
            da2(i,1)=(ao2(j)-ainc2(i,1))*(1e-06); % da in [m]

            daao2(i,1)=(1/ao2(j))*(abs(ao2(j)-ainc2(i,1)));
end
plot(daao2,p2/Pcr(j))
hold on
end
xlabel('da/ao')
ylabel('P/Pcr')
legend('Dt=10','Dt=20','Dt=40','Location', 'southeast', 'EdgeColor', 'w', 'FontSize', 11)
xlim([0 0.8])
ylim([0 2])
hold off
% Save the plot as PDF
fileName = sprintf('ovality_07.pdf');
saveas(gcf, fileName, 'pdf');
% Close the figure
close(gcf);
%%%%%%%%%%%%%%%%%%%%%%%%%%%%%%%%%%%%%%%%%%%%%%%%%%
% Ovality 1
%--- Dt_10
t(1) = 50;
Dnom(1) = t(1)*10;
Pcr(1) = (2*E/(1-poisson^2))*(t(1)/Dnom(1))^3;
```

```
INRmin2(1) = 222.5;
INRmax2(1) = 227.5;
ao2(1) = (1/4)*pi*(INRmax2(1)*INRmin2(1));
numel_hoop(1) = 100;
%--- Dt_20
t(2) = 26.1904762;
Dnom(2) = t(2)*20;
Pcr(2) = (2*E/(1-poisson^2))*(t(2)/Dnom(2))^3;
INRmin2(2) = 246.19;
INRmax2(2) = 251.43;
numel_hoop(2) = 100;
ao2(2) = (1/4)*pi*(INRmax2(2)*INRmin2(2));
%--- Dt_40
t(3) = 13.4146341;
Dnom(3) = t(3)*40;
Pcr(3) = (2*E/(1-poisson^2))*(t(3)/Dnom(3))^3;
INRmin2(3) = 258.9;
INRmax2(3) = 264.27;
ao2(3) = (1/4)*pi*(INRmax2(3)*INRmin2(3));
numel_hoop(3) = 130;
figure;
for j = 1:3
%import data from rpt file
x2 = cellArray{j,4,1};
y2 = cellArray{j,4,2};
p2 = cellArray{j,4,3};
%initialization of arrays
ainc2=zeros(size(x2,1),1);
da2=zeros(size(x2,1),1);
daao2=zeros(size(x2,1),1);
% calculation of the area enclosed by the quadrant at every
    increment
```

```
for i=1:size(x2,1)          % moving through increments
    n=1;
        slice=0;
        for k=n:numel_hoop(j)
            slice=slice+abs((x2(i,k)-x2(i,k+1)))*(y2(i,k+1)+
                y2(i,k))/2;
        end
        n=k+2;

        ainc2(i,1)=slice;

        da2(i,1)=(ao2(j)-ainc2(i,1))*(1e-06); % da in [m]

        daao2(i,1)=(1/ao2(j))*(abs(ao2(j)-ainc2(i,1)));
end
plot(daao2,p2/Pcr(j))
hold on
end
xlabel('da/ao')
ylabel('P/Pcr')
legend('Dt=10','Dt=20','Dt=40','Location', 'southeast', '
    EdgeColor', 'w', 'FontSize', 11)
xlim([0 0.8])
ylim([0 2])
hold off
% Save the plot as PDF
fileName = sprintf('ovality_1.pdf');
saveas(gcf, fileName, 'pdf');
% Close the figure
close(gcf);
%%%%%%%%%%%%%%%%%%%%%%%%%%%%%%%%%%%%%%%%%%%%
% Ovality 10
```

```
%--- Dt_10
t(1) = 50;
Dnom(1) = t(1)*10;
Pcr(1) = (2*E/(1-poisson^2))*(t(1)/Dnom(1))^3;
INRmin2(1) = 200;
INRmax2(1) = 250;
ao2(1) = (1/4)*pi*(INRmax2(1)*INRmin2(1));
numel_hoop(1) = 100;
%--- Dt_20
t(2) = 26.1904762;
Dnom(2) = t(2)*20;
Pcr(2) = (2*E/(1-poisson^2))*(t(2)/Dnom(2))^3;
INRmin2(2) = 222.62;
INRmax2(2) = 275;
numel_hoop(2) = 100;
ao2(2) = (1/4)*pi*(INRmax2(2)*INRmin2(2));
%--- Dt_40
t(3) = 13.4146341;
Dnom(3) = t(3)*40;
Pcr(3) = (2*E/(1-poisson^2))*(t(3)/Dnom(3))^3;
INRmin2(3) = 234.76;
INRmax2(3) = 288.41;
ao2(3) = (1/4)*pi*(INRmax2(3)*INRmin2(3));
numel_hoop(3) = 130;
figure;
for j = 1:3
%import data from rpt file
x2 = cellArray{j,5,1};
y2 = cellArray{j,5,2};
p2 = cellArray{j,5,3};
%initialization of arrays
ainc2=zeros(size(x2,1),1);
```

```
da2=zeros(size(x2,1),1);
daao2=zeros(size(x2,1),1);
% calculation of the area enclosed by the quadrant at every increment
for i=1:size(x2,1)        % moving through increments
    n=1;
        slice=0;
        for k=n:numel_hoop(j)
            slice=slice+abs((x2(i,k)-x2(i,k+1)))*(y2(i,k+1)+y2(i,k))/2;
        end
        n=k+2;

        ainc2(i,1)=slice;

        da2(i,1)=(ao2(j)-ainc2(i,1))*(1e-06); % da in [m]

        daao2(i,1)=(1/ao2(j))*(abs(ao2(j)-ainc2(i,1)));

end
plot(daao2,p2/Pcr(j))
hold on
end
xlabel('da/ao')
ylabel('P/Pcr')
legend('Dt=10','Dt=20','Dt=40','Location', 'southeast', 'EdgeColor', 'w', 'FontSize', 11)
xlim([0 0.8])
ylim([0 2])
hold off
% Save the plot as PDF
fileName = sprintf('ovality_10.pdf');
```

```
saveas(gcf, fileName, 'pdf');
% Close the figure
close(gcf);
%%%%%%%%%%%%%%%%%%%%%%%%%%%%%%%%%%%%%%%%
% Ovality 5
%--- Dt_10
t(1) = 50;
Dnom(1) = t(1)*10;
Pcr(1) = (2*E/(1-poisson^2))*(t(1)/Dnom(1))^3;
INRmin2(1) = 212.5;
INRmax2(1) = 237.5;
ao2(1) = (1/4)*pi*(INRmax2(1)*INRmin2(1));
numel_hoop(1) = 100;
%--- Dt_20
t(2) = 26.1904762;
Dnom(2) = t(2)*20;
Pcr(2) = (2*E/(1-poisson^2))*(t(2)/Dnom(2))^3;
INRmin2(2) = 235.71;
INRmax2(2) = 261.90;
numel_hoop(2) = 100;
ao2(2) = (1/4)*pi*(INRmax2(2)*INRmin2(2));
%--- Dt_40
t(3) = 13.4146341;
Dnom(3) = t(3)*40;
Pcr(3) = (2*E/(1-poisson^2))*(t(3)/Dnom(3))^3;
INRmin2(3) = 248.17;
INRmax2(3) = 275;
ao2(3) = (1/4)*pi*(INRmax2(3)*INRmin2(3));
numel_hoop(3) = 130;
figure;
for j = 1:3
%import data from rpt file
```

```
x2 = cellArray{j,6,1};
y2 = cellArray{j,6,2};
p2 = cellArray{j,6,3};
%initialization of arrays
ainc2=zeros(size(x2,1),1);
da2=zeros(size(x2,1),1);
daao2=zeros(size(x2,1),1);
% calculation of the area enclosed by the quadrant at every
    increment
for i=1:size(x2,1)        % moving through increments
    n=1;
        slice=0;
        for k=n:numel_hoop(j)
            slice=slice+abs((x2(i,k)-x2(i,k+1)))*(y2(i,k+1)+
                y2(i,k))/2;
        end
        n=k+2;
        ainc2(i,1)=slice;
        da2(i,1)=(ao2(j)-ainc2(i,1))*(1e-06); % da in [m]
        daao2(i,1)=(1/ao2(j))*(abs(ao2(j)-ainc2(i,1)));
end
plot(daao2,p2/Pcr(j))
hold on
end
xlabel('da/ao')
ylabel('P/Pcr')
legend('Dt=10','Dt=20','Dt=40','Location', 'southeast', '
    EdgeColor', 'w', 'FontSize', 11)
xlim([0 0.8])
ylim([0 2])
hold off
% Save the plot as PDF
```

```
fileName = sprintf('ovality_5.pdf');
saveas(gcf, fileName, 'pdf');
% Close the figure
close(gcf);
%% 3: Plot the dimensionless respone for the different
    material exponents used
clear all;close all;clc
%
    ------------------------------------------------------------------

% Specify the directory path
directoryPath = 'C:\Users\ds3922\Desktop\Ioanna\
    slice_dtr12_new';
%
    ------------------------------------------------------------------

% Read the directory contents
contents = dir(directoryPath);
% Initialize an empty cell array to store folder names
folderNames = {};
% Iterate through each entry in the directory
for i = 1:numel(contents)
    entry = contents(i);
    % Check if the entry is a directory and not "." or ".."
    if entry.isdir && ~strcmp(entry.name, '.') && ~strcmp(
        entry.name, '..')
        % Add the folder name to the cell array
        folderNames{end+1} = entry.name;
    end
end
% Display the folder names
disp('Folder names in the directory:');
```

```
disp(folderNames);
% Get the current directory
currentDirectory = pwd;
% Loop through each folder name
for i = 1:numel(folderNames)
    folderName = folderNames{i};
    % Construct the full path of the folder
    folderPath = fullfile(currentDirectory, folderName);
    % Check if the folder exists
    if exist(folderPath, 'dir')
        % Display the folder name
        disp(['Processing folder: ' folderName]);
        % Get the list of .rpt files in the folder
        rptFiles = dir(fullfile(folderPath, '*.rpt'));
       % Read Coord 1
       folderPath = fullfile(currentDirectory, folderName,
          rptFiles(1).name);
       x = importdata(folderPath);
       % Read Coord 2
       folderPath = fullfile(currentDirectory, folderName,
          rptFiles(2).name);
       y = importdata(folderPath);
       % Read Pressure
       folderPath = fullfile(currentDirectory, folderName,
          rptFiles(3).name);
       p = importdata(folderPath);
       % Calculate parameters for the plot
       [p_out,daao,M] = Postprocessing(x,y,p);
       plot(daao, p_out)
       yline(M, '--', 'Color', 'k');
       hold on
    else
```

```
            disp(['Folder does not exist: ' folderName]);
        end
end
legend('2_4','Maxwell Line','2_6','Maxwell Line','2_8','Maxwell Line','2_9','Maxwell Line','3','Maxwell Line','3_1','Maxwell Line','3_5''Maxwell Line')
xlim([0 0.78])
%% 3b: Function defined for the 3rd .m file
function [p_out,daao,M] = Postprocessing(x,y,p)
%%%%%%%%%%%%%%%%%%%%%%%%
% ring input
INRmin=232.18;
INRmax=233.20;
t=42.31;
numel_hoop=25;
%undeformed area
ao=(1/4)*pi*(INRmax*INRmin);
%initialization of arrays
ainc=zeros(size(x,1),1);
da=zeros(size(x,1),1);
daao=zeros(size(x,1),1);
% calculation of the area enclosed by the quadrant at every increment
for i=1:size(x,1)        % moving through increments
    n=1;
        slice=0;
        for k=n:numel_hoop
            slice=slice+abs((x(i,k)-x(i,k+1)))*(y(i,k+1)+y(i,k))/2;
        end
        n=k+2;
        ainc(i,1)=slice;
```

```
            da(i,1)=(ao-ainc(i,1));
            daao(i,1)=(1/ao)*(abs(ao-ainc(i,1)));
end
%% MAXWELL LINE
M = p(end);  % set initial value of M to the last value of pressure
da_interp = linspace(min(da), max(da), 1e5);  % Adjust the number of points as needed
p_interp = interp1(da, p, da_interp);
for dcr = numel(p_interp):-1:1
    Ptemp = p_interp(1:dcr);
    datem = da_interp(1:dcr);
    A = trapz(datem, Ptemp);
    Mnew = A / da_interp(dcr);
    if abs(Mnew - M) < 1e-12
        % convergence criteria
          break
    end
    M = Mnew;
end
Dnom=t*12
E=3.4
poisson=0.4
Pcr=(2*E/(1-poisson^2))*(t/Dnom)^3;
%plot(daao, P./Pcr, '--', 'Color', 'k')
% Conversion of pressure from MPa to kPa
 p_out = p*1e3;
 M=M*1e3;
end
```